Applications of Carbon Nanotubes in Drug Delivery

by

© Karina de Almeida Barcelos

A thesis submitted to the School of Graduate Studies

in partial fulfillment of the requirements for the degree of

Master of Science in Pharmacy

School of Pharmacy

Memorial University of Newfoundland

July 2022

St. John's, Newfoundland and Labrador, Canada

Abstract

The latest carbon nanotubes (CNTs) applications and functionalities for disease treatment and diagnosis have been presented to further comprehend their role and significance in medicine. Recent CNTs-based approaches in therapeutical designs, biomedical engineering, regenerative medicine, biosensing and bioimaging have demonstrated various attractive possibilities for future people's health and quality of life enhancements, such as for cancer and infection therapies. Particularly for drug and gene delivery, these nanoparticles (NPs) have been studied extensively for transporting and translocating molecules into specific sites to attenuate undesired side effects and improve bioavailability and release efficiency of drugs, as well as physicochemical and biological properties of CNTs.

We proposed a bioinspired, non-covalent CNTs functionalization strategy to augment their bioavailability and alleviate their biotoxicity. For functionalization, select amphiphilic peptides from a cytoskeletal biopolymer, microtubule (MT), were used. The peptides are involved in the MT polymerization by maintaining the essential lateral interactions among the MT's α- and β-tubulin subunits. They also participate in forming the MT-binding sites for hosting several MT-targeting antimitotics. Utilizing *in silico* methods, this study showed the peptides influenced CNT's diffusivity and aqueous solubility. The hydrodynamic shield formed by the peptides from β-tubulin was more widespread on the CNT than the α-tubulin peptides'; however, the latter created a broader hydrophobic CNT coating than those from the β-tubulin. In particular, the peptides consisting of the H1–B2, H10, H1–B2, and the M-loop, demonstrated structural features that serve to augment CNTs' water solubility and dispersibility. The performance of the peptide-functionalized CNTs as drug carriers was

examined by studying seventeen antimitotics. The CNT–peptides structural composition was identified as a suitable carrier for phomopsin A, laulimalide, epothilone A, epothilone D, discodermolide, eribulin, and docetaxel. The peptides played dual roles displaying affinities to the antimitotics and the CNT; in particular, the peptides from the H1–B2 and H2–B3 loops of β-tubulin exhibited exceptional binding properties. Specific mutations on the wildtype peptides, including those from the α-tubulin M-loop and H2–B3, or the β-tubulin H1–B2, are proposed to refine their hydrophobicity, eliminate unfavorable inter-peptides electrostatic interactions or the spatial hindrance at certain regions, to enhance their conformational steadiness and exposure to the tube surface. A combination of the select amphiphilic peptides from both tubulin subunits is suggested to improve CNTs bioavailability and efficiency for carrying insoluble hydrophobic cargos.

Acknowledgement

I would like to express my deepest appreciation to my supervisor, Dr. Laleh Alisaraie, for providing me with the opportunity of joining her research group. Her insightful suggestions and skillful guidance encouraged me to sharpen my thinking and brought the project to a higher level.

I am thankful for all encouragement and support from my lab co-worker and friend Sayi'mone whose kind messages, sympathetic ears, and enthusiasm will always be carried with the most positive memories of her.

Finally, I express my heartiest gratefulness and unconditional love for those who sustained and maintained me strong during my graduate studies. I especially dedicate all my accomplishments to my beloved husband, mother, and sister.

Table of Contents

List of Figures

List of Tables

List of Abbreviations

AA: amino acid

Ab: antibody

AD: Alzheimer's disease

ADP: amylose derivative poly(L-lysine)

BA: betulinic acid

BBB: blood-brain barrier

BC: bacterial cellulose

BMSCs: mesenchymal stromal cells

BRC: bromocriptine

BSA: bovine serum albumin

BV: bacterial vaginosis

CAM: chorioallantoic membrane assay

CDT: chemodynamic therapy

CNT: carbon nanotube

COM: center-of-mass

CPC: carbon nanotube-paper composite

CPT: carboplatin

CS: chitosan

C-SPE: screen-printed electrode

Cys-C: cystatin C

D_A: diffusion coefficient

DCOM: distance between centers of mass

DEX: dexamethasone

DFT: density functional theory

DSB: double strand break

DSSP: dictionary secondary structure of protein

DTIC: dacarbazine

EM: energy minimization

EPI: epirubicin

EPR: enhanced permeability and retention

FA: folic acid

ƒ-CNTs: functionalized carbon nanotubes

FePd: iron-palladium

FET: field-effect transistor

ƒ-MWNT: functionalized multi-walled carbon nanotube

FRET: Förster resonance energy transfer

ƒ-SWNT: single-walled carbon nanotube

GAL: gallic acid

GCE: glassy carbon electrode

GO: graphene oxide

Gox: glucose oxidase

GSH: high glutathione

GT: gene therapy

HA: hyaluronic acid

HAP: hydroxyapatite

HCC: hepatocellular carcinoma

HeLa: human cervical adenocarcinoma

HEP: hericium erinaceus polysaccharide

HiPco: high-pressure carbon monoxide process.

IPN: polymer network

JWCNT: joint-welded carbon nanotube

LINCS: LINear constraint solver

LJ: Lennard-Jones

LTO: lanthanide titanate

MAAc: methacrylic acid

Man: mannose

MD: molecular dynamics

MDA: mammary adenocarcinoma

MIP: molecularly imprinted polymer

MRI: magnetic resonance imaging

MSD: mean squared displacement

MT: microtubule

MTX: methotrexate

MWNT: multi-walled carbon nanotube

NCC: nanocellulose

NIR: near infrared

NPs: nanoparticles

OPLS-AA: optimized potentials for liquid simulations all-atom

PAGP: polyorganophosphazene

PAX or PTX: paclitaxel

PBC: periodic boundary conditions

PCL: polycaprolactone

PDA: polydopamine

PDB: Protein Data Bank

PDT: photodynamic

PEDOT: poly(3,4-ethylenedioxythiophene)

PEG: polyethylene glycol

PEGMA: polyethylene glycol methacrylate

PEI: polyethyleneimine

pfs: protofilaments

PL: peptide lipid

PLA: polylactic acid

PLGA: poly(lactic-*co*-glycolic acid)

PLH: poly(L-histidine)

PME: Particle Mesh Ewald

POPC: phosphatidylcholine

PPy: polypyrrole

PR: position restraint:

PTT: photothermal therapy

PU: polyurethane

PVA: polyvinyl alcohol

rBMSCs: rat bone marrow stromal cells

RES: resveratrol

Rg: radius of gyration

RMSD: root mean square deviation

RMSF: root mean square fluctuation

ROS: reactive oxygen species

RS: regenerated silk

SARS-CoV: severe acute respiratory syndrome coronavirus

SASA: solvent accessible surface area

SD: steepest descent

SL: sucrose laurate

SLD: stathmin-like domain

SPC: simple point charge

SS: secondary structure

SWNT: single-walled carbon nanotube

SWNTs: single-walled carbon nanotubes

TB: tuberculosis

TDN: tetrahedral DNA nanostructure

TEM: transmission electron micrograph

TFT: thin-film transistor

TMC: trimethyl chitosan

TNFα: tumor necrosis factor-alpha

Trp: tryptophan

UHMWPE: ultra-high molecular weight polyethylene

vdW: van der Waals

VLB: vinblastine

Introduction and Overview

Carbon nanotubes (CNTs) have been thoroughly investigated in the past few decades towards designing safe, effective, manageable, tractable, and targeted CNTs-based strategies for medical advances. Up-to-date studies have reflected their propitious aspects of biomedical-related applications. In particular, delivery systems containing these nanoparticles (NPs) as nanoplatforms are customarily formulated with drugs and biomolecules (*e.g.*, peptides, proteins, antibodies, or genetic material) to selectively target disease-containing tissues or cells to restrain side effects of patients and promote drug bioavailability. Functionalization of CNTs is indispensable for their bioapplicability to surpass their low solubility, bioaccumulation, and biodegradability, along with minimizing their inherent aggregation and biotoxicity. In this sense, peptides consisting of amino acids provide befitting hydrophobic or hydrophilic side-chain constituents to moderate interactions between the CNT molecules by hydrophobic and vdW forces, acting as biopolymeric coverage of these NPs. The biomolecule cargos function to modify not only the NPs' surface but also enhance their physical and biological properties.

Chapter 1 shows the latest distinct functionalities and useful properties of functionalized CNTs (*f*-CNTs) for disease treatments and diagnosis in nanomedicine and bioengineering. The novelty of the review is to categorize the recent applications of CNTs to update and inspire researchers with innovative *f*-CNTs-based strategies formulated to be diversly applied, such as in drug or gene delivery systems as nanocarriers; biomedical engineering, tissue engineering, regenerative medicine, biosensing, bioimaging; and diverse contributions

to treatments and diagnosis of mono and combinatorial anticancer therapies, as well as for the immune system, bacterial, and viral infections. The review reveals research gaps regarding the recent *f*-CNTs-based designs, bioavailability, biocompatibility, and efficiency. It has also covered the diverse paraments and techniques currently used to construct, customize, and assess *f*-CNTs-based applications, including external stimuli for drug release or diagnosis, and route administration.

Chapter 2 presents an original contribution to *f*-CNT-based anticancer research. The objective of this *in silico* study is to investigate the coverage effects of ten specific peptides from microtubule (MT) by non-covalently interacting with the pristine, uncharged (16,0) single-walled carbon nanotube (SWNT). The segments are expected to induce superior colloidal characteristics, bioavailability, cellular uptake, and biocompatibility of CNTs. Since these MT segments are involved structurally and functionally in MT polymerization by sustaining the essential lateral and longitudinal interactions of α–β tubulin and accommodating MT-antimitotic agents, the suggested approach can be useful for synergistically performing as MT-targeting ligand nanovehicles, being a step forward to study the nontoxic and biomimetic potential of these peptides on CNTs for designing new drug delivery systems. This chapter elaborates mainly on two relevant components: first, addressing the aqueous affinity and biocompatibility issues of CNTs through the functionalization effect of the interaction of non-covalent tubulin-based peptides onto the CNT; and second, providing insights into a novel anticancer drug delivery suggestion utilizing these NPs as nanotransporters and MT biopeptides, elucidating the peptide–CNT binding properties by molecular dynamics (MD) simulations and the peptide–drug on nanotube binding affinities of seventeen anticancer agents by docking experiments.

Co-authorship Statement

The composition of chapter 1 has been developed by me, Karina de A. Barcelos, who conducted the literature review collection of recent studies, reading, writing, and editing. The contents of chapter 2 have been written in the manuscript format in this thesis and published Open Access titled "Microtubule-inspired functionalization of carbon nanotubes: a biomimetic carrier design" in *Molecular Systems Design & Engineering journal*, **2022**, 7 (4), DOI 10.1039/d1me00190f, by Karina de A. Barcelos & Laleh Alisaraie. This research was predominantly completed by the first author, who performed all computational simulation calculations, all preparation of figures in the manuscript and supplementary information, primary data collection and analyses, and the initial draft of the manuscript. The supervisor (co-author), Dr. Laleh Alisaraie, remarkably contributed and guided all manuscript development *via* the original idea conception, supervision, expertise, critical feedback, and writing (extensive review and editing).

CHAPTER 1

CNTs in Medicine

1.1   CNTs: structure, discovery, properties, and diversified applications

CNTs are synthetic carbon-based NPs formed by a cylindrical architecture with a polyaromatic array ranging their diameters within nanoscale and lengths up to microscale. Their discovery in the late-20th century by Iijima[1] occurred by adding metal catalyst particles to the carbon electrodes and posteriorly applying an electric arc from an electric field. They are typically classified as either (*i*) SWNTs, comprising one graphitic layer rolled up into a nanocylinder, or (*ii*) multi-walled CNTs (MWNTs), composed of multiple rolled sheets of graphene held therein by weak van der Waals bonds (vdW). Regardless of their number of layers, there is an intrinsic attribute to accumulate into bundles and ropes due to their extraordinary surface area by volume ratio combined with strong inter-tube vdW adhesion.[2] The skeletal arrangement of CNTs differs in chirality type, (*i*) zigzag, (*ii*) chiral, and (*iii*) armchair, while their electron-rich surface offers a diversity of possibilities for modifications and alterations. Both carbon-atom structural disposition and surface regularity influence their physicochemical, mechanical, and electronic characteristics (e.g., topology, young's modulus, hydrophobicity, agglomeration state, and electrical conductivity).[3-6]

The hollow tubes enable favorable filling room for smaller nanosized molecules to be either shielded from the environment[7] or transported to a particular site. The outer surface allows hydrophobic molecules to non-covalently adsorb onto it and other polar and non-polar covalent attachments. In addition, their exceptional properties (*e.g.*, high strength, durability, lightweight, electrical and thermal conductivity)[8] provide the means for diversified industrial and biomedical utilizations, including nanocomposite structural reinforcement for mechanical[9] and durability enhancement; adsorbent for environment acid gases removal[10]; electrode materials for high-performance hybrid energy storage device[11]; airflow sensor for smart textiles and wearable electronics[12]; and nanocarrier for targeting drugs to malignant cancer[13].

1.2   Applications of CNTs in Medicine

CNTs-based biomedical implementations in nanomedicine are expected to revolutionarily treat numerous diseases. They have extensively fostered research studies on drug and gene delivery, cancer therapy, films, biosensors, and tissue engineering.[8, 13] One counterpart view is that their pristine state poses potential toxicity claimed to be due to their aspect ratio, aggregation, high bio-persistence, and metal impurities.[14-16] Utilizing adequate purification, cutting, and attachments on the outer-surface tubes of either polar functional groups (*e.g.*, carboxylic acid[17] or amide), polymers (*e.g.*, polyethylene glycol (PEG)[18-21], chitosan (CS)[21-23], and peptides[24-31]), or therapeutic molecules (*e.g.* doxorubicin (DOX)[32-41]) can ameliorate CNTs low aqueous compatibility and attenuate their toxicity potential and bundle formation propensity.[41-51] Recently, although indications of dispersant-sensitive lung accumulation in mice by Zhang et al.[16], wherein it was 1–2% for bovine serum albumin (BSA) and 15% on

day 1 increasing to 5% on day 90 for PEG, no such sensitivity on the *f*-SWNTs complex was found in the liver and spleen. Despite the reported slight hepatoxicity, their system has been pointed out as non-toxic. Other CNTs use problems in medicine are their size uniformity that could affect clinical reproducibility and surface defects *via* covalent modification that alters properties, despite the last augments blood circulation and biocompatibility.

1.2.1 Drug Delivery

Anticancer drugs' incapacity to treat only cancer-affected tissues, also harming healthy cells, causes patients severe complications after treatment. Drug delivery systems are envisioned to limit patient side effects and elevate drug bioavailability, especially for highly hydrophobic agents, by employing nanoplatforms for effective, controllable, and localized dosages in a prearranged rate and manner.[13, 52, 53] In that sense, CNTs are a remarkable candidate for delivery cargos due to their superior surface area, chemical stability, inner-cavity encapsulation, targeting specificity, drug loading, and cell membranes penetration (without cell death) abilities, aside from their interaction capacity with both drugs and biomolecules, either covalently or non-covalently, through vdW, hydrophobic, or electrostatic forces.[22, 52] Designing non-toxic CNT-based approaches that can be eliminated from the human circulation *via* the renal excretory route without adverse reactions are intended by researchers[54-56].

Current *in silico* and experimental research findings have displayed insights into the adsorptive effects of anticancer drugs on pristine and functionalized CNTs (*f*–CNTs) towards their transporting viewpoint, even evaluating comparisons between pristine and *f*–CNTs' performance. For example, a density functional theory (DFT) study[41] demonstrated

that functionalization of the armchair CNT indicated improvement of the CNT–DOX adsorption strength and stability in an exothermic and thermodynamical process. In contrast, the pure CNT sidewall was found unfavourable to the DOX energetic behaviour. The COOH–tube presented the best evident intermolecular H-bonds than in pristine and hydroxylated–tube systems, improving physisorption stability and fixation. They also observed that the flow of electron motion eventuated from a drug to the CNT. Dacarbazine (DTIC)[42] and vinblastine (VLB)[57] have also been conjugated on the pristine and the carboxylated CNTs, both armchair (10,10), revealing spontaneous encapsulation regardless of surface modification presence or type. However, considering drug transportation prospects, VLB entrapped inside the tube could indicate a lower delivery potential to the proper site of action between α–β tubulin.

Some studies, such as Kamazani et al.[58], are assessed only for the CNT and drug conjugation. They developed an *f*-carboxylated–MWNT combined with bromocriptine (BRC) nanofluid to mitigate drug dosage and eventually alleviate the BRC adverse effects. Their system exhibited an improved efficiency compared to the free drug in the *in vitro* anticancer activity by impeding the multiplication of the A549 & QU-DB lung cancer cells by apoptosis at a lower dose (compared to the pure drug and necrotic effects), and no harmful action at a high dose in the normal MRC5cell line. The mechanism of DOX release from the *f*-MWNT (processed in nitric acid) by Chudoba et al.[39] has shown competent drug release at pH 5.4 of almost 90% after 20 min, whereas that at neutral pH condition has not eventuated a release action, maintaining the aggregation level invariable.

Whereas other nanosystems are designed to constitute more than one surface functionalization group (*e.g.*, drugs, targeting moieties, synthetic polymers, and genetic

4

material) to mitigate properties for use in smart drug delivery systems, such as hydrophilicity, bioavailability, biocompatibility, and drug release. For instance, a targeted DOX delivery complex[46] was proposed as a strategy aimed to be cancer-cell selective on Man-receptor overexpression (*e.g.* HepG2 liver cancer cells). Their system was composed of the *f*-carboxylated–SWNTs covalently connected with acid-labile linkage and mannose (Man) (targeting agent for Man receptors) and conjugated with DOX. The authors presented that the DOX release profile was pH-triggered. Another work by Lyra et al.[59] described their DOX delivery system using acid-treated MWNTs non-covalently drafted with guanidinylated dendritic molecular transporters and hyperbranched polyethyleneimine (PEI) (types GPEI5K and GPEI25K), wherein the guanidinium moieties increased watery affinity for assuring outstanding colloidal stability. The synthetized complex presented high selectiveness opposing the tumorized cell growth (non-apoptotic), using aggressive DOX-resistant DU145 and PC3 human prostate carcinoma cell lines, and enhancement of cell-penetrating capability by assessing intracellular uptake of DU145 human prostate cancer cells and HEK293 normal human cell lines. Their DOX–MWNT–GPEI complex also revealed pH sensitivity and higher therapeutic efficacy (DOX encapsulation efficiency up to 99.5%) compared to the bare DOX. A nanocomposite designed by Tan et al.[21] with the short, oxidized MWNT–COOH coupled with betulinic acid (BA) and non-covalently wrapped with several hydrophilic polymers (*i.e.*, either of CS, PEG, tween 20, or tween 80) unveiled no cytotoxic effects on the normal embryonic mouse fibroblast cells (NIH/3T3 cell line) with dosages up to 100 μg mL^{-1}, as well as enhancement of the CNT solubility and dispersibility in phosphate-buffered saline aqueous media. Insights of an *in silico* loading-releasing study at different pH settings were highlighted by Khoshoei et al.[22], which model contains either

DOX or PTX on the *f*-carboxyl–SWNT using trimethyl chitosan (TMC) polymer. They emphasized that TMC's positive charge surface facilitated the DOX release at low pH tissues (as in cancerous) and promoted higher H-bonds in both acidity and neutrality (as in blood) media. DOX could be successfully adsorbed onto the *f*-SWNTs, and the highest aqueous compatibility was achieved for the PAX on *f*-tube at blood pH, inferring that pH-responsive polymers are appropriate for DOX transport. The computational kinetics models demonstrated that the DOX release mechanism is controlled by Fickian diffusion. The releasing profile and adsorption in both neutral and acidic pH of the system consisting of the armchair (12,12) SWNT non-covalently tagged with either tryptophan (Trp) or folic acid (FA), or both on the tube, evidenced a pH-triggering behaviour and protonated state of DOX dependence.[40] Another interesting release drug research work of Wolski et al.[32], containing DNA material, emphasized the pH-sensitive DOX locking mechanisms of the cytosine-abundant DNA segments covalently attached to the (20,0) CNTs complex. In the drug encapsulation at neutral pH, the blocking ability of DOX against spontaneous leave to the media occurred due to its preference for the strong knot-like intercalation between the random-coil genetic fragments. On the other hand, the DOX molecules were liberated outside the CNT entrapment at acidic pH since the DNA's folding into *i*-motifs led to a substantially weakened interaction strength between DOX and other systems constituents.

The releasing process of drugs in CNT-based systems can be improved by doping. Abbaspour et al.[60] revealed that the antitumor cisplatin releasing process of the N-doped (15,0) CNT, utilizing several iron nanowire and nanoclusters, pointed out an attractive potential towards CNT–drug encapsulation and subsequent appropriate transportation. Interestingly, they concluded that the CNT doping significantly influenced the agent-

releasing rate regardless of the constitution. Similarly, excellent release control of gallic acid (GAL) after doping the molecularly imprinted polymer (MIP) composite with SWNTs and polyhedral oligomeric silsesquioxanes (POSS) presented boosted GAL release.[61] Other nitrogen-doped CNT nanomaterials have been shown promising harmless cellular results for drug delivery and anticancer immunotherapies, such as in Burkert et al.'s study[62].

The addition of biological-based polymers (i.e., proteins and peptides) conjugation onto CNTs in the drug delivery view has also drawn attention in research to understand the competitive drug adsorption between peptides and CNTs, therapeutic release enablement, biomimicry[26], and overall improvement of physical-chemical and biological properties of CNTs. Tohidifar & Strodel[63] discovered that PTX on the zigzag (21,0) SWNT, in the presence and absence of PW3 peptide chains (sequence (NH_2)–WVWVWVKK–(COOH)), exhibited strengthened PTX bounding efficiency in the presence of the peptide; however, this drug binding preference was towards the f-CNT sidewall, *i.e.*, (–OH), (–COOH), rather than binding onto the surrounded peptides. An MD and metadynamics simulation work by Haghi et al.[64] searched the DOX binding onto the armchair (16, 16) pristine CNT in the presence or not of the cell-penetrating poly(L-histidine) (PLH) peptide. They determined that the DOX–CNT–PLH nanohybrid adsorbed on the phosphatidylcholine (POPC) membrane in neutral pH, but not in acidic conditions due to the strong CNT–drug interaction, acting fairly as smart drug platforms. This peptide on the CNT's surface improved the drug loading capacity by increasing the drug–carrier LJ interaction and presented a more beneficial drug release profile at lower pH.

Controllable or stimulated drug transportation advances with various stimuli-responsive parameters have been significantly studied. Madani et al.[65] proposed an implantable,

optically controllable drug platform strategy containing DNA-wrapped (9,4) CNTs with liposomes embedded into a 3D alginate hydrogel. Their obtained complex benefits from the unique near-infrared (NIR) optical and electronic properties of semiconducting CNTs. A drug release can be induced by applying an external NIR laser stimulation adjusted to a specific optical resonance on a stimuli-reactive moiety, causing a physical or chemical change in the carrier segment. The liposomes offer distinct advantages as nanocarriers, such as compatibility with hydrophilic and hydrophobic drugs, biocompatibility, and tunability. Minimal toxicity was noticed in RAW 264.7 macrophages *in vitro* using their system. Bibi et al.'s investigation[66] presented the entrapment efficiency and sustained delivery of the alginate–CS–MWNTs nanocomposite as an ibuprofen release platform with a successful encapsulation (88%) and a sustained drug release delivery (68% in controlled 6 h), besides being pH- and temperature-sensitive. The drug release profile from the nanohybrid was improved in simulated body fluid than gastric fluid, and greater temperature generated the drug–nanocarrier desorption while increasing crosslinking and charge density of the obtained material decreased this feature. In addition, a standard stimulus using MWNTs is to tune them by a magnetic field. Anticancer 5-Fluorouracil (5-FU) binding onto either the pristine or the chloromethylated semiconductive (8.0) SWNTs was found to be physical and exothermal, not affecting the drug's structural integrity. These SWNTs were uniquely suitable for 5-FU carriers with safety indications to properly transport the drug to the target by magnetism. Associating the *f*-SWNTs with 5-FU drug acts as a bipolar semiconductor, which can also be utilized to guide the drug *via* an external electric field.[49] The system composed of epirubicin (EPI) and Fe_3O_4 molecules on the MWNTs, elaborated by Suo et al.[67], has shown sustained release, prolonged drug EPI lifetime, and enhanced antitumor and

cytotoxicity activity under external magnets use than compared to its free EPI performance, according to the *in vitro* and *in vivo* results. Their complex was indicated as an effective intravesical instillation agent transport for bladder cancer therapy. Likewise, the DOX-decorated MWNTs covered with Fe_3O_4 NPs nanohybrid displayed sustained drug release and an augmented drug release time, enabling decreased dosing frequency. The magnetism-controlled system repressed the growth of bacteria (Gram-negative/Gram-positive bacterium, *Escherichia coli* and *Bacillus subtilis*) even at a lower drug concentration and refined the drug bioavailability and efficiency.[38] Gangrande et al.[68] proposed an injectable silk-incorporated *f*-FA–CNT hydrogel for DOX transport with higher bioavailability for targeted cells and side effect fading in the non-targeted cells for localized intra-tumoral delivery to drug build-up at the required location for an extended period. The acidic tumor pH and NIR light excitation inducement prompted the SWNT–FA–DOX release for 14 days, which was endocytosed by FR^{+ve} cancer cells to provoke apoptosis. H-bonding and electrostatic interactions between the SWNT–FA and DOX were attenuated by high temperatures to stimulate the drug release. This work emphasized potential intertumoral implantation as a sustained, targeted, localized, and external-stimuli-trigged system for DOX release to limit therapy complications against cancer.

As these NPs can frequently be taken up by cells without the immune system recognition against infectious and viral diseases due to their small size and high aspect ratio, other prospective CNTs-based targeted drug transportation systems apart from fighting cancer are exploited, including for immune augmentation, insomnia, bacterial resistance, and COVID-19 infection treatments. It has been developed an MWNT-CS complex encapsulating the immunostimulant Hericium Erinaceus polysaccharide (HEP), which results in mice

peritoneal macrophages determining the humoral immune response could be effectively regulated by the complex.[69] The PEGyled HiPco-SWNTs (HiPco: high-pressure carbon monoxide process) by Kofoed Andersen et al.[19] were non-covalently linked to either siRNA (targeting NOTCH1 gene) or anti-inflammatory drug methotrexate (MTX), or both, to form conjugates with higher drug efficacy. They showed that the system interestingly reduced the associated toxicity of MTX by suppressing targeting specificity to immune cells, mainly B cells, demonstrating this complex potential for drug delivery, specifically for immune cells involved in rheumatoid arthritis. Their *in vivo* assessment for free HiPco-SWNTs revealed accumulation in arthritic joints. Yu et al.[20] built an innovative multifunctional nasal gel matrix for drug nanoplatforms to act against insomnia to lengthen zaleplon's action time and efficiency. Since sleeplessness provokes nerve damage and CNTs may present certain neuroprotective effects, these NPs are suitable nanocarrier alternative for insomnia-drug transport to increase zaleplon bioavailability to cross the blood-brain barrier (BBB). The PEGylated SWNT–zaleplon approach can suitably protract its adequate action time in a balanced manner to not affect a next day patient's regular performance with excessive sleep due to the quick release of the CNT–drug complex non-covalently bounded (i.e., weaker than covalently, being easier to release). The carbomer-based gel can extend the nasal retention time to improve therapeutic absorption, and its ion sensitivity can avoid nasal blockage. Zomorodbakhsh et al.[70] investigated a new technique to generate the isoniazid-loaded MWNTs for tuberculosis (TB) infection treatment. Compared to the pure drug, the methodology exhibited distinctly ameliorated antibacterial action against mycobacterium TB H37Rv and isoniazid-sensitive strains. A lethal effect was achieved at considerably lower doses (1/32 and 1/16 for respective strains) than treatment with pure isoniazid. That can

relate to a better penetration of nano-formulation to the bacterial membrane and enhanced delivery of isoniazid at lower doses, resulting in minimized bacterial resistance toward the typical form of antibiotics. This system has the potential to surpass antibiotic resistance, which is a consequent issue of the usual TB treatment. In addition, a modeling study[71] investigated the binding interaction of the accessible monomeric B domain of the severe acute respiratory syndrome coronavirus (SARS-CoV-2) spike glycoprotein to CNT for a better understanding of forthcoming drug transporting elaboration. The tubes changed the spike glycoprotein B domain binding site to enter cells, causing changes in the tertiary structure. This domain is preferred by the tube to minimize internal hydrogen bonds. Functionalizing the SWNT can affect the stability of the protein.

The drug-loading nanovehicle routes of administration significantly influence the CNT–anticancer-agent efficiency in localized treatments and biodistribution, such as by oral, intramuscular, and intravenous routes. Shi et al.[72] reported different administration routes and the results of their system (*i.e.* oxidized SWNT nanohorns, which is a derived-CNTs aggregate with closed ends) by using label-free multispectral optoacoustic tomography using. The outcome demonstrated: (*i*) the oral route: the biodistribution of the obtained nanomaterial was majority localized in the gastrointestinal tract and posteriorly excreted *via* the gut, while nearly no accumulation was observed in kidney, liver, blood and spleen; (*ii*) the intravenous (IV) injection route: the sample mainly maintained in the spleen and liver, slightly was found in the kidney, and hardly any was perceptible in the intestine; (*iii*) the hypodermic and intramuscular injection route: almost no amount could be noted in the spleen, kidney or liver, presumably owing to its low absorption rate. Furthermore, the oral route of several types of CNTs has been inferred by Chen et al.[73] as a growing intestinal

permeability, favoring several inflammatory responses and modification in gut microbiota in mice. Ye et al.[17] published their prospective transdermal drug transportation work of ketoprofen-incorporated in *f*-MWNTs that presented good skin penetration of ethosomes (ex vivo permeation of rat skin) and *in vivo* pharmacokinetic characteristics. The accomplished complex had excellent drug loading of NPs, as well as dispersion properties and stability enhancement of ketoprofen. Overall, there is an utmost necessity for further toxicity and pharmacology studies of CNTs for further research prior to clinical settings.

1.2.2   Gene Delivery

Innovative CNT-based have been researched towards gene delivery implementation[13]. Recently, a synthesis investigation of a modified amylose derivative poly(L-lysine) dendron (ADP) and tumor necrosis factor-alpha (TNFα) on the SWNTs complex[74] for gene delivery/photothermal therapy (PTT) of colorectal cancer indicated good aqueous dispersion stability, high cell viability, gene transfection competence, and enhanced antitumor outcome promoting TNFα release from the nanohybrid and photothermal effect by NIR-trigged irradiation. Their ADP–SWNT–TNFα presented cancer growth and metastasis *in vivo* and *in vitro*, suggesting impressive optimistic indications in favor of tumor therapy. Zhao et al.'s work[75] also suggested a synergistic PTT/gene therapy (GT) association. A self-assembly conjugation of peptide lipid (PL) and sucrose laurate (SL) to the SWNTs and the MWNTs, loaded with therapeutic siRNA, demonstrated excellent biocompatibility and photothermal effect. The highly efficient complex inhibited cancer development by silencing survivin expression while performing photothermal features trigged by NIR. The siRNA-containing system acted appropriately, successfully suppressing some tumors' development *in vivo* and *in vitro* and outstanding temperature responsivity (due to the lipids-layer phase transition)

for gene release inside malignant cells. A nucleic acid transport study by Li et al.[76] for cancer immunotherapy using different brush-grafted chemistries (*e.g.*, density, polymer-chain length, others) of cationic poly(2-dimethylaminoethylmeth-acrylate) on the CNTs revealed that the nucleic acids (*i.e.*, siRNA, ssDNA, and plasmid) exhibited structure-dependent impact in the biocompatibility, cellular uptake, and silencing efficiency *in vitro*. The brush-coatings eminently influenced the binding efficiency of different genetic material by comparing several architectures, wherein the best binding was the dense long, sparse long, and sparse short brush-covered CNTs.

Moreover, there are studies for targeted, simultaneous co-delivery for both drugs and gene transport.[34, 58, 77, 78] Taghavi et al.[77] established a novel gene co-transportation complex for adenocarcinoma combinatorial therapy. It consisted of the SWNTs conjugated with plasmid encoding survivin (psur) shRNA and prodrug SN38 wrapped with PEG, PEI, and cancerous-targeting peptide PNC27 against colon adenocarcinoma. The delivery system showed an effective and harmless synergistic SN38-psur-shRNA transport. A lethal effect of the injected mice was a consequence of SN38 absence according to the *in vivo* results, indicating reduced the mice pulmonary complications of SWNTs. The system of the CD44v6-O-MWNTS-coupled gemcitabine and CXCR4 siRNA was reported by Yin & Qian[78], which could effectively load gemcitabine or oxaliplatin, and CXCR4 siRNA absorbed by malignant cells. It presented distinguishable *in vitro* and *in vivo* preventive effects against ovarian cancer increase. Noteworthy, CXCR4 is expressed in various malignant tumors (*e.g.*, breast, prostate, and ovarian tumor), while CD44v6 is not expressed in normal ovarian tissues but is expressed in ovarian epithelial carcinoma. Another study by Rabiee et al. [34] presented a carbon-based nanosystem integrated with CS–alginate–MWNTs into the reduced graphene

oxide (rGO) to supply proper space for in situ growth of $CoNi_2S_4$ between carbonic layers. Capping surface treatment with genetic material and agents from leaf extracts was aimed at stabilizing the ZnO NPs. Minimal cytotoxicity and significant drug–gene-loading capacity of the attained complex was observed. The DOX coating was enhanced with space selection and space accumulation techniques with the beneficial cone-shaped $CoNi_2S_4$, demonstrating that the new co-discharge system is secure and bioactive.

1.2.3 Cancer Therapy

There are ambitions to focus on the research community to tackle cancer utilizing tumor-targeting CNT-based systems, especially employing PTT, chemotherapy, radiation therapy, hyperthermia, immunotherapy, and combinational therapies.

1.2.3.1 PTT

Recently, auspicious approaches using CNTs for PTT are emerging since they are photothermally active due to their intense NIR-region absorption and NIR photothermal conversion capacity. The PTT overall method has reduced side effects and has a non-invasive character, minimal toxicity, short treatment period, fast recovery, and high ablation efficacy. The PPT healing precept is to introduce photothermal materials into cancerous life forms and transform light energy into heat energy from a particular external light source to attain the "burning" of the tumor.[75, 79] Su et al.[80] created a photothermal fiber system comprising Yb^{3+}/Nd^{3+} doped lanthanide titanate (LTO) matrix and CNTs for temperature monitoring by upconversion luminescence of Nd^{3+} ions and heating in PTT for tumor ablation. The nanocomposite under 980-nm laser inducement and temperature-sensitive conditions could successfully and accurately reach cancer in mice. Nagai et al.[79] revealed incorporation of anti-TRP-1 antibody into SWNT embedded in maleimide gel (*i.e.,* furan-

protected maleimide methacrylate and PEG methacrylate (PEGMA) monomers), which complex was posteriorly conjugated with streptavidin and biotin was onto the maleimide, by utilizing NIR in PTT effect for selectively reaching and successfully destroying active targeting of B16F10 melanoma cells cancer cells *in vitro*.

1.2.3.2 Chemotherapy

Chemotherapy using chemotherapeutic drugs is one of the most traditional and commonly used cancer treatment alternatives, which is necessary for a patient's advanced cancer stage, being a variable treatment, often with unfavourable results, that causes severe adverse effects. CNT-based complexes have been studied to aim for enhanced non-invasive, accurate, and effective chemo-treatments. Fan et al.[81] studied hyaluronidase of the DOX-coated nanoprobes in tumor-bearing mice for pancreatic cancer to address the specific extracellular hyaluronic acid (HA) matrix barrier of this tumor type for better drug anticancer activity, the challenges of low bioavailability of chemotherapy agents, and insights of this tumor size during treatment. HA barrier eradication and the DOX-loaded nanoprobes increased the drug absorption into tumor with higher efficacy. Their SWNT–CY7–DOX (*i.e.* CY7 means cyanine fluorescent dye) transported DOX into the tumor *via* the enhanced permeability and retention (EPR) effect. Leyva-González et al.[82] developed the HA–oxidized–MWNTs filled with carboplatin (CPT) approach that indicated selective *in vitro* antitumor action and cytotoxic properties on human cervical adenocarcinoma (HeLa) and mammary adenocarcinoma MDA–MB-231 human tumor cell lines due to the intensified adherence to the CD44 receptor and succeeding endocytosis, improving the nanovector uptake *via* receptor-mediated. Whereas its cytotoxicity was not significant in normal cells compared with free CPT, exhibiting that the *f*-HA–CPT–CNT nanocomplex has

biocompatible vectors for drug transport with minimal cytotoxicity in normal cells and anticancer activity.

1.2.3.3 Radiation Therapy

Radiotherapy is also widely applied to support malignant-tumor treatments in clinics by employing radiation rays to eliminate directly or indirectly tumorized tissue cells through DNA double-strand breaks (DSBs) and subsequent cellular apoptosis. In contrast, it may also damage healthy tissues and organs, provoking severe health consequences for patients.[83] CNTs have been used as radio carriers to transport the proper irradiation in cancerous tissues and enhance the theranostics and treatment. Gajewska et al.[84] explored the nanocapsules containing the f-NH$_2$–MWNT with methacrylic acid (MAAc) decorated with radioactive salts (*i.e.* isotopically enriched 152-samarium chloride (^{152}SmCl$_3$)) by arylation reaction for *in vivo* radiotherapy delivery. The rodent's radioactive–f-MWNT biodistribution results indicated elevated lung accumulation, succeeded by liver and spleen, without any inner radioactive substance escaping to the bloodstream. Ali & Radwan's approach[45] could be useful as an anti-inflammatory for patients during radiotherapy since the oral intake of resveratrol (RES) incorporation in the f-MAAc–MWNT system by pH-controlled radiation enteropathy in rats demonstrated a decrease in the oxidative stress, inflammatory, and apoptotic markers. That presented overall better potency, bioavailability, and prolonged release (by pH changes) at the desired site. Yang et al.[83] developed the iron-palladium (FePd) and CNTs strategy, possessing respective radiosensitization and crossing biological barriers capacity. As the tube carriers would deliver FePd into the cells, more abundant reactive oxygen species (ROS) induced by the complex and further tumor cells apoptosis would be achieved by stronger radiation energy absorption. The FePd–CNTs material extended the

circulation time *in vivo* with satisfactory therapeutic activity by pharmacokinetic outcome, while *in vitro* experiments evidenced biocompatibility and significant radiosensitizing impact.

1.2.3.4 Immunotherapy

The activated-immune cells by proper immunotherapeutic inhibitors (*e.g.*, nivolumab and durvalumab) eliminate several cancerous cells by apoptosis and necrosis in immunotherapy. Qiang et al.[85] built a new immunotherapy durvalumab–CNT–PEI–aptamer–siRNA chimera nanocomplex for the Trem2 siRNA delivery. Their methodology stimulated anticancer immunity to successfully fight against hepatocellular carcinoma (HCC) tissues, as emphasized by their *in vivo* and *in vitro* experiments, not affect normal liver and lungs. Their system provoked HepG2 cell apoptosis and T cell proliferation and showed the durvalumab control for a 48-h sustained release. Moreover, considering reinforcing apoptotic and immunotherapeutic properties, a recombinant fragment of human surfactant protein D on the nanocarrier strategy (CNT–rfhSP-D) by Khan et al.[86] was applied against K562 leukemic cells, inducing apoptosis in eosinophilic cells, by targeting intracellular signaling cascades. The complex has drug potential in targeting leukemic cells.

1.2.3.5 Combinational Therapies

Combinational tumor therapies attempt to ameliorate the tumor-curative effect since monotherapies are usually insufficient to exterminate cancer tissues, frequently causing cancer to reappearance.

Chemo-PTT (*i.e.* chemotherapy and PTT) has been considered for synergistic prospects. Das et al.[87] showed their injectable approach, a nanocarrier of CNT embedded into *β*-cyclodextrin (pH- and temperature-sensitive polymer). The antiangiogenic effect *via*

curcumin and DOX hydrochloride addition exhibited synergistic antitumor action and FGF2 and VEGF growth factor reduction (angiogenesis inhibition), while *in vivo* tests, CAM (chorioallantoic membrane assay), confirmed multiple mechanisms for anticancer activity. A sustained release profiles of the two agents were observed over 30 h, wherein DOX reached a release rate of 90% under tumor microenvironmental conditions, while curcumin release rate was 85% under high temperature and at neutral pH. The developed material on HeLa and MCF-7 cells exhibited a cell mortality rate of 70% that surpasses up to 80% with photothermal inducement *in vitro*. González-Domínguez et al.[88] formulated a theragnostic *f*-CNT–nanocellulose (NCC) colloidal nanohybrid covalently attached to fluorescein, targeting agent FA, and chemotherapy capecitabine drug (against colorectal cancer). The produced proliferation-resistant nanohybrid demonstrated a better Caco-2 cancer activity than bare capecitabine, wherein, interestingly, capecitabine presence was not required to mediate against cancer proliferation since type-II NCC destroys selectively and inherently colon cancer cells. Moreover, the SWNT–II-NCC can be favorably applied for its no toxicity, dispersibility, and imaging capability.

The dual functionality combination of PTT and GT, and combinatorial PTT and immunotherapy also improve tumor-fighting activity. Chen et al.[74] used cationic amylose for the SWNTs coating in a colorectal cancer PPT and GT association. Similarly, Zhao et al.'s CNT–siRNA approach[75] revealed auspicious tumor-inhibiting growth platforms by silencing survivin expression while exhibiting photothermal effects (conversion efficiency of ~60%) under NIR light for gene delivery-PPT treatment of the heat-responsive and photothermal lipid-loaded siRNA-coupled SWNTs and MWNTs. A facilitated gene release inside tumor cells occurred owing to PL and SL coating, besides presenting any evident

cytotoxic effect at concentrations as high as 60 μg mL^{-1} or toxicity to mice. The effective cellular internalization was confirmed after they observed NPs' presence in the cytosol of HeLa cells. In addition, immunotheranostic has shown synergistic outcomes enabling cancer remission and attain immunologic memory, then combined with PTT, as exhibited by McKernan et al.[89] insights, can promisingly qualify towards metastatic breast cancer inhibitory treatment. Their work was a targeted SWNTs complex using an immune checkpoint inhibitor, which bounds to cell proteins that regulate the patient's immunological reaction to cancer. The studied PTT with the SWCT conjugated with targeting protein ANXA5, and non-cytotoxic T-lymphocyte-associated protein 4 (anti-CTLA-4) agent showed relatively notable non-lethal rate using aggressive metastatic breast cancer mice and a tumor average maximum temperature of 54 °C (duration 175 s). Noteworthy, the organ biodistribution was studied over 4-month administration revealed, despite remaining in the SWNTs presence, no side effects or apparent tissue toxicity were found.

The associating use of photoacoustic therapy and PTT procedures has also been evaluated *via* CNTs-based photonic suspensions with active agents to diagnose and treat diseases concurrently or after. For instance, Golubewa et al.[90] manifested that glioma C6 cells were capable of accumulation of the salmon-DNA HiPco-SWNTs suspension (stable for up to 4 months) of relatively large bundles. That allows photo-stimulated cancer cell death using picosecond laser irradiation, and, most importantly, only cells with agglomerated SWNTs are annihilated in solution; otherwise, individual tubes have no photoacoustic-induced activity. They successfully exhibited that their system can be applied to visualize the cancer cell and its photo-induced destruction.

Furthermore, research cases including the CNTs-based cancer hyperthermia method have been published, in which it is based on a temperature increase that causes the kinetics of a chemical reaction since CNTs convert NIR radiation into hyperthermia for PTT. Wang et al.[91] evidenced their nanoplatform, the f-MWNTs with FA–PEG–NH_2 coated with MnO_2–Ce6, for magnetic resonance imaging (MRI)-oriented photodynamic (PDT) and PTT. Ce6 is a photosensitizer that initiated PDT under the NIR beam (causing cell destruction *via* PTT), and MnO_2 disintegrated H_2O_2 to generate O_2 and consume high glutathione (GSH), resulting in chemodynamic therapy (CDT) and subsequently improving the PDT. The synthesized material was successfully captured by tumor cells and inhibited its growth as well as ablated cancer *in vitro* while it had rapid transport of Ce6 and MnO_2 at low pH. Surface modification and EPR caused minimal side effects. Liu et al.[92] reported a study of mild hyperthermia-enhanced intervention by an enzyme of the PEGylated-MWNTs–PEI–Fe_3O_4 incorporated in glucose oxidase (GOx) nanocomposite in favor of an integrated CDT and PTT. Their material resulted in tumor cell apoptosis through a high concentration of intracellular H_2O_2 and acidity in the tumor tissue by the catalysis of GOx. The 808-nm laser heat in mild hyperthermia caused better CDT efficacy. Chall et al.[91] describe their technique for cancer tissue penetration and super heat utilization using low-level microwave irradiation (advantageously penetrating deeper than NIR) for hyperthermic cellular ablation in mice using an antibody (Ab) to target cancer agents on MWNTs. They injected Ab–MWNTs without affecting adversely healthy mice cells, and no toxicity presented in the absence of microwave incitement.[93] A study[94] exploited an *in situ* magnetic, porous nanocomposite scaffold, *i.e.*, the MWNT/Fe_3O_4 into the gelatin/akermanite matrix, that displayed a high photothermal effect (from both NPs) using varying NIR intensities and laser time. A

boosting biocompatibility effect was observed in G292 osteoblastic cells, protein adsorption, and the elastic modulus and compressive strength values, useful for PTT and bone tissue engineering applications.

1.2.4   Tissue Engineering

Regenerative medicine has been diversely and extensively examined tissue scaffolds, cells, and others, aiming to heal, maintain, enhance, and substitute various biological tissues (*i.e.*, skin[95], bone[96-101], ligament[102], and others).

David et al.[103] wound-healing dressing with enhanced antimicrobial and biocompatible performance was successfully formulated as a nanocomposite of cellulose acetate-collagen films containing MWNTs coupled with TiO_2 NPs that restrained proliferation of both Gram-positive and Gram-negative strains. Khalid et al.[44] probed antibacterial action and regenerative bandaging, and their MD simulations checked the expression of genes impact of the biocomposite containing by the *f*-MWNTs-incorporated within 3D microporous matrix of bacterial cellulose (BC). Using an ex-situ immersion method for synthesis, they found the implantation of the CNTs instituted noticeable repressing effects against *Klebsiella sp.*, *E. coli*, *P. aeruginosa*, *S. aureus* to BC, better compared to standard bactericidal drugs. This novel composite performed as an efficient healing biomaterial to regulate infection and expedite the diabetic wound restoration, besides being a physical obstacle and possessing moist retention functionality. Zhang et al.[104] divulged a rapid, effective JWCNT (joint-welded CNT)/hydroxybutyl CS sponge dressing to approach the weak mechanical, absorptive, and antibacterial properties of the hemostatic agents, being a beneficial biomedical alternative in support of uncontrolled hemorrhage since the complex's features of blood absorption (porous structure), blood compatibility, high elasticity, blood-

maintaining action, and good antibacterial activity. On the other hand, the nanomaterial's antiseptic potential accelerated blood clotting *in vitro* and hastier hemostasis time *in vivo* than the traditional gelatin sponge.

Bioprintable studies have shown unprecedented tissue-engineered ideas. A bio-adhesive was designed by Bon et al.[93] via incorporating regenerated silk (RS) obtained from *Bombyx Mori cocoons* into the *f*-carboxyl–CNTs to obtain their functional 3D printable bio-adhesive ink by seeding and proliferating human skin fibroblasts for implantable devices. The proposed *f*-CNTs–RS composite was electrically controllable, with impressive biocompatibility and adhesive properties on wet biological substrates. As their system can be managed by electricity, constructing a piezoelectric implement applied to a rat proved useful in supervising the self-powered respiration *in vivo* strategy. Moreover, tissue replacement's future aims to join with the transplanted native organ tissue to enhance cellular viability and preserve or upgrade the tissue role. A cardiac scaffold of a non-mulberry silk-based conductive bioink with CNTs was established by Mehrotra et al.[105], which such shear-thinning biolink facilitated the shaping of an accurate anisotropic vascularized structure akin to the natural heart tissue. The outstanding conductive and mechanical properties of CNTs advantage maturation, synchronous beating, and mechanotransducive action to the cardiomyocytes, showed an advance towards cardiac tissue development.

Conductive scaffolds for regeneration advancements are investigated, such as in Bai et al.'s study[106], which comprised the bioactive SWNT/extracellular matrix hybrid hydrogels. The pristine tubes were well dispersed in the hydrogel due to the matrix proteins that act as biophysical cues to activate the integrin-related pathways. An *in vivo* assessment of the injectable nanocarrier scaffolds that were utilized to deliver stem cells (concerning mice

myocardial repair *via* reconstructing an integrin-sensitive niche) emphasized ameliorating cardiac differentiation and maturation (12.5 ± 2.3% vs 32.8 ± 5%) of stem cells. The elaborated complex could be used as a scaffold for cardiac tissue construction and injectable stem cell transporting carriers. Yang et al.[107] synthesized a retinal sheet of the CNTs and poly(lactic-*co*-glycolic acid) (PLGA) that can augment retinal cell therapy. This polymeric scaffold displayed indications of restoring development along the optic nerve in the retinal ganglion cells, besides having extraordinary electrical conductivity, biocompatibility, and biodegradation compared to PLGA scaffolds, which all suggested their positive prospect for retina injury, repair, and regeneration. Zheng et al.[108] revealed a new approach for non-therapeutic, non-invasive neural regeneration neural tissue recovery, composed of photoacoustic PEG–CNT (CNTs have photoacoustic properties) in silk fibroin scaffold. That allowed neural inducement and neurite outgrowth by absorbing 1030-nm NIR-II laser and its light energy to acoustic conversion that incites neurons cultured on the CNT/silk matrix. Their scaffold biocompatibility was proved *in vivo*.

Similarly, the scaffold of polydopamine (PDA)/polycaprolactone (PCL)/CNTs fibrous scaffold[109] loaded with brain neurotrophic factor could beneficially nurture sciatic nerve and functional reconstruction according to the *in vitro* and *in vivo* (rat sciatic nerve) results and also benefit from the sustained release of the factor over 28 days. For artificial tendons[102], a semi-interpenetrating polymer network (IPN) study of polyurethane (PU) with poly acrylic acid (PAA) semi-IPNs containing the MWNTs nanocomposite was aimed for proper elasticity, biocompatibility, and relative electrical conductivity (nerve tissue). Accordingly, optimize variables by the response surface methodology (RSM) to produce a material with a reasonable arrangement as a native tendon, in which the best combination results were 20

wt.% of PAA, 8.75 and 16.25 mol.% of crosslinking agent of 1 wt.% and 3 wt.% of the MWNTs. The carbon-based NPs agglomeration induced electro-carried current due to their random distribution threshold was more than 1 wt.% and their addition to PU–PAA affected the biocompatibility.

Efforts also have been made to develop bone repair biomaterials.[96, 97] Another recent suggestion is the biomimetic cuttlebone polyvinyl alcohol (PVA)–CNT–hydroxyapatite (HAP) aerogel scaffolds to enhance bone reconstitution by Liu et al.'s research[110]. This porous nanostructure exhibited superior mechanical and bone-renewing properties in 8 weeks. The last occurred without the contribution of endogenous cytokines, and the boosted osteogenic-marker differentiation (adhesion, proliferation, and gene expression) MC3T3-E1 cells *via in vivo* calvarial defect model of SD IGS rat. Wang et al.[98] emphasized that their PEG–MWNT–polylactic acid (PLA) nanofibers as drug-incorporated nanofibrous have excellent prospects for scaffold in bone tissue reformation. The rat bone marrow stromal cells (rBMSCs) were introduced into the resulting nanofibers. The tubes' function was reinforcement, uniform drug incorporation, and induce osteogenesis, while the pristine PLA fibers mainly coated the osteogenic dexamethasone (DEX) on their surface, and the drug favored effectively osteogenic differentiation and improved mineralization of rBMSCs on the nanofibers. The releasing rate and time of DEX were tuned by PEG quantity. Additionally, Huang et al.[111] described the strategy of alanine ethyl ester and glycine ethyl ester co-substituted polyorganophosphazene (PAGP) (rich in phosphorus–nitrogen) coupled with the CNT. The bone marrow mesenchymal stromal cells (BMSCs) modified with PDA films with their complex under electrical stimulus can generate significant osteogenesis

activity, suggesting that the combination of the conductive system with electrical stimulus may reach combined advances in osteogenesis.

Other structural studies have also been reported in research, such as in Oliveira et al.[112] that described the viable cells after the *ƒ*-carboxyl–MWNT treatment by employing stem cells from the human exfoliated deciduous teeth model, and such reached complex caused no superoxide dismutase action alteration, genotoxic, oxidative stress, and toxicity activity.

1.2.5   Biosensing and Bioimaging

1.2.5.1   Anticancer-related Diagnosis Biosensor

Recent studies have been showing propitious perspectives for biosensor and imaging development containing CNTs. Ma et al.[113] described their low-price, sensitive, and specific tetrahedral DNA nanostructure (TDN) system for high-action identification of circulating tumor DNA biomarker of AKT2 gene (metastatic and primary triple-negative breast cancer) employing an all-CNT thin-film transistor (TFT) biosensor. Its response for at least 35% for TDN-2T and 98% for TDN-4T (improved DNA hybridization competence) compared with single-stranded DNA probes, manifesting significant chances for direct quantification and label-free finding of ctDNA in blood. Karimi-Maleh et al.[114] suggested a green and sensitive DNA detection electrochemical biosensor for enhanced, accurate anticancer idarubicin amount traceability, favoring patient health conditions in chemotherapy. Their glassy carbon electrode (GCE) coated with Platinum and Palladium particles, Zinc-oxide–SWNT, and recognizing ds-DNA (Calf Thymus) substance (for element selectivity improvement), formed a nanocomposite aimed to find guanine base signals between ds-DNA on the electrode surface (ds-DNA–Pt–Pd–ZnO–SWNTs–GCE) and the intercalated drug, resulting in a notable idarubicin detecting effect within a concentration of 1.0 nM–65 μM. This drug

intercalation interaction into the ds-DNA guanine base binding was observed by molecular docking. Another innovative CNT-based electrochemical biosensor for a diagnostic probe has been traced for hypoxia glycolysis byproducts (H_2O_2/ROS)[115] released from human neoplastic cells. In many clinical trials and safety examinations, the method indicated sensitivity of >95% pathological equivalence results in testing more than 250 *in vitro* human tumor tissues and 57 *in vivo* in tumorized mice (after the *in vitro* formed breast tumors dissection) in an intraoperative real-time electrical sensing.

1.2.5.2   Disease Detection Biosensor

Advance identification of diseases can be beneficial for obtaining greater changes for early diagnosis and healing. In that regard, an utmost-sensitive, economical, and straightforward immunosensor technique for the Alzheimer's disease (AD) diagnosis *via* phosphorylated Tau 181 protein (highly AD specific biomarker) detection was elaborated[116]. Constituted with a carbon screen-printed electrode (C-SPE) of platinum NPs loaded with an improved electron-transfer antibody-binding f-aminated–MWNTs coating, the authors evidenced the superior p-Tau181 identification with a limit of detection of 0.24 pg mL^{-1} in a concentration range of 8.6 pg mL^{-1} to 1100 pg mL^{-1}. In addition, a study developed bacterial vaginosis (BV) quick diagnosis machine-learning biosensor chip (feasible certification precision of 87.5%) that distinguishably detected BV-related biogenic *via* either amine-negative or amine-positive samples. By applying several testing approaches and algorithms as well as pH sensing tests, their strategy indicated leads of field-effect transistors in over one-month stability for point-of-care prognostics of this disease.[117]

1.2.5.3   Viral Diagnosis Biosensor

The latest unique CNT-based methodologies for speedy SARS-CoV-2 (COVID-19) infection tests at the mass level application have been studied for proper early COVID monitorability. As reported by Pinals et al.[118], a hybrid biosensor employing non-covalently SWNTs bounded to the human host ACE2 protein, in which the last molecule has an effective binding affinity to the protein receptor-binding domain, manifested the spike-protein reading within 90 min and 73% luminescence reaction in 5s to 35 mg L^{-1} viral treatment and its further recognition time in seconds. Their non-covalent coating beneficially maintained the CNT fluorescence properties. Another COVID diagnostic tool presented to be 2–3 min, responsive, user-friendly, economical, quantitative-electrochemical, and NIR-optical sensitive[119], through saliva samples, by the development of the CNT printing on a Si/SiO$_2$ surface with the anti-SARS-CoV-2 using field-effect transistor (FET) of surface spike protein S1, offering a minimum retained sensing activity of 91.18%. The machine-learning systematic method of Kim et al.[120] also evaluated for quick SARS-CoV-2 virus catching the CNT-based thin-film properties and responsiveness of an immunosensor.

Moreover, an influenza viral sensing application was published as a pliable, competitive cost, smooth fabrication, reproducible, and electrical resistant, and immunosensor of C-SPEs for label-free evaluation of influenza viruses (H5N1, H7N9, and H9N2) detection. The paste-form electrode is produced with an electrochemical antibody placement on the *f*-COOH–CNT–polydimethylsiloxane nanocomposite, *via* 1-ethyl-3-(3-dimethylamino-propyl) carbodiimide and N-hydroxysuccinimid on paper substrate.[121]

1.2.5.4   Specific Biomolecule Detection Biosensor

A stable and fabricated-consistent NIR-fluorescent composite nanosensor, composed of colloidal engineered DNA-wrapped SWNTs embedded in PEG diacrylate hydrogel, applied in controlled injections *in vivo* intraperitoneal SKH1-E murine model, has shown selective sensing *via* DNA of two vitamins, the riboflavin (vitamin B2) and the ascorbic acid (vitamin C). The results were beneficial in unravelling building issues for intraperitoneal *in vivo* reading credibility, noise sources, and signal stability of these vitamins for an optimized vitamin-detecting utilization.[122] Another biosensor construction, for ease, thorough non-electrical-contact blood hemostasis analysis, was developed based on a CNT-paper composite (CPC) capacitance transcutaneous biosensor of vitamins utilizing NIR fluorescence, being useful for patient management who suffer from hemorrhages, aggressive treatments, or take antithrombotic. Their one-measuring capacitance signal methodology could synchronously estimate platelet count/function, hematocrit, and coagulation function, evidencing its effective monitoring possibility for various hemostatic conditions (*e.g.*, hemophilia and thrombocytopenia). Results emphasized fitting availability, sensitivity, and effectiveness in respect of the traditional thromboelastographic analyzer, with its high fringing field found permittivity changes in human blood on glass, leading to unnecessary use of physical and electrical contact.[123] Furthermore, a synthetic antibody of the polypyrrole (PPy)/MWNTs on screen-printed electrodes system for cystatin C (Cys-C) (*i.e.* an acute kidney injury biomarker) identification device has emphasized satisfactory, simple, cost-effective, and sensitive particularities for acute kidney injury diagnosis.[124]

1.2.5.5   Healthcare-monitoring Sensors

Recent works have shown the detection of the human body's signals for future perspectives on wearable wellness electronics. A remarkably optimistic strain sensor of an MWNTs–$Ti_3C_2T_x$ MXene–polyurethane (TPU) nanohybrid foam presented effective lightweight and sensitive strain sensing performance for tracking human movements (*e.g.*, joint and finger motion and vocal cord vibration). The results revealed a broad strain recognition range (~100%), a high sensitivity (gauge factor = 363, meaning great resistance responsivity to applied strain), excellent durable cyclic stability, as well as high flexibility and gas permeability that are close to those of skin, indicating a comfortability of wearing.[125] Another prototype is the remarkably sensitive, selective boron nitride nanotube/CNT nanohybrid for a reversible, self-enhanced chemiresistive identification of NO_2, without external heating necessity, which showed encouraging 33-day constancy performance at 200 °C to preserve CNT temperature. That indicated complete recovery after gas exposure and excellent electrical and thermal results for NO_2 sensing in the direction of smart clothing with wearable electronics production.[126] Cotton-fiber transistors based on the MWNTs covered with poly(3,4-ethylenedioxythiophene) (PEDOT) nanowires for the discovery of K^+ ions in the human fluid could also be the wearable biosensors for ion detection.[127]

1.2.5.6   Temperature-inspection sensors

A CNT-composite temperature-monitoring sensor has been reported[128] to measure on-skin temperatures. The heat mismatch between the CNTs and the matrix in high temperatures constrained the tubes, altering their electrical properties in a stable and consistent temperature-resistance correlation by promoting changes in the electrical resistance. The proposed biosensor exhibited satisfactory stable and reproducible characteristics under

multiple thermal loads, besides being flexible, wearable, and biocompatible temperature sensors appropriate for lab-on-a-chip devices or artificial sensory skin.

1.2.5.7 Imaging

A high-specific directed imaging technology to recognize inflamed atherosclerotic plaques before their rupture could impede heart attack and stroke consequences by determining the abundant arterial-wall immune cells (*i.e.* plaque inflammation) and diagnosing atherosclerotic injury. Using an injectable ultraselective CNTs (contrast agent) targeting Ly-6C^{hi} inflammatory monocytes and foamy macrophages, along with photoacoustic imaging through red-laser light into tissues, Gifani et al.[129] were able to accurately image susceptible plaques *ex vivo* in a mouse model that mimics human in-risk plaques. The uptake into only these fragile cells led to a localized SWNTs accumulation within the plaques, excluding healthy blood vessels. An *in vivo* imaging of the non-photobleaching, NIR fluorescent SWNTs with DNA (GT)$_{15}$ system[130] within the gastrointestinal track of *Caenorhabditis Elegans* nematodes (model organism for eukaryotes) was assessed to suppress their interference challenge from the vast-range visible autofluorescence challenge for imaging and track fluorescent proteins/dyes utilizing traditional beaming observation techniques. The uterus and intestine of the worms revealed potent autofluorescence over all visible spectra, whereas this effect was not found for the NIR wavelength range (>900 nm) from any organelles. The (GT)$_{15}$-SWNTs concentration adjusted the luminous level in the worms, presenting negligible long-term toxicity and non-phototoxic, and any heating consequence from the laser exposure was observed; hence, the CNT's bright signal was adequate for *in vivo* biosensing. Moreover, Langenbacher et al.[131] projected an approach of a single-chirality SWNT multiplexed imaging probes and studied their internanotube förster resonance energy

transfer (FRET) between two probes, and exciton energy transfer capabilities in live cells, indicating imaging potential of the single-chirality system and FRET probes for multiplexed cellular imaging bio-utilizations by their specific subcellular partitions. The functionalization of the (6,5) and (7,6) tubes was *via* polycarbodiimide polymers containing distinct capabilities through two-phase aqueous extraction.

1.2.6   Others

There are various other captivating classes of CNTs-based studies and medicine-related applications that have not been covered herein. For example, in cosmetics, there is a recent original skincare-emulsion product composed of the lignin, MWNT, and graphene oxide (GO) nanoadditives with improved sun protection factor and UV balance to preserve a healthy skin[132]. In the bio-coating field, a surface work with a designed fluorinated CNT superamphiphobic layer for effective (>97%), the long-lasting underwater anti-biofouling function has shown restrained biofilm growth and wear resistance from preventing bacterial and BSA adherence and deposit of *Escherichia coli*.[133] Positive indications for future use of CNTs for Alzheimer's disease therapies are expected since the effective inhibition of Aβ aggregation by the *f*-carboxylated–SWNTs presence, which is the disease treatment goal, and, interestingly, also the system caused the depolymerization of the Aβ mature fibrils due to the suppressing mechanism of the Alzheimer's amyloid-β protein (Aβ) misfolding.[134] CNTs have been studied as vaccine carriers, such as in the immersion vaccine application for enhanced immune responses against koi herpesvirus in vaccinated koi fish.[135] Due to the strong mechanical features, CNT-based nanocomposites for human implant performance improvement have been a common implement for structural reinforcement. One example is the research of the manufacturing variables to obtain enhanced properties of a biocompatible

ƒ-SWNTs in an ultra-high molecular weight polyethylene (UHMWPE) matrix proved that could be applied in case of the knee, cranial, or hip replacement needs.[135] Another example is a preventive medical device coating (*e.g.* in orthopedic implants), such as a carbon-infiltrated CNT sensitive to cell biofilm such as methicillin-resistant staphylococcus aureus bacteria, preventing serious post-surgery complications like periprosthetic joint infection.[136]

1.3　Summary

Researchers have dedicated their time to designing, optimizing, and fabricating promising biomedical CNT-based nanosystems with enhanced biocompatible, structural, thermal, electrical, optical, electrochemical, and electrochemiluminescence properties to tackle a variety of diseases. Numerous attempts to progress customizable drug and gene delivery systems have been developed through experimental and computational studies via solutions for smart, selective, controllable, and effective treatments. These systems aim to release targeting molecules into cells with localized dose control to reduce side effects for patients. Notably, in multiple cancer therapeutics, even in the combinational therapies, the advantages of CNTs as nanovehicles are not only for malignant tumor treatment with drugs and recognizing moieties but also applied in carriers for real-time cancer diagnosis and imaging with high resolution. Other biomedical devices also have excellent prospects for their implementations in medicine, such as biosensors for monitorability, and early detection and healing, aside from structural biocomposites and healing films biomaterials.

Although their notorious potential in medicine, several issues need to be addressed before large-scale use in medicine, especially with respect of the human health hazard associated with the exposure. The CNTs nanoscale size can be easily taken up by the human body via

skin penetration, ingestion, inhalation, and injections, which is aggravated by their low in-body biodegradability that may undesirably remain longer periods of time. Their pristine state has shown toxicity response due to their high aspect ratio, hydrophobicity, and aggregation propensity. Most CNTs-containing bioapplications rely on a multifunctional functionalization to succeed in the intended medical care improvement. The defects via covalent modification alter their unique properties. All these concerns impede their progress into clinical stage application.

1.4   Bibliography

1.   Iijima, S. Helical microtubules of graphitic carbon. *Nature* **1991**, *354* (6348), 56–58.

2.   Liu, M.; Ye, X.; Bai, Y.; Zhang, R.; Wei, F.; Li, X. Multi-scale analysis of the interaction in ultra-long carbon nanotubes and bundles. *Journal of the Mechanics and Physics of Solids* **2020**, *142*, 104032.

3.   Charoenpakdee, J.; Suntijitrungruang, O.; Boonchui, S. Chirality effects on an electron transport in single-walled carbon nanotube. *Scientific Reports* **2020**, *10* (1), 18949.

4.   Naqvi, S. T. R.; Rasheed, T.; Hussain, D.; Najam ul Haq, M.; Majeed, S.; Shafi, S.; Ahmed, N.; Nawaz, R. Modification strategies for improving the solubility/dispersion of carbon nanotubes. *Journal of Molecular Liquids* **2020**, *297*, 111919.

5.   Chio, L.; Pinals, R. L.; Murali, A.; Goh, N. S.; Landry, M. P. Covalent Surface Modification Effects on Single-Walled Carbon Nanotubes for Targeted Sensing and Optical Imaging. *Advanced Functional Materials* **2020**, *30* (17), 1910556.

6.   Yuan, X.; Wang, Y.; Zhu, B. Adhesion between two carbon nanotubes: Insights from molecular dynamics simulations and continuum mechanics. *International Journal of Mechanical Sciences* **2018**, *138*, 323–336.

7.   Jin, C.; Wu, Q.; Yang, G.; Zhang, H.; Zhong, Y. Investigation on hybrid nanofluids based on carbon nanotubes filled with metal nanoparticles: Stability, thermal conductivity, and viscosity. *Powder Technology* **2021**, *389*, 1–10.

8.   Rathinavel, S.; Priyadharshini, K.; Panda, D. A review on carbon nanotube: An overview of synthesis, properties, functionalization, characterization, and the application. *Materials Science and Engineering: B* **2021**, *268*, 115095.

9.   Abrisham, M.; Panahi-Sarmad, M.; Mir Mohamad Sadeghi, G.; Arjmand, M.; Dehghan, P.; Amirkiai, A. Microstructural design for enhanced mechanical property and shape memory behavior of polyurethane nanocomposites: Role of carbon nanotube, montmorillonite, and their hybrid fillers. *Polymer Testing* **2020**, *89*, 106642.

10.   Bamdad, H.; Hawboldt, K.; MacQuarrie, S. A review on common adsorbents for acid gases removal: Focus on biochar. *Renewable and Sustainable Energy Reviews* **2018**, *81*, 1705–1720.

11.   Tsai, K.-J.; Ni, C.-S.; Chen, H.-Y.; Huang, J.-H. Single-walled carbon nanotubes/Ni–Co–Mn layered double hydroxide nanohybrids as electrode materials for high-performance hybrid energy storage devices. *Journal of Power Sources* **2020**, *454*, 227912.

12.   Wang, H.; Li, S.; Wang, Y.; Wang, H.; Shen, X.; Zhang, M.; Lu, H.; He, M.; Zhang, Y. Bioinspired Fluffy Fabric with In Situ Grown Carbon Nanotubes for Ultrasensitive Wearable Airflow Sensor. *Advanced Materials* **2020**, *32* (11), 1908214.

13.   Zare, H.; Ahmadi, S.; Ghasemi, A.; Ghanbari, M.; Rabiee, N.; Bagherzadeh, M.; Karimi, M.; Webster, T. J.; Hamblin, M. R.; Mostafavi, E. Carbon Nanotubes: Smart Drug/Gene Delivery Carriers. *Int J Nanomedicine* **2021**, *16*, 1681–1706.

14.   Prajapati, S. K.; Malaiya, A.; Kesharwani, P.; Soni, D.; Jain, A. Biomedical applications and toxicities of carbon nanotubes. *Drug and Chemical Toxicology* **2020**, *45* (1), 1–16.

15.   Liu, Y.; Zhao, Y.; Sun, B.; Chen, C. Understanding the Toxicity of Carbon Nanotubes. *Accounts of Chemical Research* **2013**, *46* (3), 702–713.

16.   Zhang, M.; Xu, Y.; Yang, M.; Yudasaka, M.; Okazaki, T. Comparative assessments of the biodistribution and toxicity of oxidized single-walled carbon nanotubes dispersed with two different reagents after intravenous injection. *Nanotoxicology* **2021**, *15* (6), 798–811.

17.   Ye, L.; Chen, W.; Chen, Y.; Qiu, Y.; Yi, J.; Li, X.; Lin, Q.; Guo, B. Functionalized multiwalled carbon nanotube-ethosomes for transdermal delivery of ketoprofen: Ex vivo and in vivo evaluation. *Journal of Drug Delivery Science and Technology* **2022**, *69*, 103098.

18.   Ohta, T.; Hashida, Y.; Yamashita, F.; Hashida, M. Development of Novel Drug and Gene Delivery Carriers Composed of Single-Walled Carbon Nanotubes and Designed Peptides With PEGylation. *Journal of Pharmaceutical Sciences* **2016**, *105* (9), 2815–2824.

19.   Kofoed Andersen, C.; Khatri, S.; Hansen, J.; Slott, S.; Pavan Parvathaneni, R.; Mendes, A. C.; Chronakis, I. S.; Hung, S.-C.; Rajasekaran, N.; Ma, Z.; Zhu, S.; Dai, H.; Mellins, E. D.; Astakhova, K. Carbon Nanotubes-Potent Carriers for Targeted Drug Delivery in Rheumatoid Arthritis. *Pharmaceutics* **2021**, *13* (4), 453.

20.	Yu, P.; Zhang, X.; Cheng, G.; Guo, H.; Shi, X.; Zhang, X.; Zhou, J.; Wang, S.; Wu, Z.; Chang, J. Construction of a new multifunctional insomnia drug delivery system. *Chemical Engineering Journal* **2022**, *430*, 132633.

21.	Tan, J. M.; Bullo, S.; Fakurazi, S.; Hussein, M. Z. Characterization of Betulinic Acid-Multiwalled Carbon Nanotubes Modified with Hydrophilic Biopolymer for Improved Biocompatibility on NIH/3T3 Cell Line. *Polymers* **2021**, *13* (9), 1362.

22.	Khoshoei, A.; Ghasemy, E.; Poustchi, F.; Shahbazi, M.-A.; Maleki, R. Engineering the pH-Sensitivity of the Graphene and Carbon Nanotube Based Nanomedicines in Smart Cancer Therapy by Grafting Trimetyl Chitosan. *Pharmaceutical Research* **2020**, *37* (8), 160.

23.	Saeednia, L.; Yao, L.; Cluff, K.; Asmatulu, R. Sustained Releasing of Methotrexate from Injectable and Thermosensitive Chitosan-Carbon Nanotube Hybrid Hydrogels Effectively Controls Tumor Cell Growth. *ACS Omega* **2019**, *4* (2), 4040–4048.

24.	Wang, C.; Zhou, X.; Wang, G.; Wang, D.; Fang, C.; Ru, Y.; Hu, J.; Xie, L. Preparation of lysozyme/carbon nanotube hybrids and their interactions at the nano-bio interface. *Progress in Organic Coatings* **2022**, *163*, 106659.

25.	Chaudhary, H.; Fernandes, R. M. F.; Gowda, V.; Claessens, M. M. A. E.; Furó, I.; Lendel, C. Intrinsically disordered protein as carbon nanotube dispersant: How dynamic interactions lead to excellent colloidal stability. *Journal of Colloid and Interface Science* **2019**, *556*, 172–179.

26.	Feng, M.; Bell, D. R.; Zhou, R. Propensity of a single-walled carbon nanotube-peptide to mimic a KK10 peptide in an HLA-TCR complex. *The Journal of Chemical Physics* **2017**, *147* (22), 225101.

27.   Baweja, L.; Balamurugan, K.; Subramanian, V.; Dhawan, A. Effect of graphene oxide on the conformational transitions of amyloid beta peptide: A molecular dynamics simulation study. *Journal of Molecular Graphics and Modelling* **2015**, *61*, 175–185.

28.   Roxbury, D.; Zhang, S.-Q.; Mittal, J.; DeGrado, W. F.; Jagota, A. Structural Stability and Binding Strength of a Designed Peptide–Carbon Nanotube Hybrid. *The Journal of Physical Chemistry C* **2013**, *117* (49), 26255–26261.

29.   Balamurugan, K.; Gopalakrishnan, R.; Raman, S. S.; Subramanian, V. Exploring the Changes in the Structure of α-Helical Peptides Adsorbed onto a Single Walled Carbon Nanotube Using Classical Molecular Dynamics Simulation. *The Journal of Physical Chemistry B* **2010**, *114* (44), 14048–14058.

30.   Kuang, Z.; Kim, S. N.; Crookes-Goodson, W. J.; Farmer, B. L.; Naik, R. R. Biomimetic Chemosensor: Designing Peptide Recognition Elements for Surface Functionalization of Carbon Nanotube Field Effect Transistors. *ACS Nano* **2010**, *4* (1), 452–458.

31.   Dieckmann, G. R.; Dalton, A. B.; Johnson, P. A.; Razal, J.; Chen, J.; Giordano, G. M.; Muñoz, E.; Musselman, I. H.; Baughman, R. H.; Draper, R. K. Controlled Assembly of Carbon Nanotubes by Designed Amphiphilic Peptide Helices. *Journal of the American Chemical Society* **2003**, *125* (7), 1770–1777.

32.   Wolski, P.; Nieszporek, K.; Panczyk, T. Cytosine-Rich DNA Fragments Covalently Bound to Carbon Nanotube as Factors Triggering Doxorubicin Release at Acidic pH. A Molecular Dynamics Study. *Int J Mol Sci* **2021**, *22* (16), 8466.

33.   Wolski, P.; Nieszporek, K.; Panczyk, T. Carbon Nanotubes and Short Cytosine-Rich Telomeric DNA Oligomeres as Platforms for Controlled Release of Doxorubicin—A

Molecular Dynamics Study. *International Journal of Molecular Sciences* **2020**, *21* (10), 3619.

34.   Rabiee, N.; Bagherzadeh, M.; Ghadiri, A. M.; Fatahi, Y.; Aldhaher, A.; Makvandi, P.; Dinarvand, R.; Jouyandeh, M.; Saeb, M. R.; Mozafari, M.; Shokouhimehr, M.; Hamblin, M. R.; Varma, R. S. Turning Toxic Nanomaterials into a Safe and Bioactive Nanocarrier for Co-delivery of DOX/pCRISPR. *ACS Applied Bio Materials* **2021**, *4* (6), 5336–5351.

35.   Panczyk, T.; Wolski, P.; Lajtar, L. Coadsorption of Doxorubicin and Selected Dyes on Carbon Nanotubes. Theoretical Investigation of Potential Application as a pH-Controlled Drug Delivery System. *Langmuir* **2016**, *32* (19), 4719–4728.

36.   Meng, L.; Zhang, X.; Lu, Q.; Fei, Z.; Dyson, P. J. Single walled carbon nanotubes as drug delivery vehicles: Targeting doxorubicin to tumors. *Biomaterials* **2012**, *33* (6), 1689–1698.

37.   Maleki, R.; Afrouzi, H. H.; Hosseini, M.; Toghraie, D.; Piranfar, A.; Rostami, S. pH-sensitive loading/releasing of doxorubicin using single-walled carbon nanotube and multi-walled carbon nanotube: A molecular dynamics study. *Computer Methods and Programs in Biomedicine* **2020**, *186*, 105210.

38.   Ghoderao, P.; Sahare, S.; Alegaonkar, P.; Kulkarni, A. A.; Bhave, T. Multiwalled Carbon Nanotubes Decorated with Fe3O4 Nanoparticles for Efficacious Doxycycline Delivery. *ACS Applied Nano Materials* **2019**, *2* (1), 607–616.

39.   Chudoba, D.; Jażdżewska, M.; Łudzik, K.; Wołoszczuk, S.; Juszyńska-Gałązka, E.; Kościński, M. Description of Release Process of Doxorubicin from Modified Carbon Nanotubes. *International Journal of Molecular Sciences* **2021**, *22* (21), 12003.

40.   Arabian, T.; Amjad-Iranagh, S.; Halladj, R. Molecular dynamics simulation study of doxorubicin adsorption on functionalized carbon nanotubes with folic acid and tryptophan. *Scientific Reports* **2021**, *11* (1), 24210.

41.   Karimzadeh, S.; Safaei, B.; Jen, T.-C. Theorical investigation of adsorption mechanism of doxorubicin anticancer drug on the pristine and functionalized single-walled carbon nanotube surface as a drug delivery vehicle: A DFT study. *Journal of Molecular Liquids* **2021**, *322*, 114890.

42.   Mirsalari, H.; Maleki, A.; Raissi, H.; Soltanabadi, A. Investigation of the Pristine and Functionalized Carbon Nanotubes as a Delivery System for the Anticancer Drug Dacarbazine: Drug Encapsulation. *Journal of Pharmaceutical Sciences* **2021**, *110* (5), 2005–2016.

43.   de Almeida Barcelos, K.; Alisaraie, L. Microtubule-inspired functionalization of carbon nanotubes: a biomimetic carrier design. *Molecular Systems Design & Engineering* **2022**, *7* (4), 330–349.

44.   Khalid, A.; Madni, A.; Raza, B.; Islam, M. u.; Hassan, A.; Ahmad, F.; Ali, H.; Khan, T.; Wahid, F. Multiwalled carbon nanotubes functionalized bacterial cellulose as an efficient healing material for diabetic wounds. *International Journal of Biological Macromolecules* **2022**, *203*, 256–267.

45.   Ali, H. E.; Radwan, R. R. Synthesis, characterization and evaluation of resveratrol-loaded functionalized carbon nanotubes as a novel delivery system in radiation enteropathy. *European Journal of Pharmaceutical Sciences* **2021**, *167*, 106002.

46.	Assali, M.; Kittana, N.; Dayyeh, S.; Khiar, N. Dual covalent functionalization of single-walled carbon nanotubes for effective targeted cancer therapy. *Nanotechnology* **2021**, *32* (20), 205101.

47.	Díez-Pascual, A. M. Chemical Functionalization of Carbon Nanotubes with Polymers: A Brief Overview. *Macromol* **2021**, *1* (2), 64–83.

48.	Ebrahim-Habibi, M.-B.; Ghobeh, M.; Mahyari, F. A.; Rafii-Tabar, H.; Sasanpour, P. An investigation into non-covalent functionalization of a single-walled carbon nanotube and a graphene sheet with protein G:A combined experimental and molecular dynamics study. *Scientific Reports* **2019**, *9* (1), 1273.

49.	Ershadi, N.; Safaiee, R.; Golshan, M. M. Functionalized (4,0) or (8,0) SWCNT as novel carriers of the anticancer drug 5-FU; A first-principle investigation. *Applied Surface Science* **2021**, *536*, 147718.

50.	Li, Z.; de Barros, A. L. B.; Soares, D. C. F.; Moss, S. N.; Alisaraie, L. Functionalized single-walled carbon nanotubes: cellular uptake, biodistribution and applications in drug delivery. *International Journal of Pharmaceutics* **2017**, *524* (1), 41–54.

51.	Pennetta, C.; Floresta, G.; Graziano, A. C. E.; Cardile, V.; Rubino, L.; Galimberti, M.; Rescifina, A.; Barbera, V. Functionalization of Single and Multi-Walled Carbon Nanotubes with Polypropylene Glycol Decorated Pyrrole for the Development of Doxorubicin Nano-Conveyors for Cancer Drug Delivery. *Nanomaterials (Basel)* **2020**, *10* (6), 1073.

52.   Debnath, S. K.; Srivastava, R. Drug Delivery With Carbon-Based Nanomaterials as Versatile Nanocarriers: Progress and Prospects. *Frontiers in Nanotechnology* **2021**, *3*, 644564.

53.   Sanginario, A.; Miccoli, B.; Demarchi, D. Carbon Nanotubes as an Effective Opportunity for Cancer Diagnosis and Treatment. *Biosensors* **2017**, *7* (1), 9.

54.   Park, S.; Kim, T.; Jo, D.; Jung, J. S.; Jo, G.; Park, Y.; Kang, E. S.; Kim, Y. H.; Kim, J.; Kim, K.; Hyun, H. Bioengineered Short Carbon Nanotubes as Tumor-Targeted Carriers for Biomedical Imaging. *Macromolecular Research* **2019**, *27* (8), 833-838.

55.   Jacobsen, N. R.; Møller, P.; Clausen, P. A.; Saber, A. T.; Micheletti, C.; Jensen, K. A.; Wallin, H.; Vogel, U. Biodistribution of Carbon Nanotubes in Animal Models. *Basic Clin Pharmacol Toxicol* **2017**, *121 Suppl 3*, 30-43.

56.   Jain, S.; Thakare, V. S.; Das, M.; Godugu, C.; Jain, A. K.; Mathur, R.; Chuttani, K.; Mishra, A. K. Toxicity of Multiwalled Carbon Nanotubes with End Defects Critically Depends on Their Functionalization Density. *Chemical Research in Toxicology* **2011**, *24* (11), 2028-2039.

57.   Li, Z.; Tozer, T.; Alisaraie, L. Molecular Dynamics Studies for Optimization of Noncovalent Loading of Vinblastine on Single-Walled Carbon Nanotube. *The Journal of Physical Chemistry C* **2016**, *120* (7), 4061–4070.

58.   Kamazani, F. M.; Sotoodehnejad nematalahi, F.; Siadat, S. D.; Pornour, M.; Sheikhpour, M. A success targeted nano delivery to lung cancer cells with multi-walled carbon nanotubes conjugated to bromocriptine. *Scientific Reports* **2021**, *11* (1), 24419.

59.   Lyra, K. M.; Kaminari, A.; Panagiotaki, K. N.; Spyrou, K.; Papageorgiou, S.; Sakellis, E.; Katsaros, F. K.; Sideratou, Z. Multi-Walled Carbon Nanotubes Decorated

with Guanidinylated Dendritic Molecular Transporters: An Efficient Platform for the Selective Anticancer Activity of Doxorubicin. *Pharmaceutics* **2021**, *13* (6), 858.

60.   Abbaspour, M.; Namayandeh Jorabchi, M.; Akbarzadeh, H.; Salemi, S.; Ebrahimi, R. Molecular dynamics simulation of anticancer drug delivery from carbon nanotube using metal nanowires. *Journal of Computational Chemistry* **2019**, *40* (25), 2179–2190.

61.   Zhang, X.; An, D.; Zhang, R.; Huang, Y.; Liu, Z. Preparation of carbon nanotubes and polyhedral oligomeric-reinforced molecularly imprinted polymer composites for drug delivery of gallic acid. *International Journal of Pharmaceutics* **2022**, *615*, 121476.

62.   Burkert, S. C.; He, X.; Shurin, G. V.; Nefedova, Y.; Kagan, V. E.; Shurin, M. R.; Star, A. Nitrogen-Doped Carbon Nanotube Cups for Cancer Therapy. *ACS Applied Nano Materials* **2021**, *4*, n/a.

63.   Tohidifar, L.; Strodel, B. Molecular dynamics studies for enhancing the anticancer drug efficacy: Toward designing a new carbon nanotube-based paclitaxel delivery system. *Journal of Molecular Liquids* **2021**, *323*, 114638.

64.   Haghi, A.; Raissi, H.; Hashemzadeh, H.; Farzad, F. Development of the poly(l-histidine) grafted carbon nanotube as a possible smart drug delivery vehicle. *Computers in Biology and Medicine* **2022**, *143*, 105336.

65.   Madani, S. Z. M.; Safaee, M. M.; Gravely, M.; Silva, C.; Kennedy, S.; Bothun, G. D.; Roxbury, D. Carbon Nanotube–Liposome Complexes in Hydrogels for Controlled Drug Delivery via Near-Infrared Laser Stimulation. *ACS Applied Nano Materials* **2021**, *4* (1), 331–342.

66.   Bibi, A.; Sadiq ur, R.; Akhtar, T.; Akhtar, K.; Farooq, M.; Shahzad, M. I. Alginate-chitosan/MWCNTs nanocomposite: a novel approach for sustained release of Ibuprofen. *Journal of Polymer Research* **2020**, *27* (12), 363.

67.   Suo, N.; Wang, M.; Jin, Y.; Ding, J.; Gao, X.; Sun, X.; Zhang, H.; Cui, M.; Zheng, J.; Li, N.; Jin, X.; Jiang, S. Magnetic multiwalled carbon nanotubes with controlled release of epirubicin: an intravesical instillation system for bladder cancer. *Int J Nanomedicine* **2019**, *14*, 1241–1254.

68.   Gangrade, A.; Mandal, B. B. Injectable Carbon Nanotube Impregnated Silk Based Multifunctional Hydrogel for Localized Targeted and On-Demand Anticancer Drug Delivery. *ACS Biomaterials Science & Engineering* **2019**, *5* (5), 2365-2381.

69.   Ren, Z.; Luo, Y.; Meng, Z.; Zhang, J.; Yu, R.; Sun, M.; Xu, T.; Li, J.; Ma, Y.; Huang, Y.; Qin, T. Multi-walled carbon nanotube polysaccharide modified Hericium erinaceus polysaccharide as an adjuvant to extend immune responses. *Int J Biol Macromol* **2021**, *182*, 574–582.

70.   Zomorodbakhsh, S.; Abbasian, Y.; Naghinejad, M.; Sheikhpour, M. The Effects Study of Isoniazid Conjugated Multi-Wall Carbon Nanotubes Nanofluid on Mycobacterium tuberculosis. *Int J Nanomedicine* **2020**, *15*, 5901–5909.

71.   Jomhori, M.; Mosaddeghi, H.; Farzin, H. Tracking the interaction between single-wall carbon nanotube and SARS-Cov-2 spike glycoprotein: A molecular dynamics simulations study. *Computers in Biology and Medicine* **2021**, *136*, 104692.

72.   Shi, Y.; Peng, D.; Wang, D.; Zhao, Z.; Chen, B.; He, B.; Zhu, Y.; Wang, K.; Tian, J.; Zhang, Q. Biodistribution Survey of Oxidized Single-Wall Carbon Nanohorns

Following Different Administration Routes by Using Label-Free Multispectral Optoacoustic Tomography. *Int J Nanomedicine* **2019**, *14*, 9809–9821.

73.   Chen, H.; Zhao, R.; Wang, B.; Zheng, L.; Ouyang, H.; Wang, H.; Zhou, X.; Zhang, D.; Chai, Z.; Zhao, Y.; Feng, W. Acute Oral Administration of Single-Walled Carbon Nanotubes Increases Intestinal Permeability and Inflammatory Responses: Association with the Changes in Gut Microbiota in Mice. *Adv Healthc Mater* **2018**, *7* (13), e1701313.

74.   Chen, Z.; Zhuang, J.; Pang, J.; Liu, Z.; Zhang, P.; Deng, H.; Zhang, L.; Zhuang, B. Application of a cationic amylose derivative loaded with single-walled carbon nanotubes for gene delivery therapy and photothermal therapy of colorectal cancer. *J Biomed Mater Res A* **2022**, 1052–1061.

75.   Zhao, Y.; Zhao, T.; Cao, Y.; Sun, J.; Zhou, Q.; Chen, H.; Guo, S.; Wang, Y.; Zhen, Y.; Liang, X.-J.; Zhang, S. Temperature-Sensitive Lipid-Coated Carbon Nanotubes for Synergistic Photothermal Therapy and Gene Therapy. *ACS Nano* **2021**, *15* (4), 6517–6529.

76.   Li, D.; Ahmed, M.; Khan, A.; Xu, L.; Walters, A. A.; Ballesteros, B.; Al-Jamal, K. T. Tailoring the Architecture of Cationic Polymer Brush-Modified Carbon Nanotubes for Efficient siRNA Delivery in Cancer Immunotherapy. *ACS Applied Materials & Interfaces* **2021**, *13* (26), 30284–30294.

77.   Taghavi, S.; Shahriari, M.; Abnous, K.; Taghdisi, S. M.; Alibolandi, M.; Ramezani, M. Development of PNC-27 targeted codelivery system for survivin-shRNA and SN38 against colon adenocarcinoma in vitro and in vivo. *Journal of Drug Delivery Science and Technology* **2022**, *69*, 103180.

78.   Yin, W.; Qian, S.-M. CD44v6-O-MWNTS-Loaded Gemcitabine and CXCR4 siRNA Improves the Anti-tumor Effectiveness of Ovarian Cancer. *Frontiers in Cell and Developmental Biology* **2021**, *9*, 687322.

79.   Nagai, Y.; Nakamura, K.; Ohno, J.; Kawaguchi, M.; Fujigaya, T. Antibody-Conjugated Gel-Coated Single-Walled Carbon Nanotubes as Photothermal Agents. *ACS Applied Bio Materials* **2021**, *4* (6), 5049–5056.

80.   Su, Z.; Zhao, Y.; Huang, Y.; Lian, Y.; Xu, S.; Bai, G. Bi-functional nanocomposite based on phosphor and carbon nanotubes for tumor ablation in a photothermal fiber system with temperature feedback. *Chemical Engineering Journal* **2022**, *436*, 134994.

81.   Fan, Y. F.; Shang, W. T.; Lu, G. H.; Guo, K. X.; Deng, H.; Zhu, X. H.; Wang, C. C.; Tian, J. Decreasing hyaluronic acid combined with drug-loaded nanoprobes improve the delivery and efficacy of chemotherapeutic drugs for pancreatic cancer. *Cancer Lett* **2021**, *523*, 1–9.

82.   Leyva-González, C. A.; Salas-Treviño, D.; Contreras-Torres, F. F.; Loera-Arias, M. J.; Gómez-Tristán, C. A.; Piña-Mendoza, E. I.; García-Rivas, G. J.; Guillén-Meléndez, G. A.; Montes-de-Oca-Luna, R.; Saucedo-Cárdenas, O.; Soto-Domínguez, A. Hyaluronate Functionalized Multi-Wall Carbon Nanotubes Loaded with Carboplatin Enhance Cytotoxicity on Human Cancer Cell Lines. *Materials (Basel)* **2021**, *14* (13), 3622.

83.   Yang, S.; Yang, Y.; Yang, Y.; Zhao, X.; Wang, Q.; Li, B.; Dong, L.; Tian, R.; Bao, Z. Iron-Palladium Decorated Carbon Nanotubes Achieve Radiosensitization via Reactive Oxygen Species Burst. *Front Bioeng Biotechnol* **2021**, *9*, 683363–683363.

84.   Gajewska, A.; Wang, J. T. W.; Klippstein, R.; Martincic, M.; Pach, E.; Feldman, R.; Saccavini, J.-C.; Tobias, G.; Ballesteros, B.; Al-Jamal, K. T.; Da Ros, T. Functionalization of filled radioactive multi-walled carbon nanocapsules by arylation reaction for in vivo delivery of radio-therapy. *Journal of Materials Chemistry B* **2022**, *10* (1), 47–56.

85.   Qiang, N.; Wei, L.; Tao, Y.; Jin, W.; Bin, Y.; DingHua, Z. Construction of Durvalumab/carbon nanotube/PEI/aptamer-siRNA chimera for the immunotherapy of hepatocellular carcinoma. *Biomed Mater* **2022**, *17* (2), 25015.

86.   Khan, H. A.; Kishore, U.; Alsulami, H. M.; Alrokayan, S. H. Pro-Apoptotic and Immunotherapeutic Effects of Carbon Nanotubes Functionalized with Recombinant Human Surfactant Protein D on Leukemic Cells. *International journal of molecular sciences* **2021**, *22* (19), 10445.

87.   Das, M.; Nariya, P.; Joshi, A.; Vohra, A.; Devkar, R.; Seshadri, S.; Thakore, S. Carbon nanotube embedded cyclodextrin polymer derived injectable nanocarrier: A multiple faceted platform for stimulation of multi-drug resistance reversal. *Carbohydr Polym* **2020**, *247*, 116751.

88.   González-Domínguez, J. M.; Grasa, L.; Frontiñán-Rubio, J.; Abás, E.; Domínguez-Alfaro, A.; Mesonero, J. E.; Criado, A.; Ansón-Casaos, A. Intrinsic and selective activity of functionalized carbon nanotube/nanocellulose platforms against colon cancer cells. *Colloids and Surfaces B: Biointerfaces* **2022**, *212*, 112363.

89.   McKernan, P.; Virani, N. A.; Faria, G. N. F.; Karch, C. G.; Prada Silvy, R.; Resasco, D. E.; Thompson, L. F.; Harrison, R. G. Targeted Single-Walled Carbon

Nanotubes for Photothermal Therapy Combined with Immune Checkpoint Inhibition for the Treatment of Metastatic Breast Cancer. *Nanoscale Research Letters* **2021**, *16* (1), 9.

90.   Golubewa, L.; Timoshchenko, I.; Romanov, O.; Karpicz, R.; Kulahava, T.; Rutkauskas, D.; Shuba, M.; Dementjev, A.; Svirko, Y.; Kuzhir, P. Single-walled carbon nanotubes as a photo-thermo-acoustic cancer theranostic agent: theory and proof of the concept experiment. *Scientific Reports* **2020**, *10* (1), 22174.

91.   Wang, D.; Zhang, N.; Jing, X.; Zhang, Y.; Xu, Y.; Meng, L. A tumor-microenvironment fully responsive nano-platform for MRI-guided photodynamic and photothermal synergistic therapy. *Journal of Materials Chemistry B* **2020**, *8* (36), 8271–8281.

92.   Liu, X.; Liu, Y.; Wang, J.; Wei, T.; Dai, Z. Mild Hyperthermia-Enhanced Enzyme-Mediated Tumor Cell Chemodynamic Therapy. *ACS Applied Materials & Interfaces* **2019**, *11* (26), 23065–23071.

93.   Chall, A.; Stagg, J.; Mixson, A.; Gato, E.; Quirino, R. L.; Sittaramane, V. Ablation of cells in mice using antibody-functionalized multiwalled carbon nanotubes (Ab-MWCNTs) in combination with microwaves. *Nanotechnology* **2021**, *32* (19), 195102.

94.   Saber-Samandari, S.; Mohammadi-Aghdam, M.; Saber-Samandari, S. A novel magnetic bifunctional nanocomposite scaffold for photothermal therapy and tissue engineering. *International Journal of Biological Macromolecules* **2019**, *138*, 810–818.

95.   Bon, S. B.; Chiesa, I.; Degli Esposti, M.; Morselli, D.; Fabbri, P.; De Maria, C.; Morabito, A.; Coletta, R.; Calamai, M.; Pavone, F. S.; Tonin, R.; Morrone, A.; Giorgi, G.; Valentini, L. Carbon Nanotubes/Regenerated Silk Composite as a Three-Dimensional

Printable Bio-Adhesive Ink with Self-Powering Properties. *ACS Applied Materials & Interfaces* **2021**, *13* (18), 21007–21017.

96.   Kaur, K.; Paiva, S. S.; Caffrey, D.; Cavanagh, B. L.; Murphy, C. M. Injectable chitosan/collagen hydrogels nano-engineered with functionalized single wall carbon nanotubes for minimally invasive applications in bone. *Mater Sci Eng C Mater Biol Appl* **2021**, *128*, 112340.

97.   Lemos, R.; Maia, F. R.; Ribeiro, V. P.; Costa, J. B.; Coutinho, P. J. G.; Reis, R. L.; Oliveira, J. M. Carbon nanotube-reinforced cell-derived matrix-silk fibroin hierarchical scaffolds for bone tissue engineering applications. *Journal of Materials Chemistry B* **2021**, *9* (46), 9561–9574.

98.   Wang, S.-F.; Wu, Y.-C.; Cheng, Y.-C.; Hu, W.-W. The Development of Polylactic Acid/Multi-Wall Carbon Nanotubes/Polyethylene Glycol Scaffolds for Bone Tissue Regeneration Application. *Polymers* **2021**, *13* (11), 1740.

99.   Wei, C.; Jin, X.; Wu, C.; Zhang, W. Injectable composite hydrogel based on carbon particles for photothermal therapy of bone tumor and bone regeneration. *Journal of Materials Science & Technology* **2022**, *118*, 64–72.

100.   Machado-Paula, M. M.; Corat, M. A. F.; de Vasconcellos, L. M. R.; Araújo, J. C. R.; Mi, G.; Ghannadian, P.; Toniato, T. V.; Marciano, F. R.; Webster, T. J.; Lobo, A. O. Rotary Jet-Spun Polycaprolactone/Hydroxyapatite and Carbon Nanotube Scaffolds Seeded with Bone Marrow Mesenchymal Stem Cells Increase Bone Neoformation. *ACS Applied Bio Materials* **2022**, *5* (3), 1013–1024.

101.   Murugan, E.; Akshata, C. R.; Yogaraj, V.; Sudhandiran, G.; Babu, D. Synthesis, characterization and in vitro evaluation of dendrimer-MWCNT reinforced SrHAP

composite for bone tissue engineering. *Ceramics International* **2022**, *48* (11), 16000–16009.

102.   Zenoozi, S.; Sadeghi, G. M. M.; Shahrousvand, M.; Rafiee, M. Preparation and optimization of polyurethane/crosslinked poly acrylic acid semi-IPNs containing multi wall carbon nanotube applicable for artificial tendon. *Colloids and Surfaces A: Physicochemical and Engineering Aspects* **2022**, *640*, 128415.

103.   David, M. E.; Ion, R. M.; Grigorescu, R. M.; Iancu, L.; Holban, A. M.; Iordache, F.; Nicoara, A. I.; Alexandrescu, E.; Somoghi, R.; Teodorescu, S.; Gheboianu, A. I. Biocompatible and Antimicrobial Cellulose Acetate-Collagen Films Containing MWCNTs Decorated with TiO2 Nanoparticles for Potential Biomedical Applications. *Nanomaterials* **2022**, *12* (2), 239.

104.   Zhang, W.; Zhao, L.; Gao, C.; Huang, J.; Li, Q.; Zhang, Z. Highly resilient, biocompatible, and antibacterial carbon nanotube/hydroxybutyl chitosan sponge dressing for rapid and effective hemostasis. *Journal of Materials Chemistry B* **2021**, *9* (47), 9754–9763.

105.   Mehrotra, S.; Singh, R. D.; Bandyopadhyay, A.; Janani, G.; Dey, S.; Mandal, B. B. Engineering Microsphere-Loaded Non-mulberry Silk-Based 3D Bioprinted Vascularized Cardiac Patches with Oxygen-Releasing and Immunomodulatory Potential. *ACS Applied Materials & Interfaces* **2021**, *13* (43), 50744–50759.

106.   Bai, R.; Liu, J.; Zhang, J.; Shi, J.; Jin, Z.; Li, Y.; Ding, X.; Zhu, X.; Yuan, C.; Xiu, B.; Liu, H.; Yuan, Z.; Liu, Z. Conductive single-wall carbon nanotubes/extracellular matrix hybrid hydrogels promote the lineage-specific development of seeding cells for

tissue repair through reconstructing an integrin-dependent niche. *J Nanobiotechnology* **2021**, *19* (1), 252–252.

107. Yang, R.; Yang, S.; Li, K.; Luo, Z.; Xian, B.; Tang, J.; Ye, M.; Lu, S.; Zhang, H.; Ge, J. Carbon Nanotube Polymer Scaffolds as a Conductive Alternative for the Construction of Retinal Sheet Tissue. *ACS Chemical Neuroscience* **2021**, *12* (17), 3167–3175.

108. Zheng, N.; Fitzpatrick, V.; Cheng, R.; Shi, L.; Kaplan, D. L.; Yang, C. Photoacoustic Carbon Nanotubes Embedded Silk Scaffolds for Neural Stimulation and Regeneration. *ACS Nano* **2022**, *16* (2), 2292–2305.

109. Pi, W.; Zhang, Y.; Li, L.; Li, C.; Zhang, M.; Zhang, W.; Cai, Q.; Zhang, P. Polydopamine-coated polycaprolactone/carbon nanotubes fibrous scaffolds loaded with brain-derived neurotrophic factor for peripheral nerve regeneration. *Biofabrication* **2022**, *14* (3), 35006.

110. Liu, S.; Li, D.; Chen, X.; Jiang, L. Biomimetic cuttlebone polyvinyl alcohol/carbon nanotubes/hydroxyapatite aerogel scaffolds enhanced bone regeneration. *Colloids and Surfaces B: Biointerfaces* **2022**, *210*, 112221.

111. Huang, Y.; Jing, W.; Li, Y.; Cai, Q.; Yang, X. Composites made of polyorganophosphazene and carbon nanotube up-regulating osteogenic activity of BMSCs under electrical stimulation. *Colloids Surf B Biointerfaces* **2021**, *204*, 111785.

112. Oliveira, E. R.; Fayer, L.; Zanette, R. S. S.; Ladeira, L. O.; de Oliveira, L. F. C.; Maranduba, C. M. C.; Brandão, H. M.; Munk, M. Cytocompatibility of carboxylated multi-wall carbon nanotubes in stem cells from human exfoliated deciduous teeth. *Nanotechnology* **2021**, *33* (6), 65101.

113. Ma, S.; Zhang, Y.; Ren, Q.; Wang, X.; Zhu, J.; Yin, F.; Li, Z.; Zhang, M. Tetrahedral DNA nanostructure based biosensor for high-performance detection of circulating tumor DNA using all-carbon nanotube transistor. *Biosensors and Bioelectronics* **2022**, *197*, 113785.

114. Karimi-Maleh, H.; Khataee, A.; Karimi, F.; Baghayeri, M.; Fu, L.; Rouhi, J.; Karaman, C.; Karaman, O.; Boukherroub, R. A green and sensitive guanine-based DNA biosensor for idarubicin anticancer monitoring in biological samples: A simple and fast strategy for control of health quality in chemotherapy procedure confirmed by docking investigation. *Chemosphere* **2022**, *291*, 132928.

115. Miripour, Z. S.; Abbasvandi, F.; Aghaee, P.; NajafiKhoshnoo, S.; Faramarzpour, M.; Mohaghegh, P.; Hoseinpour, P.; Namdar, N.; Amiri, M. H.; Ghafari, H.; Zareie, S.; Shojaeian, F.; Sanati, H.; Mapar, M.; Sadeghian, N.; Akbari, M. E.; Khayamian, M. A.; Abdolahad, M. Electrochemical tracing of hypoxia glycolysis by carbon nanotube sensors, a new hallmark for intraoperative detection of suspicious margins to breast neoplasia. *Bioeng Transl Med* **2022**, *7* (1), e10236.

116. Eduarda Schneider, M.; Guillade, L.; Correa-Duarte, M. A.; Moreira, F. T. C. Development of a biosensor for phosphorylated Tau 181 protein detection in Early-Stage Alzheimer's disease. *Bioelectrochemistry* **2022**, *145*, 108057.

117. Liu, Z.; Bian, L.; Yeoman, C. J.; Clifton, G. D.; Ellington, J. E.; Ellington-Lawrence, R. D.; Borgogna, J.-L. C.; Star, A. Bacterial Vaginosis Monitoring with Carbon Nanotube Field-Effect Transistors. *Analytical Chemistry* **2022**, *94* (9), 3849–3857.

118. Pinals, R. L.; Ledesma, F.; Yang, D.; Navarro, N.; Jeong, S.; Pak, J. E.; Kuo, L.; Chuang, Y.-C.; Cheng, Y.-W.; Sun, H.-Y.; Landry, M. P. Rapid SARS-CoV-2 Spike

Protein Detection by Carbon Nanotube-Based Near-Infrared Nanosensors. *Nano Letters* **2021**, *21* (5), 2272–2280.

119.   Zamzami, M. A.; Rabbani, G.; Ahmad, A.; Basalah, A. A.; Al-Sabban, W. H.; Nate Ahn, S.; Choudhry, H. Carbon nanotube field-effect transistor (CNT-FET)-based biosensor for rapid detection of SARS-CoV-2 (COVID-19) surface spike protein S1. *Bioelectrochemistry* **2022**, *143*, 107982.

120.   Kim, S. Y.; Lee, J.-C.; Seo, G.; Woo, J. H.; Lee, M.; Nam, J.; Sim, J. Y.; Kim, H.-R.; Park, E. C.; Park, S. Computational Method-Based Optimization of Carbon Nanotube Thin-Film Immunosensor for Rapid Detection of SARS-CoV-2 Virus. *Small Science* **2022**, *2* (2), 2100111.

121.   Lee, D.; Bhardwaj, J.; Jang, J. Paper-based electrochemical immunosensor for label-free detection of multiple avian influenza virus antigens using flexible screen-printed carbon nanotube-polydimethylsiloxane electrodes. *Scientific Reports* **2022**, *12* (1), 2311.

122.   Bakh, N. A.; Gong, X.; Lee, M. A.; Jin, X.; Koman, V. B.; Park, M.; Nguyen, F. T.; Strano, M. S. Transcutaneous Measurement of Essential Vitamins Using Near-Infrared Fluorescent Single-Walled Carbon Nanotube Sensors. *Small* **2021**, *17* (31), e2100540.

123.   Sekar, P. K.; Liang, X. M.; Kahng, S.-J.; Shu, Z.; Dichiara, A. B.; Chung, J.-H.; Wu, Y.; Gao, D. Simultaneous multiparameter whole blood hemostasis assessment using a carbon nanotube-paper composite capacitance sensor. *Biosensors and Bioelectronics* **2022**, *197*, 113786.

124.   Gomes, R. S.; Gomez-Rodríguez, B. A.; Fernandes, R.; Sales, M. G. F.; Moreira, F. T. C.; Dutra, R. F. Plastic Antibody of Polypyrrole/Multiwall Carbon Nanotubes on Screen-Printed Electrodes for Cystatin C Detection. *Biosensors (Basel)* **2021**, *11* (6), 175.

125.   Wang, H.; Zhou, R.; Li, D.; Zhang, L.; Ren, G.; Wang, L.; Liu, J.; Wang, D.; Tang, Z.; Lu, G.; Sun, G.; Yu, H.-D.; Huang, W. High-Performance Foam-Shaped Strain Sensor Based on Carbon Nanotubes and Ti3C2Tx MXene for the Monitoring of Human Activities. *ACS Nano* **2021**, *15* (6), 9690–9700.

126.   Lim, G.-H.; Bae, S.; Kim, Y.-J.; Lee, K. S.; Cho, H.; Park, Y. J.; Lee, H.-S.; Kim, S.-H.; Kim, S.; Chung, H.-S.; Yun, Y. J.; Kim, K.; Kim, C.; Seo, J.-S.; Moon, H. G.; Son, D. I. Boron nitride/carbon nanotube composite paper for self-activated chemiresistive detection. *Sensors and Actuators B: Chemical* **2022**, *355*, 131273.

127.   Wang, Y.; Wang, Y.; Zhu, R.; Tao, Y.; Chen, Y.; Liu, Q.; Liu, X.; Wang, D. Woven fiber organic electrochemical transistors based on multiwalled carbon nanotube functionalized PEDOT nanowires for nondestructive detection of potassium ions. *Materials Science and Engineering: B* **2022**, *278*, 115657.

128.   Ben-Shimon, Y.; Ya'akobovitz, A. Flexible and bio-compatible temperature sensors based on carbon nanotube composites. *Measurement* **2021**, *172*, 108889.

129.   Gifani, M.; Eddins, D. J.; Kosuge, H.; Zhang, Y.; Paluri, S. L. A.; Larson, T.; Leeper, N.; Herzenberg, L. A.; Gambhir, S. S.; McConnell, M. V.; Ghosn, E. E. B.; Smith, B. R. Ultraselective Carbon Nanotubes for Photoacoustic Imaging of Inflamed Atherosclerotic Plaques. *Advanced Functional Materials* **2021**, *31* (37), 2101005.

130.   Hendler-Neumark, A.; Wulf, V.; Bisker, G. In vivo imaging of fluorescent single-walled carbon nanotubes within C. elegans nematodes in the near-infrared window. *Materials Today Bio* **2021**, *12*, 100175.

131.   Langenbacher, R.; Budhathoki-Uprety, J.; Jena, P. V.; Roxbury, D.; Streit, J.; Zheng, M.; Heller, D. A. Single-Chirality Near-Infrared Carbon Nanotube Sub-Cellular Imaging and FRET Probes. *Nano Letters* **2021**, *21* (15), 6441–6448.

132.   Bikiaris, N. D.; Koumentakou, I.; Lykidou, S.; Nikolaidis, N. Innovative Skin Product O/W Emulsions Containing Lignin, Multiwall Carbon Nanotubes and Graphene Oxide Nanoadditives with Enhanced Sun Protection Factor and UV Stability Properties. *Applied Nano* **2022**, *3* (1), 1–15.

133.   Zhang, D.; Liu, Z.; Wu, G.; Yang, Z.; Cui, Y.; Li, H.; Zhang, Y. Fluorinated Carbon Nanotube Superamphiphobic Coating for High-Efficiency and Long-Lasting Underwater Antibiofouling Surfaces. *ACS Applied Bio Materials* **2021**, *4* (8), 6351–6360.

134.   Zhao, W.; Jiang, L.; Wang, W.; Sang, J.; Sun, Q.; Dong, Q.; Li, L.; Lu, F.; Liu, F. Design of carboxylated single-walled carbon nanotubes as highly efficient inhibitors against Aβ40 fibrillation based on the HyBER mechanism. *Journal of Materials Chemistry B* **2021**, *9* (34), 6902–6914.

135.   Hu, F.; Li, Y.; Wang, Q.; Zhu, B.; Wu, S.; Wang, Y.; Zeng, W.; Yin, J.; Liu, C.; Bergmann, S. M.; Shi, C. Immersion immunization of koi (Cyprinus carpio) against cyprinid herpesvirus 3 (CyHV-3) with carbon nanotube-loaded DNA vaccine. *Aquaculture* **2021**, *539*, 736644.

136.   Morco, S. R.; Williams, D. L.; Jensen, B. D.; Bowden, A. E. Structural biofilm resistance of carbon-infiltrated carbon nanotube coatings. *Journal of Orthopaedic Research* **2021**, *n/a* (n/a), 1–8.

CHAPTER 2

Cytoskeletal-inspired Peptides on CNT for Drug Delivery[*]

2.1   Introduction

There have been emerging interests in exploring CNTs physicochemical, mechanical, thermal, structural, and optical properties[1] for their applications in multiple fields, including nanomedicine[2], drug, and gene delivery.[3-12] The pristine CNTs' chemical structures comprise carbon atoms with sp^2 hybridization, capable of interacting with other chemical entities through vdW forces. CNTs accumulate in cancer tissues due to their EPR properties, which besides their high aspect ratio and unique architecture, make them potential NPs for onsite cancer drug delivery systems.[13] Their hydrophobic property allows their bound hydrophobic cargos (*e.g.* drugs) to float in the bloodstream. CNTs high aspect ratio enables a high payload that consequently would help reduce the required drug dose for cancer treatments[14] by lowering the potential off-target drug interactions and the associated adverse

---

[*] This chapter was modified from "Microtubule-inspired functionalization of carbon nanotubes: a biomimetic carrier design" de Almeida Barcelos, K. & Alisaraie, L, *Molecular Systems Design & Engineering* **2022**, 7 (4).

effects in cancer patients.[15, 16] However, a significant obstacle for CNTs' bio-applicability is their low aqueous solubility.

Some chemical functionalization methods have been developed to address the probelm[17], including covalently attaching hydrophilic groups, usually carboxylic acid or amide chemical functional groups, *via* oxidation routes or using any existing defects in the CNT structure, or introducing artificial holes for chemical substitutions.[18] The particles produced from the oxidative degradation could be more easily expelled from the respiratory system than the unprocessed nanotubes.[19] Similarly, oxidation of multi-walled carbon nanotubes (MWNTs) using H_2SO_4 and HNO_3 results in O-MWNTs, which have been shown to not only improve CNTs biodegradation *in vitro* but also could act as an anticancer cytotoxic agent.[20] While surface oxidation of CNTs could increase their biodegradation *in vitro* and *in vivo*, assisting in the excretion of the NPs, it could also interrupt CNT's function as a drug delivery system when they immaturely release their side-chain bound cargos (*i.e.* drugs) before delivery to the site of action.[21] Despite the effectiveness of the covalent methods on CNTs hydrophilicity, they disrupt the intrinsic sp^2 hybridization of many carbon atoms and their associated network that are necessary for the CNT's exceptional properties[1] and thus diminish their utility for particular applications[17]. Alternatively, physical surface-adsorption has gained researchers' interest for maintaining the sp^2 hybridization in the chemical skeleton of carbon-based nanomaterials such as CNT[22, 23], graphene[22, 24], and fullerene.[22, 25] Amphiphilic peptides consisting of amino acids with various degrees of side-chain hydrophobicity and hydrophilicity are suitable molecules that due to their dual binding properties could bind to CNTs and water molecules.

The presented work proposes a bioinspired strategy for improving bioavailability and biocompatibility of single-walled CNTs using some of the functionally important amino acids sequence segments of the cytoskeletal biopolymer, MT, for CNTs non-covalent functionalization. MTs are composed of tubulin α–β heterodimer building blocks. MTs regulate multiple vital cellular functions and act as a platform for motor proteins (*e.g.*, dynein[26, 27], and kinesin[28]) movements for intracellular cargo transportations. The MTs' continual dynamic reconstruction is a natural process that permits unceasing transitions between heterodimers assembly (polymerization and elongation) and disassembly (depolymerization and shrinkage) at the MT ends[29]. The extension of MTs results from the heterodimers longitudinal (head-to-tail) assembly *via* non-covalent interactions of the α- and β-tubulin subunits that form long chains of protofilaments (pfs). The subunits of the pfs interact laterally in side-by-side arrangements, shaping a hollow cylinder along its longitudinal axis[30-35].

Due to the various and vital roles of the MTs in cell formation, cargo and organelle transportations, and cell motility, they have been one of the important targets for drug discovery and development of antimitotic, anticancer drugs.[36] The drugs act either as an MT polymerizer or depolymerizer, inhibiting its dynamic assembly–disassembly (i.e. polymerization–depolymerization) process, essential for maintaining the cell structure and survival. There are several binding sites on the α-, β-tubulin, located at the lateral or longitudinal interface of the two tubulin monomers that could accommodate several antimitotics, such as PTX[37], docetaxel[38], taccalonolide[39], epothilones (types A, B, D, and ixabepilone)[40, 41], cyclostreptin[42], dictyostatin[43], discodermolide[44], zampanolide[45], laulimalide[46, 47], peloruside A[46, 47], VLB[48-50], dolastatin[51], phomopsin A[52], and eribulin[53].

Earlier *in vivo* studies have emphasized that MWNTs mimic some of the MT's properties in HeLa cells. It reduces MT's dynamic, affecting the protein's polymerization–depolymerization process and its performance during cell division.[54] Due to the high similarity of CNTs and MTs[55] and their potential for use as drug delivery system[56], this work aims to take a step towards biomimicry of the MT using CNT to project some of the MT's drug-binding properties for improving CNTs drug delivery properties. In this approach, the MT segments from tubulin α–β heterodimer were selected as the amphiphilic peptides capable of non-covalently binding to the CNT surface. The peptides participate in the functionally critical lateral and longitudinal interactions among tubulin subunits, the MT protofilaments formation, and its dynamic "treadmilling" processes[37]. The peptides also contribute to the construction of the MTs drug binding sites.

The proposed microtubule-inspired CNT functionalization in this study is expected to enhance its solubility and drug delivery potential. The chemical specificity and amphiphilic diversity of the selected MT-based peptides can weaken CNTs' biotoxicity and amplify their cellular uptake.[57] *In silico* methods were utilized for this investigation to acquire information on the molecular and atomic interactions between the peptides bound to the CNT surface and each of the seventeen aforementioned antimitotic MT-targeting drugs. This work examined the potential of the proposed biomimicry strategy for improving CNTs application as biocompatible nanocarriers.

2.2   Materials and Method

There are five main lateral-associated segments on each α- and β-subunit of tubulin in the crystal structure of the α–β heterodimer.[37] They are located at: (*i*) H1–B2 loop (α: Tyr24–

Pro63, β: Ile24–Ala65); (*ii*) H2–B3 loop (α: Arg79–Pro89, β: Gly81–Asn91); (*iii*) H4–T5 loop (α: Leu157–Tyr161, β: Glu159–Asp163); (*iv*) M-loop (α: Tyr272–Val288, β: Pro274–Glu290); and (*v*) H10 helix (α: Asp327–Ile341, β: Asp329–Phe343). The H10 helix is the only MT fragment that participates in the α- and β-subunits' both lateral and longitudinal interactions. The amino acids indices and the protein segments' secondary structure (SS) assignments are according to the crystal structure of α–β-tubulin heterodimer of *Bos Tauros* (Uniprot code, P81947 (α-tubulin) and Q6B856 (β-tubulin)), deposited on the Protein Data Bank[58] (PDB) under 1JFF.pdb[37] retrieving code. Here, 1JFF.pdb[37] (*Bos taurus*) was studied instead of *Homo sapiens* tubulin subunits due to the availability of the experimentally-solved structure of the former. The sequence similarities between pair of equivalent peptides of α- and β-tubulin (i.e. the P1–P6; the P2–P7; the P3–P8; the P4–P9; and the P5–P10) were calculated using the Lalign server[59, 60] (**Table 2.1** and **Figure 2.1**).

The most critical lateral interactions among the MT protofilaments are directed by conformational changes of the tubulin fragments that consist of the M-loop (the P4 and P9) and the H1–B2 loop (the P1 and P6).[37, 61] The highly flexible loops undergo a wide range of changes at their dihedral angles leading the MT lattice to shape MTs with different diameters by the association of 12–16 interacting protofilaments.[30, 33] The M-loop plays a critical role in the pfs formation and accommodating anticancer drugs.[33, 37, 61-63] (**Table 2.1**)

Table 2.1 The studied MT segments (*i.e.*, the P1–P10 peptides) with their assigned SS on the tubulin heterodimer crystal structure (1JFF[37]) and location in an MT protofilament. The amino acids are shown as single-letter codes. The letters "T", "B", and "H" refer to the loops, β-strand, and α-helix folding, respectively.

Peptide	Segment in MT	Functional association in MT (inter-subunits)	Residue range (1JFF.pdb[37])	Amino acid (length AA) sequence and index
P1	α-H1–B2	Lateral	Tyr24–Pro63	Y_{24}CLEHGIQPDGQMPSDKTIGGGDDSFNTFFSETGAGKHVP$_{63}$ (40 AA)
P2	α-H2–B3	Lateral	Arg79–Pro89	R_{79}TGTYRQLFHP$_{89}$ (11 AA)
P3	α-H4–T5	Lateral	Leu157–Tyr161	L_{157}SVDY$_{161}$ (5 AA)
P4	α-M-loop	Lateral	Tyr272–Val288	Y_{272}APVISAEKAYHEQLSV$_{288}$ (17 AA)
P5	α-H10	Lateral and longitudinal	Asp327–Ile341	D_{327}VNAAIATIKTKRSI$_{341}$ (15 AA)
P6	β-H1–B2	Lateral	Ile24–Ala65	I_{24}SDEHGIDPTGSYHGDSDLQLERINVYYNEAAGNKYVPRA$_{65}$ (40 AA)
P7	β-H2–B3	Lateral	Gly81–Asn91	G_{81}PFGQIFRPDN$_{91}$ (11 AA)
P8	β-H4–T5	Lateral	Glu159–Asp163	E_{159}EYPD$_{163}$ (5 AA)
P9	β-M-loop	Lateral	Pro274–Glu290	P_{274}LTSRGSQQYRALTVPE$_{290}$ (17 AA)
P10	β-H10	Lateral and longitudinal	Asp329–Phe343	D_{329}EQMLNVQNKNSSYF$_{343}$ (15 AA)

Figure 2.1 (A) The schematic of an MT composed of (B) the tubulin heterodimers with α-subunit (light grey), β-subunit (dark grey) (1JFF.pdb[37]), and the studied tubulin-segments as loaded peptides on the CNT, (C) the C2 system is consisting of the peptides from β-tubulin segments and (D) the C1 system with the peptides from α-tubulin.

2.2.1   *In Silico* Preparation of the Peptides

The missing (*i.e.* unsolved) amino acids from the crystal structure of α–β tubulin heterodimer 1JFF.pdb[37] were identified according to the tubulin's amino acid sequence information. They were modeled and inserted in the heterodimer structure[34]. The protein fragments were next extracted and named the peptides P1–P5 (from α-tubulin) and P6–P10 (from β-tubulin). (**Table 2.1**)

2.2.1.1 *In silico* preparation of the C1 and C2 structures.

CNTs are specified by their diameter and chiral angle, determined with (***n, m***) vector pair notation. The initial three-dimensional structure of the single-walled CNT was modeled using Nanotube Modeler (version 1.8.0, JCrystalSof)[64] in a zigzag index of (16,0) with 12.4 Å in diameter and 40.0 Å in length, comparable to our previous experiments.[65] The zigzag CNT (16,0) also has sufficient surface area for loading all the selected peptides, the P1–P10, onto the CNT's outer wall. (**Table 2.2**)

Table 2.2 Description of the CNT–peptides complexes systems.

Peptides–CNT complex system (no. of atoms)	System descriptions	Peptides	Chirality	No of CNT
C1 (50775)	P1–P5 and CNT (16,0)	n = 5 from α-tubulin (the P1 to P5)	Zigzag (16,0)	n = 1
C2 (50824)	P6–P10 and CNT (16,0)	n = 5 from β-tubulin (the P6 to P10)	Zigzag (16,0)	n = 1

The P1–P5 (in the C1 system) and the P6–P10 (in the C2 system) were positioned randomly over the length of the CNT surface at a distance > ~3 Å. Next, the initial structures of the C1 and C2 were subject to MD simulations as follows:

2.2.2   Parametrization and Set-up for the MD Simulations

The MD simulations were carried out using the Gromacs package v.2016.5[66, 67]. The OPLS-AA force field[68] was employed for the calculation of bonding and non-bonding interactions.[65] The CNT non-bonded and charging parameters were according to the configurations described by Li et al.,[65] whereas the peptides' topology parameters were obtained from the Gromacs topology library for amino acids. (**Table 2.3**)

Table 2.3 Non-bonded parameters for the MD simulation of uncharged CNT according to the OPLS-AA force field. The k^b, k^θ, and k_φ are the force constants of stretching, bending, and torsional potentials, respectively; b_0 and θ_0 are reference geometry parameters; ε is the energy well-depth, and σ is the separation distance at which the interparticle potential is zero. Partial charges for carbon and hydrogen atoms were set 0.0, as for the uncharged particles.[65]

Function	Parameters		OPLS-AA notation
Atom	$\underline{C}$: $\varepsilon_c = 0.29288$ kJ mol^{-1}	$\sigma = 3.55$ Å	opls_147
types	$\underline{H}$: $\varepsilon_H = 0.12552$ kJ mol^{-1}	$\sigma = 2.42$ Å	opls_146
Bond	$\underline{C\text{-}C}$: $k^b = 392.4592$ kJ mol^{-1} Å	$b_0 = 1.40$ Å	TRP, TYR, PHE
types	$\underline{C\text{-}H}$: $k^b = 307.1056$ kJ mol^{-1} Å	$b_0 = 1.08$ Å	PHE, etc.
Angle	$\underline{C\text{-}C\text{-}C}$: $k^\theta = 527.184$ kJ mol^{-1} rad^{-2}	$\theta_0 = 120°$	PHE (OL)
types	$\underline{C\text{-}C\text{-}H}$: $k^\theta = 292.880$ kJ mol^{-1} rad^{-2}	$\theta_0 = 120°$	
	$\underline{H\text{-}C\text{-}H}$: $k^\theta = 292.880$ kJ mol^{-1} rad^{-2}	$\theta_0 = 117°$	wlj from HC-CM-HC
Dihedral	$\underline{C\text{-}C\text{-}C\text{-}C, H\text{-}C\text{-}C\text{-}H, H\text{-}C\text{-}C\text{-}C}$:		Aromatic rings
types	$k_\varphi = 30.334$ kJ mol^{-1}		

Besides the C1 and C2 systems, a separate MD simulation was performed (as a control system) for a single pristine CNT (16,0), in the absence of the peptides in a cubic water box with the same dimensions as in the C1 and C2 simulations (XYZ dimensions: $8.0 \times 8.0 \times 8.0$ nm^3). In addition, ten other independent MD simulations were carried out in the absence of the CNT for each of the ten peptides (*i.e.*, a free, unbounded peptide in a water box), which were also considered control systems. The latter is labeled with a single-prime symbol (') as in the P1' to P10' to distinguish each CNT-bound from the free peptide. **(Table A1)**

The simple point charge (SPC) water model was used for modeling the solvent (water) box. Depending on the resulting net charge of each system, Na^+ or Cl^- were added as counter ions to attain a 0.0 net charge under the physiological pH. (**Table A2**)

Periodic boundary conditions (PBC) were applied in three dimensions to minimize the edge effects by replicating adjacent boxes in all directions. Gromacs used the minimum image convention to ensure that only one image of an atom is examined for a short-range pair interaction during the calculations under the PBC. The non-bonded vdW and electrostatic interactions were modeled according to the forcefield parameters and 1.4 nm cut-off distance for both interaction types. The electrostatic forces and energy calculations were based on the Particle Mesh Ewald (PME) algorithm[69] to obtain accurate long-range interactions. Energy minimization (EM) was performed on the C1, C2 systems, the free peptides, and the pristine CNT using the steepest descent (SD)[70] algorithm with a maximum force tolerance ranging from 100.0–1000.0 kJ mol^{-1} nm^{-1}. (**Table A3**)

The energy minimization was followed by the position restraint (PR) using the "md" integrator for implementing Newton's equation of motion for 4.0 ns duration with 2.0×10^{-3} ps time-step. The Linear Constraint Solver (LINCS)[71] algorithm was applied to constrain all bond lengths, including those involved in hydrogen bonding. The temperature was set to 300.0 K with 0.1 ps temperature-coupling. The "md" integrator was also used in the following 10.0 ns equilibration phase. The compressibility was set to 4.5×10^{-5} bar implementing the Berendsen pressure-coupling scheme. The same parameters associated with the peptides or the CNT in the complex mode were applied to simulate the individual free peptides (*i.e.*, the P1'–P10') or the unbound CNT (16,0). However, due to the systems' smaller size, compared to the C1 and C2, the duration of the PR and equilibration

steps were set to 2.0 ns and 4.0 ns, respectively. The conformation, obtained at the 10.0 ns time frame of the equilibration phase, was used as the starting conformation for the 1.500 μs MD data collection. The root mean square deviation (RMSD) of the complexes were calculated according to Maiorov et al.,[72] for convergence assessment and estimating each conformation's deviation from its corresponding reference structure throughout the MD trajectory.[73] According to the RMSD data, the C1 and C2 systems were converged at ~0.800 μs. The simulations were continued for extra 0.700 μs after the convergence to allow sufficient time for the peptides or the complexes to explore a broader range of conformational space. Thus, the data from 0.800–1.500 μs of the simulations were analyzed. All calculations were run on Graham, the High-Performance Computing Cluster of Compute Canada. (**Equation 2.1** and **Figure A1A–B**)

$$RMSD\ (t_1, t_2) = \sqrt{\frac{1}{M} \sum_{i=1}^{N} m_i \|r_i(t_1) - r_i(t_2)\|^2}$$

Equation 2.1

$M = \sum_{i=1}^{N} m_i$ and r_i *(t)* are the position of atom *i* at *t* time.

2.2.3   Drugs' Structure and Binding to Peptides

A ligand library was constructed utilizing SYBYL-X 2.1.1 software package (Certara Corporation©). The library consisted of seventeen (17) anticancer MT-targeting drugs: PTX[37], docetaxel[38], taccalonolide[39], epothilones (types A, B, D, and ixabepilone)[40, 41], cyclostreptin[42], dictyostatin[43], discodermolide[44], zampanolide[45], laulimalide, peloruside A[46], vinblastine[48, 49], dolastatin[51], phomopsin A[52], and eribulin[53]. The structure of each drug was

energy minimized using the steepest descent algorithm and the Tripos force field with an energy gradient ranging from 0.0005 kJ mol^{-1} to 1 kJ mol^{-1} for up to 10,000,000 iterations. For the docking of the ligands on the peptides, the representative conformations of the MD trajectories of the C1 and C2 systems were obtained through the RMSD-based linkage clustering method.[66] The average structure of the most-populated conformation cluster was selected from the 0.800–1.500 µs time interval of each trajectory. For clustering, the conformation with the lowest gyration radius (R_g Å) was selected as the reference. FlexX[74-76] docking software, embedded in v.2.1.8 of the LeadIT software package (BioSolveIT©), was used for the calculation and binding-energy-based ($\Delta G_{binding}$) ranking of the docking solutions of the drug–peptides conformations. The FlexX search algorithm is founded on a base-fragment and incremental construction. The interaction energies are calculated according to the Böhm scoring function[77]. Prior to the docking calculations, all the peptides' amino acids were defined as potential target for the drugs binding, allowing the algorithm to distinguish the best sites of interactions. The binding profiles of the drugs in the highest rank (*i.e.* the lowest $\Delta G_{binding}$) were inspected for their potential as cargo for loading on the CNT as a carrier.

2.3   Results and Discussion

The tubulin lateral-associated peptides (*i.e.*, the P1–P10) include amino acids with hydrophobic moieties that interact with the hydrophobic CNT surface through vdW forces. In contrast, their hydrophilic moieties make polar interactions with the solvent molecules or the adjacent peptides. The distance of 2.5–6.0 Å between an atom of the CNT and a peptide's was a criterion for considering an inter-atomic interaction for calculating its Lenard-Jones

(LJ) potential interaction energy.[78] The peptides' binding affinities to the CNT were affected by increasing their interaction frequency and the CNT–peptides solvent accessible surface (SAS) that was calculated according to Eisenhaber et al.,[79] implemented in the Gromacs package.[66, 67, 80, 81] (**Equation 2.1**)

$$SAS\ area_{peptide_n-CNT} \ = \ \frac{1}{2} \left\{ (SAS_{peptide_n}) + (SAS_{CNT}) - (SAS_{complex}) \right\} \quad \textbf{Equation 2.1}$$

"n" represents a peptide index.

2.3.1 Analyses of the P1 to P10 Binding on the CNT

The analyses of the MD trajectories of the C1 and C2 systems showed that most of the peptides were bound to the CNT without any detachment from the tube surface; however, the P9 showed partial unbound conformations during 0.800–1.500 μs of the simulation. (**Figure 2.1C–D**)

A more detailed analysis of the observations, starting with the best binding peptides, was elucidated as follows:

2.3.1.1 The P4 and the P9

The P4 (α-M-loop) from tubulin α-subunit possesses seventeen residues (Y_{272}APVISAEKAYHEQLSV$_{288}$), coded as 272–288 (1JFF.pdb[37]). It is equivalent to the P9 (β-M-loop) from β-tubulin, also with seventeen residues (P_{274}LTSRGSQQYRALTVPE$_{290}$), numbered as 274–290 in the α–β tubulin heterodimer structure in 1JFF[37]. The similarity between their sequences is 60.0% (identity of 26.7%). The P4 and P9 were simple loops in the tubulin heterodimer structure and mainly folded as coil and bend configurations when

bound to the CNT during the MD simulation. The P4 showed a more effective binding pattern than the P9 presenting the lowest average distance to the CNT (0.30 nm), accounting for the most potent vdW interactions to the CNT, among the tubulin lateral segments (*i.e.,* the P1–P10). The Leu286–Glu290 of the P9 moved away from the CNT (average distance >0.57 nm) in favor of hydrogen bonding with the P6 hydrophilic amino acids and water molecules. However, its Pro274–Ala285 segment remained firmly bound to the CNT at a distance <~0.30 nm such that it made the P9 the second strongest CNT-binder among the P1–P10. (**Figure 2.2**, **Table A4** and **Table 2.4**)

Table 2.4 The average LJ energy (*i.e.* vdW), SAS area, interaction frequency number (at a distance ≤ 6 Å) between each peptide (*i.e.,* the P1–P10) and the CNT over the simulation time ordered by the strongest binding to the CNT.

Peptide on the CNT	LJ energy (kJ mog)	SAS area (nm²)	Interaction number
P4 (α-M-loop)	−425.43 ± 16.21	6.05 ± 0.28	3,635 ± 139
P9 (β-M-loop)	−375.84 ± 27.29	5.90 ± 0.43	3,373 ± 228
P6 (β-H1–B2)	−314.47 ± 12.18	5.56 ± 0.27	2,823 ± 113
P2 (α-H2–B3)	−245.41 ± 8.92	4.27 ± 0.18	2,304 ± 83
P7 (β-H2–B3)	−238.11 ± 10.47	4.13 ± 0.22	2,046 ± 96
P10 (β-H10)	−239.22 ± 20.56	4.40 ± 0.37	2,076 ± 180
P1 (α-H1–B2)	−219.69 ± 28.50	3.64 ± 0.32	1,840 ± 206
P5 (α-H10)	−172.03 ± 10.03	3.38 ± 0.19	1,783 ± 88
P8 (β-H4–T5)	−104.40 ± 12.33	1.97 ± 0.21	865 ± 101
P3 (α-H4–T5)	−101.51 ± 16.58	2.08 ± 0.25	975 ± 147
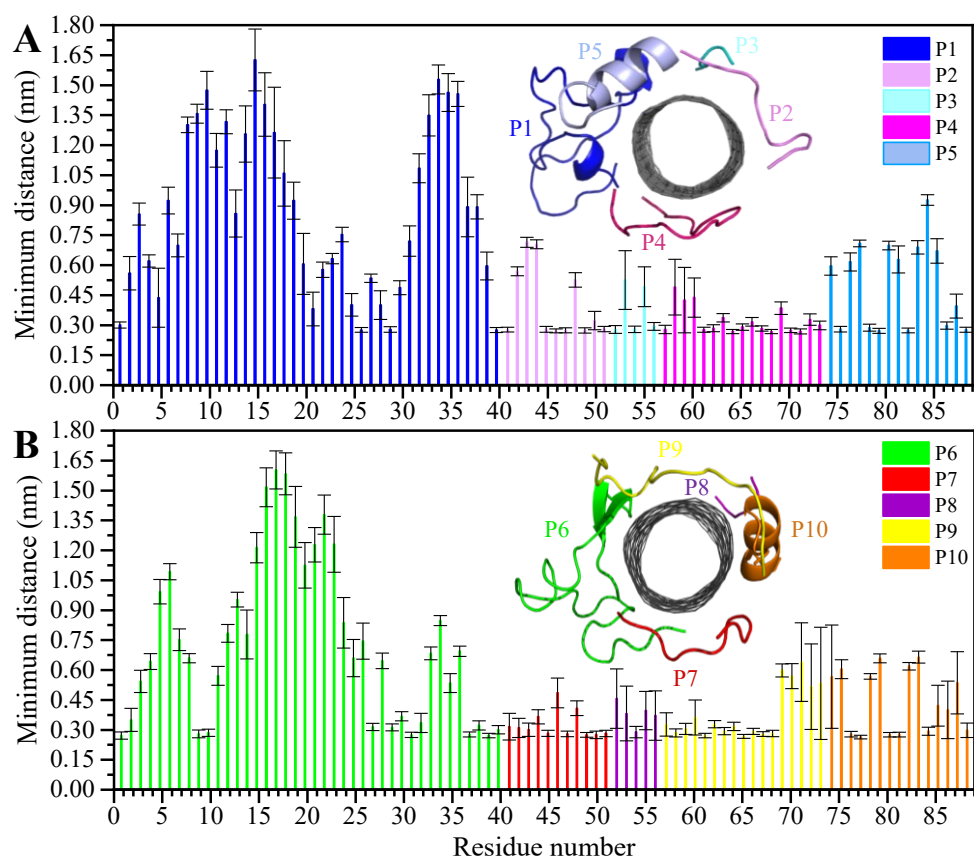
Figure 2.2 Residue-based binding analysis of the minimum distance between the centers-of-mass (COM) of the CNT and each of the: (A) P1 to P5 (the C1 system), and the (B) P6 to P10 (the C2 system).

The P4 conformations in the bound state had the most effective binding affinity due to the peptide's well-distributed side chains on the CNT, adapting satisfactorily to the tube's curvature that favored maximum vdW interactions. The P4 binding affinity was reinforced by a combination of vdW and polar interactions through the nearest amino acids, possessing aromatic, cyclic, positively charged, and aliphatic moieties (Tyr282, Tyr272, Gln285, Ile276, Lys280, His283, Pro274, Ala281, and Val275). The most extreme fluctuation of the P4 was during 1.160–1.190 µs, caused by its Tyr272 movements. It rotated from its

perpendicular to parallel position to the CNT as it was stimulated by a water molecule that bridged a hydrogen bond with the tyrosine hydroxyl moiety and an oxygen atom of Glu284. That caused a steric hindrance, triggering Pro274 desorption from the CNT, and consequently weakened the LJ potential energy of the P4–CNT by ~27 kJ mol^{-1}. That occurred along with the increase of the distance of their centers of mass (DCOM) for ~1 Å. Tyr272 at the N-terminal caused significant instability and weakened the vdW interactions of the P4 with the tube during 45% of the simulation time. Despite that, the P4 was identified as the best CNT-binder among the P1–P10. The observations suggest that Tyr272 could be replaced with Phe to eliminate Tyr hydroxyl moiety and its H-bonding property. (**Figure 2.3**)

The closely interacting P9 residues with the CNT were either positively charged or consisted of an aromatic moiety (Arg278, Arg284, Tyr283). Despite its Leu286, Val288, and Pro289 being intrinsically hydrophobic, their associated segment in the P9 (Leu286–Glu290) was hindered from firmly binding to the tube due to the more dominant effect of the hydrophilic fragments and their hydrogen bonding with water molecules, or the electrostatic interaction of Glu290 with Arg48 of its neighboring peptide, the P6. They, together, caused desorption of the P9 segment from the CNT during 0.864–0.871 μs and 1.027–1.073 μs time intervals. However, the overall P9's LJ energy improved over time due to the more frequent conformational changes of the Leu286–Glu290 segment favoring the CNT binding. The P9 instability and its nearly half-sequence desorption can be abolished using a CNT with a greater diameter or length than the CNT (16,0), capable of accommodating a broader range of the P9 conformations. In addition, replacing the P9's

Glu290 with a hydrophobic residue can eliminate its electrostatic interactions with the P6 and the P1 and improve its binding to the CNT. (**Figure 2.4B–C** and **Figure A2**)
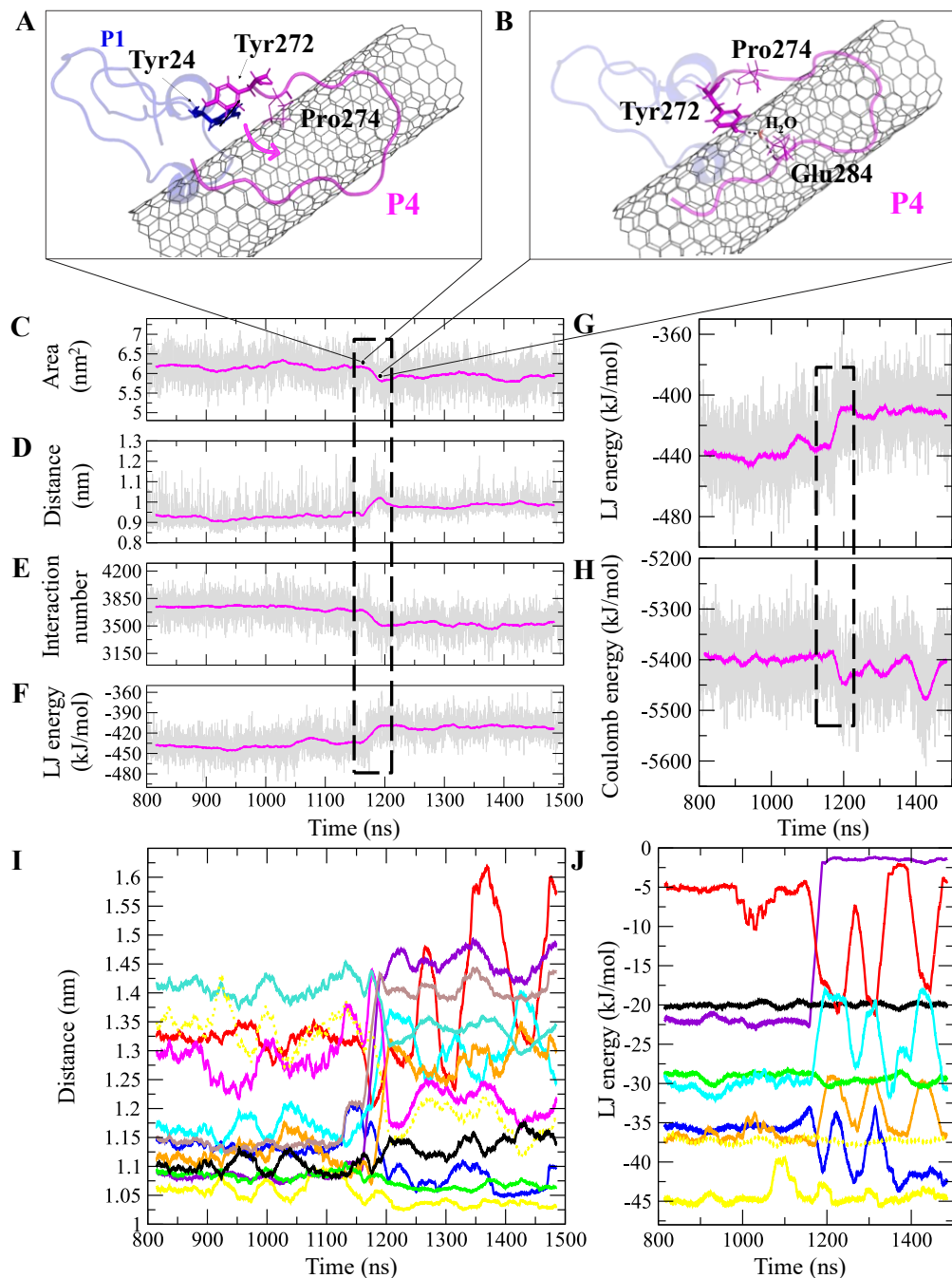

Figure 2.3 The P1 and P4 peptides, (A) and (B) The movement of Tyr272 ring of the P4 from vdW interacting with the Tyr24 of the P1 to hydrogen bond a mediating-water molecule

that bridges Glu284 of the P4, adapting its aromatic ring from perpendicular to parallel orientation with reference to the CNT longitudinal axis in the C1 system. The time evolution of properties between the CNT and the P4 (α-M-loop): (C) SAS area, (D) DCOM, (E) interaction frequency (< 6.0 Å), and (F) LJ energy. The P4 intramolecular (G) LJ energy and (H) coulomb energy. (I) The DCOM average between the CNT and the P4 residues Tyr272 (blue), Ala273 (brown), Pro274 (violet), Val275 (red), Ile276 (orange), Lys280 (cyan), Ala281 (black), Tyr282 (yellow), His283 (green), Glu284 (turquoise), Gln285 (dotted yellow), and Leu286 (magenta). (J) The LJ energy average of the CNT with: Tyr282 (yellow), Tyr272 (blue), Gln285 (dotted yellow), Ile276 (orange), His283 (green), Ala281 (black), Pro274 (violet), Val275 (red), and Lys280 (cyan). Graphs were generated with averaging every 300 frames of the 1.5 μs MD trajectory.

The P9 and P10 had the shortest CNT-binding lifetime, ~10% and ~17% of the simulation time after the convergence (*i.e.* 0.800 μs). The broadest LJ potential energy distribution curves as in the P4 (~−360–−480 kJ mol^{-1}) or the P9 (~−300–−500 kJ mol^{-1}) indicated a highly stable hydrophobic binding to the CNT. In contrast, the P2 had ~27%, the P7 ~33%, and P5 ~32% dwell time on the tube interacting to the CNT more frequently than the other peptides (*i.e.*, the P4 ~19%; the P9 ~10%). The long-lasting binders (the P2, P5, and P7) remained at the tube's central region involving their adjacent peptides, which limited their conformational freedom. (**Figure 2.4A**)

Studying CNTs using biomolecular force fields such as OPLS-AA, which uses pairwise interactions, might underestimate the degree of CNT's stiffness and exaggerate its flexibility,

causing unrealistic deformations as seen in some of the time frames of the simulation trajectories. (**Figure 2.2**)
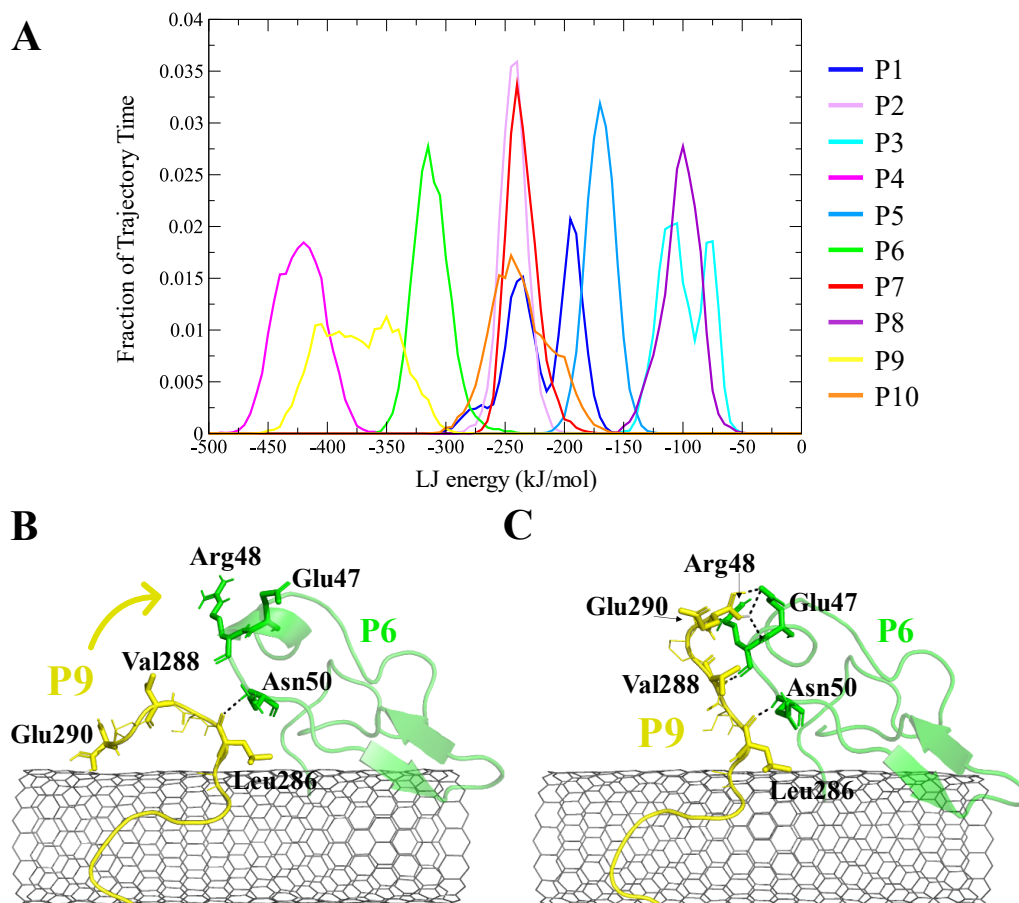
Figure 2.4 (A) The fraction of the simulation time (after convergence at ~0.800 μs) that each peptide was bound to the CNT versus their LJ potential energy (vdW interaction). The representative conformations of the P9 (Leu286–Glu290) fragment (B) binding to the CNT, (C) distancing from the CNT to H-bond to the P6 at the Glu47–Ans50 portion. The dashed lines represent hydrogen bonds.

To address similar situations, simulation of CNTs might benefit from implementing many-body potentials such as the adaptive intermolecular reactive empirical bond-order

(AIREBO) developed for treating the elasticity, energy, and vibrational states of carbon, hydrocarbons, and polymers.[82-85]

2.3.1.2 The P1 and the P6

The P6 is another MT-lateral segment, a simple loop that links the H1 helix and the B2 strand of β-tubulin. It consists of forty (40) residues (I_{24}SDEHGIDPTGSYHGDSD-LQLERINVYYNEATGNKYVPRA$_{65}$) coded 24–65 in 1JFF.pdb[37]. The P6 was the third strongest binder to the CNT among the P1–P10. The P6 most considerable contribution to its LJ potential energy was made by Arg64 and the phenyl ring of Tyr52. The P6's Arg64 was stabilized at a ~3.5 Å distance to the CNT due to its H-bonding to Asp90 in the P7. The binding energy of Tyr52 fluctuated as its phenyl ring rotated from parallel to the tube from 0–45°. The intra-peptide H-bond of Tyr52 to Asn54 also weakened the peptide's binding to the CNT, suggesting that the Asn mutation with a more hydrophobic amino acid (*e.g.* Leu) prevents the disadvantageous interaction. The LJ energy was favorably affected by water molecules' H-bonds to the neighboring residues of Tyr52 during 1.182–1.219 μs, causing the Tyr ring to adapt a parallel conformation to the CNT that was also supported by the H-bond with the Arg284 of the P9 and consequently strengthened the vdW force between the P6 and the CNT. Similarly, a Tyr and an Arg interacted in the P2, P5, P6, P9 (each consisting of the Arg), and the P2, P4, and P9 (each consisting of the Tyr), resulting in the improvement of the binding conformation of the latter group to the CNT, which indicates the importance of the Tyr for the CNT coating. (**Table 2.4** and **Figure A3**)

The P1, from α-tubulin, is known as the α-H1–B2 loop in the α, β-heterodimer tubulin, with forty (40) residues (Y_{24}CLEHGIQPDGQMPSDKTIGGGDDSFNTFFSETGAGK-

HVP$_{63}$), coded as 24–63.[37] Due to the dense intra-peptide interactions in the P1, only a few hydrophobic residues consisting of aromatic or cyclic moieties (*i.e.*, Phe49, Tyr24, Phe52, Pro63, His28, and Gly44) were available for binding to the CNT. The P6 is the equivalent peptide to the P1 in β-tubulin. They have 75.7% sequence similarity and 32.4% identity. The former covers a broader tube surface area than the latter. Compared to the P1', the P1 binding to the CNT resulted in a helix folding (*i.e.*, α- and 3-helix) at Cys25–His28 and Asp47–Asn50 segments that demonstrated the impact of the CNT binding. That was also shown in the P6 compared to the P6', as it maintained its β-strand configuration at Tyr52–Glu55 and Asn59–Val62, similar to its SS in the MT. The P6' highly fluctuated in a coil configuration since it was influenced by its exposure to the aqueous environment. (**Figure 2.5A–F** and **Table A4**)

There were three major conformational changes in the P1 that occurred during *i.* 1.130–1.155 μs, *ii.* 1.375–1.380 μs, and *iii.* 1.430–1.435 μs. Unlike the third time-interval, during the first two, the P1–CNT binding improved due to His28 and Gly44 movements and hydrophobic binding to the CNT. However, the third was related to Tyr24 and its ring's rotation from parallel, in a range of 0°–30° with respect to the CNT's long axis. Its hydroxyl moiety made H-bond to water molecules and formed H-bond bridges to His28 and Glu27. Those water molecules pulled the ring away from the CNT that weakened the vdW forces. That suggests a mutation at Tyr24 with Phe will omit its hydroxyl H-bonding effects and prevent declining P1 affinity to the CNT. (**Figure A4**)
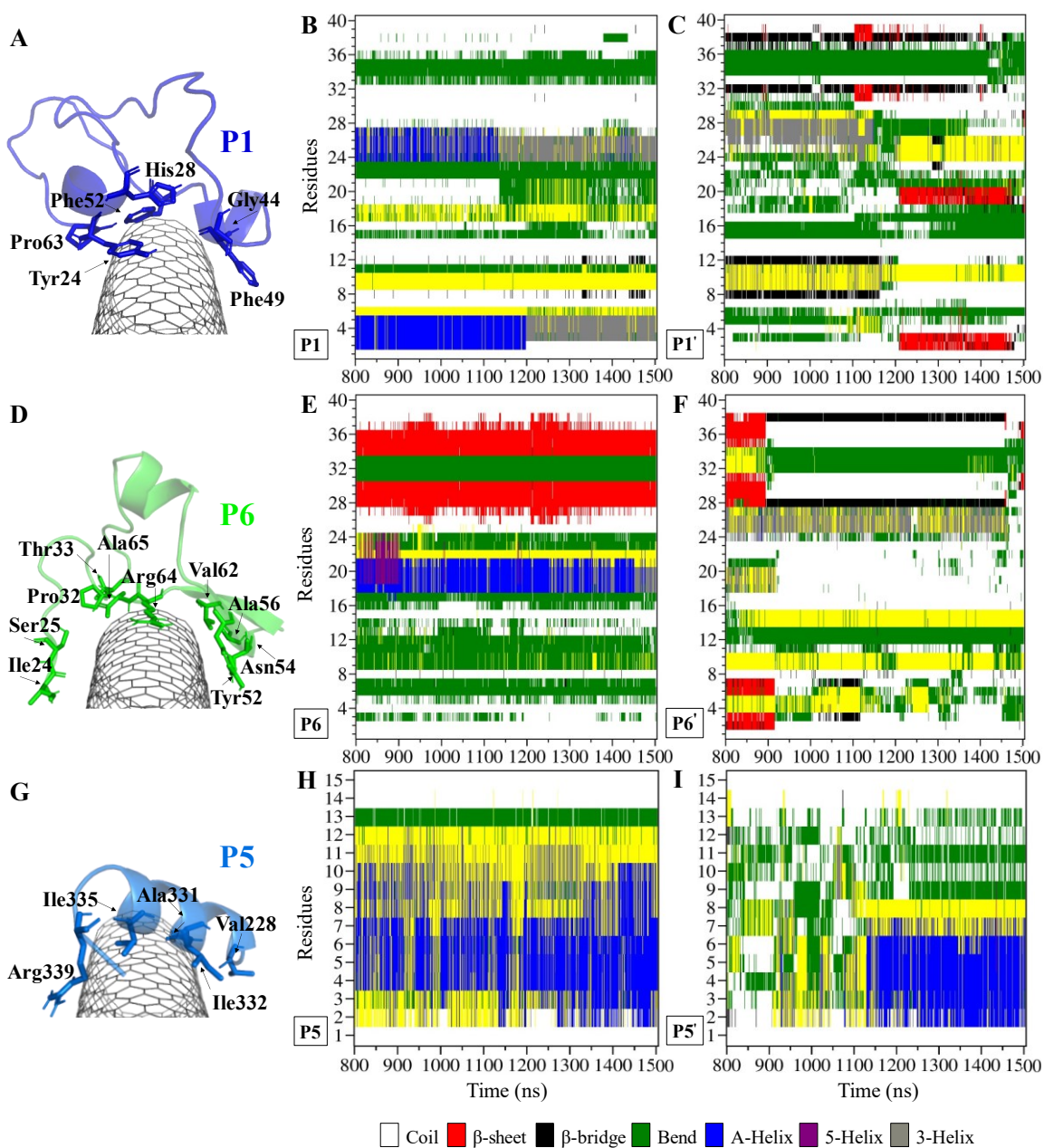
Figure 2.5 Binding profile of (A) the P1 (the C1 system) with a hydrophobic cyclic residue moiety structure core, (D) the P6 (the C2 system) coating a wider CNT surface area than the P1, and (G) the P5 (the C1 system). The SS analysis is based on the Dictionary Secondary Structure of Protein (DSSP) algorithm during 0.800–1.500 µs of the (B) P1, (E) P6, and (H) P5 on the CNT, and their CNT–peptides-free states the (C) P1', (F) P6', and (I) P5'. The

residue numbering of 1–40 corresponds to Tyr24–Pro63 in the P1 and Ile24–Ala65 in the P6.

Comparing RMSD of the P1 and the P6 to their respective CNT-free conformations, the P1' and the P6', demonstrates the CNT's role in refining their SS with steady binding ability. (**Figure A1C–D** and **Figure 2.5A–F**)

2.3.1.3 The P2 and the P7

The P2, from α-tubulin, has eleven residues (R_{79}TGTYRQLFHP$_{89}$) with amino acids coded as 79–89 in 1JFF.pdb[37], known as the α-H2–B3 loop. It is equivalent to the P7 of β-tubulin, also with eleven residues (G_{81}PFGQIFRPDN$_{91}$), coded as 81–91 at the β-H2–B3 loop[37]. The P2 and P7 have 77.8% sequence similarity and 44.4% identity. They adapted a combination of folding as coil, bend, and turn during the MD simulation time, distinct from the lengthier peptides (*e.g.*, the P1 and P6) at the bound state on the CNT. (**Table A4** and **Figure A5A–B**)

The turn formation prevented the maximum LJ interaction of the P2 with the CNT at the Thr80–Thr82 segment, caused by Tyr83 spatial hindrance and the frequent perpendicularly reorienting Tyr83 and Phe87 aromatic rings. The P2's N-terminal (Arg79–Tyr83) wrapped around the CNT in a crook shape, creating a condition for a steady intra-peptide H-bond between Arg79 and Arg84. That facilitated a stable flat conformation of Arg84 aliphatic moiety and π–π interactions of its guanidine moiety to the CNT. The Arg, along with the contribution of the bridging water molecules, formed H-bond to Gln85. The N-terminal's Arg79 was also frequently H-bonded to Tyr83, which increased the distance

between the Thr80–Tyr83 segment and the CNT. Replacing Tyr83 and Phe87 of the P2 with a simpler hydrophobic residue (e.g. Leu) could reduce their steric hindrance, result in better exposure of the P2 to the CNT, and increase the P2's binding affinity. In addition, mutating Arg84 also with a more hydrophobic amino acid can reduce the potential H-bond formation. In the P7, Phe87 and Phe83 rings were also perpendicular to the CNT, similar to Phe87 of the P2. Their conformations prevented the P7 full interactions, negatively affecting the P7–CNT binding and weakening the LJ energy. As suggested for the P2, replacing Phe83 with a non-aromatic hydrophobic residue is expected to enhance the P7's binding property. (**Figure A6–A7**)

2.3.1.4   The P3 and the P8

The P3 and P8 were the shortest sequences among the P1–P10 with low intrinsic hydrophobicity. The P3 is the H4–T5 loop in α-tubulin, with five amino acids ($L_{157}SVDY_{161}$), numbered 157–161.[37] The five residues shaping the P8 are from β-tubulin ($E_{159}EYPD_{163}$), coded as 159–163.[37] (**Table 2.4** and **Figure A8–A9**)

The P3 and the P8 showed supporting roles for their neighboring peptides. For instance, the inter-peptide interaction profile of the P3 showed that it mainly involved the hydrophobic, polar, and charged amino acids of the P2 and P5, demonstrating its role was primarily auxiliary to the conformation of its adjacent peptides to CNT binding. (**Figure 2.6**)
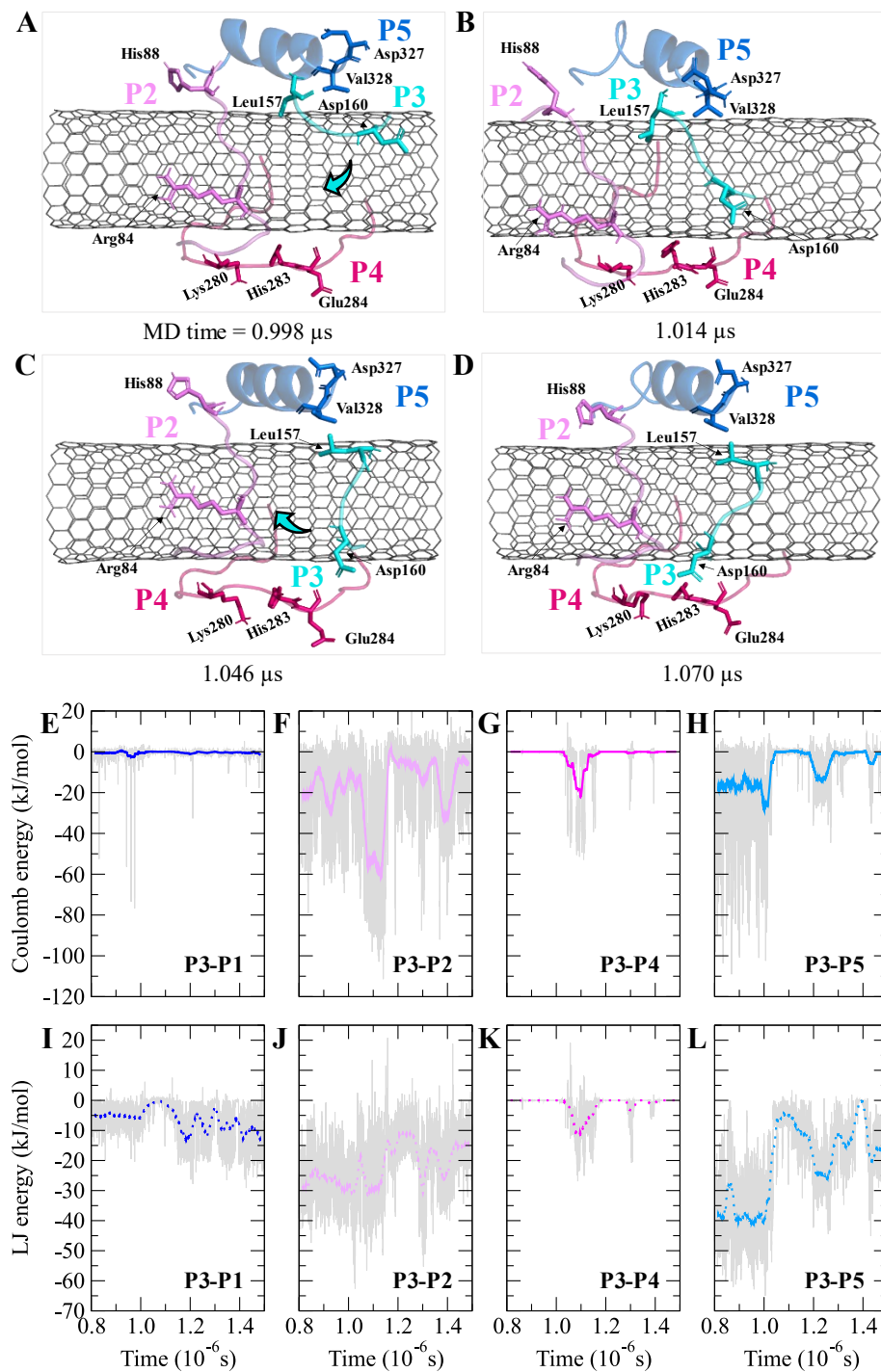
Figure 2.6 The P2–P5 binding to the CNT and the inter-peptide coulomb and LJ energy of the (A, E) the P1–P3, the (B, F) the P2–P3, the (C, G) the P3–P4, and the (D, H) the P3–P5 on the CNT. Graphs were generated with averaging every 300 frames.

2.3.1.5   The P5 and the P10

The P5 belongs to α-tubulin and comprises fifteen (15) amino acids (D_{327}VNAAIAT-IKTKRSI$_{341}$) coded as 327–341 in 1JFF.pdb.[37] Unlike the other peptides, the P5 lacks aromatic or cyclic side chains, affecting the magnitude of its LJ potential energy in the CNT binding. The P10 of β-tubulin also has fifteen amino acids (D_{329}EQMLNVQNKNSSYF$_{343}$), equivalent to 329–3431.[37] The sequence similarity and identity between the P5 and P10 are 66.7% and 16.7%, respectively. Due to the CNT presence, the P5 and the P10 folded into α-helix, 3-helix, and turn configurations during the MD simulation time. The unstable turn configuration of the P5 was caused by Arg339. It shifted away from the tube, disturbed the intra-peptide H-bonding of the P5 that is necessary for maintaining the helicity. Arg also caused steric-hindrance to other amino acids' binding to the CNT that cost ~19 kJ mol^{-1} in LJ potential energy of the P5–CNT binding. Mutating Arg339 with serine could eliminate the Arg size-related steric hindrance while contributing to the helix forming H-bonds. (**Figure 2.5G–I** and **Figure A5G, A10–A11**)

2.3.2   Peptides' Stability on the CNT and the Complex Solubility

The residues' root mean square fluctuation (RMSF) data were inspected to evaluate the peptides' SS compared to that in the MT or the peptides in their CNT-free states (*i.e.*, the P1'–P10'). A residue with an RMSF ≤ 2.0 Å was considered steady; otherwise, it was classified as highly flexible. According to that criterion, the peptides from β-tubulin, frequently appearing with random coil configuration and consisting of polar or ionic residues, presented higher RMSF than their counterparts in α-tubulin (*i.e.*, the P1–P5). Comparing residues' RMSFs in the CNT-bound peptides with their free forms showed the

configurational stability of the former, as seen in the C-terminal of the P1, the P2, and the

P4–P7. (**Figure 2.7** and **Table A5**)
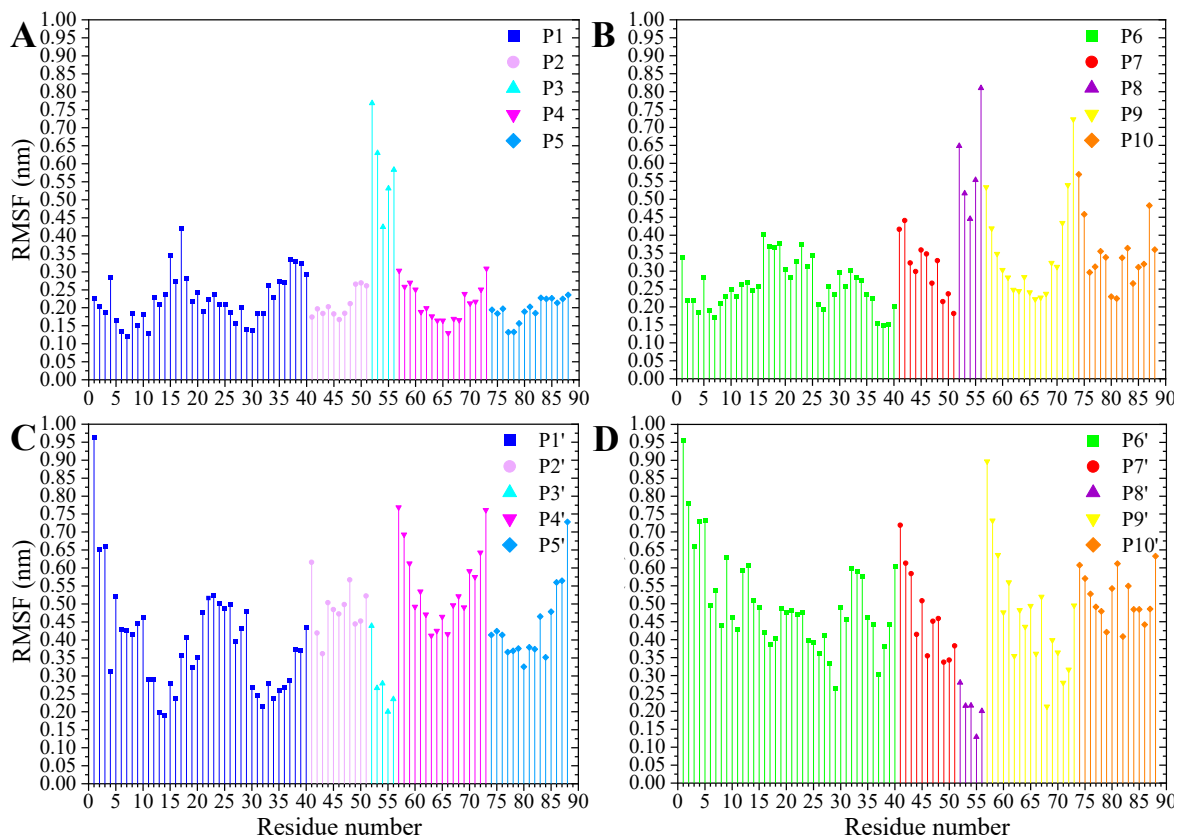
Figure 2.7 The RMSF of the amino acids (A) the P1–P5 and the (B) the P6–P10 on the CNT

and their CNT-free structure, (C) the P1'–P5' and (D) the P6'–P10', during 1.5 μs MD

trajectory.

The mobility of each peptide was also affected by its surrounding peptides, especially the

shortest peptides, the P3 and P8. Their CNT-presence RMSFs were substantially higher due

to the presence of other adjacent peptides and water molecules compared to their free states.

(**Figure 2.7**)

A ~3 Å dehydration gap near the CNT wall at its exterior and interior regions was due to the hydrophobicity of the pristine CNT that functioned in favor of the vdW interactions to the peptides' hydrophobic side chains and the CNT–peptides LJ energy. (**Figure A12**)

The water molecules triggered the charged and polar residues of the CNT-bound peptides to reorient towards the solvent and, consequently, altered the peptides' polar surface distribution on the tube. The peptides bound to the tube *via* polar or positively charged amino acids simultaneously formed H-bonds with the aqueous solvent molecules; for instance, those in the P1 (Glu27, Asp33, Lys40, Asp47, Lys60, and His61), the P4 (Glu284), the P5 (Asp327 and Lys336), the P6 (Asp26, His28, Asp39, Asp41, and Arg48), the P7 (Arg88), the P9 (Glu290), and the P10 (Asp329 and Lys338). That suggests their potential to improve CNT solubilization and dispersibility in water. The peptides' effects on the CNT's solubility vary depending on the number of H-bonds formed. For instance, the P6 had a considerably higher number of H-bonds with its surrounding water molecules (in the C2) than the P1 (in the C1). The P2, P8, P9, and P10 displayed a superior potential for influencing the CNT solubility over the P3, P4, P5, and P7. (**Figure 2.8**, **Figure A13A–J**, and **Table A6**)

The hydrophilic surface of the β-tubulin peptides (the C2) was ~51.5 nm^2, which was more significant than of the peptides from α-tubulin (the C1), ~44 nm^2 since the C2 peptides have 54 polar side chains (including the charged residues) compared to 48 of the C1. Thus, the C2 system functioned better than the C1 in favor of CNT's solubility. Conversely, the peptides from α-tubulin, hydrophobically interacting with the CNT, resulted in a higher coating in the C1 of ~22 nm^2 compared to ~19 nm^2 surface area in the C2. (**Table A7**)
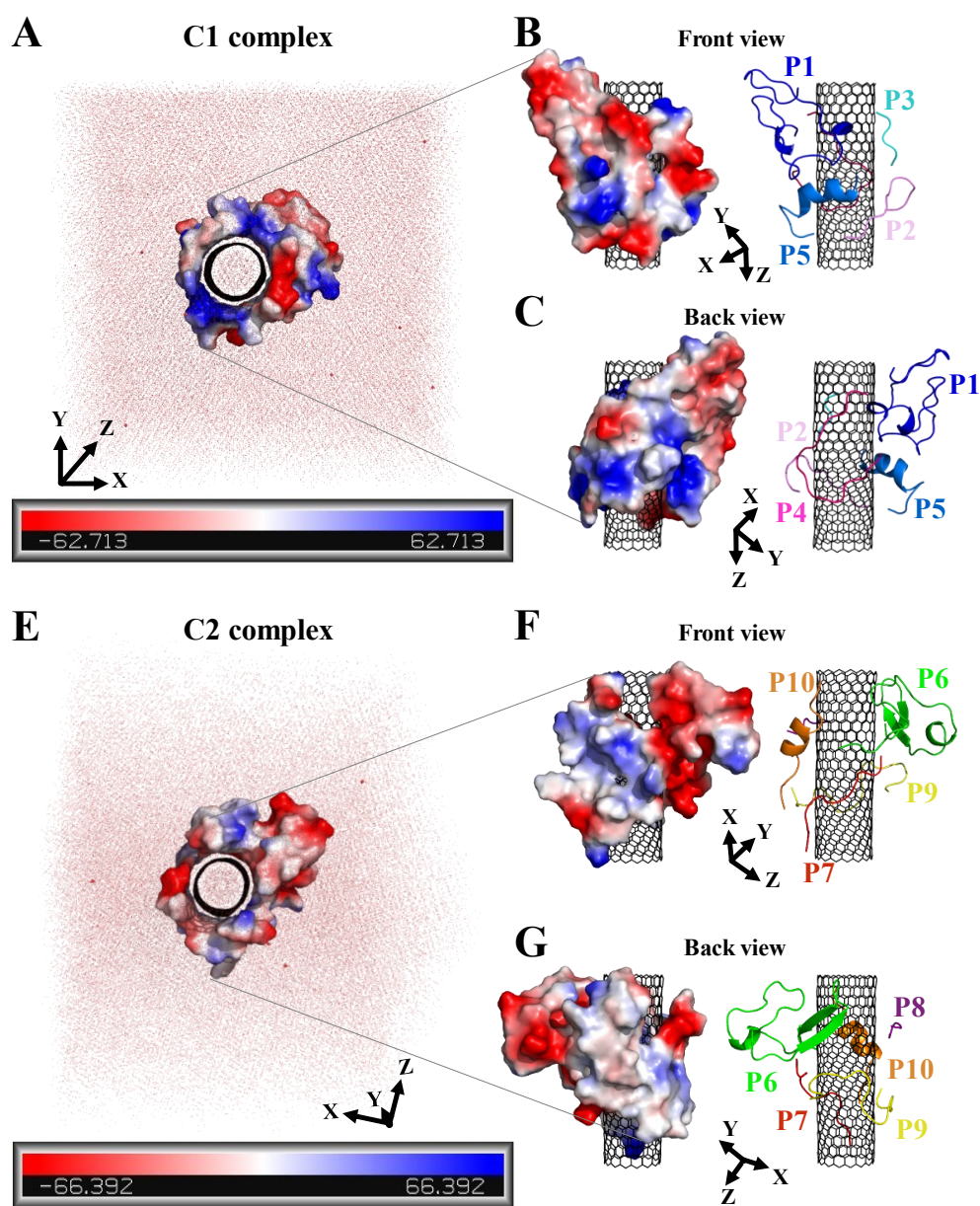
Figure 2.8 The peptides' polar surface distribution in (A) the C1 and (E) the C2. The front and back views of (B, C) the C1 and (F, G) the C2. Negative charge or polarity (red), and the positive charge or polarity of the amino acids (blue).

The CNTs randomly and diffusively traversed from their initial position in the solvent box of the peptide-bound and unbound systems. The CNT's radius of gyration, R_g[66, 67], was calculated according to Equation 2.3. The R_g of the unbound CNT was less than

its peptide-bound form, indicating the broad distribution of the peptides' atoms around the tube's center of mass in the C1 and C2 during the complexes' rotational and transitional motions. It was a consequence of the peptides' hydrophilic nature and their interactions to the aqueous polar environment, causing the hydrodynamic shell around the CNT–peptides complexes to expand and increase the R_g. Equation 2.3 has some limitations. (**Equation 2.3** and **Figure 2.9**)

$$Rg\ (x) = \sqrt{\frac{\sum_{i=1}^{N} m_i\ (R_i(y)^2 + R_C(z)^2)}{\sum_{i=1}^{N} m_i}} \qquad \textbf{Equation 2.3}$$

Radius of gyration of a molecule (m) about the x, y, and z axes.

The CNT's mean squared displacement (MSD)[86] was calculated as a function of time. The diffusion coefficient (D_A) was also calculated, according to Einstein's relation[87], to calculate the CNT's position deviation. (**Equation 2.4–6**)

$$MSD = \lim_{t \to \infty} \langle \| \boldsymbol{r}_i(t) - \boldsymbol{r}_i(0) \|^2 \rangle_{i \in A} \qquad \textbf{Equation 2.4}$$

$$D_A = \frac{1}{6} \lim_{t \to \infty} \frac{MSD}{t} \qquad \textbf{Equation 2.5}$$

$$D_A = \frac{kT}{6\pi\eta Rg} \qquad \textbf{Equation 2.6}$$

$r_i(t) - r_i(0)$ is the distance (vector) traveled by the COM of an ith particle over time t in a solvent with η viscosity, k, Boltzmann constant, and temperature T.
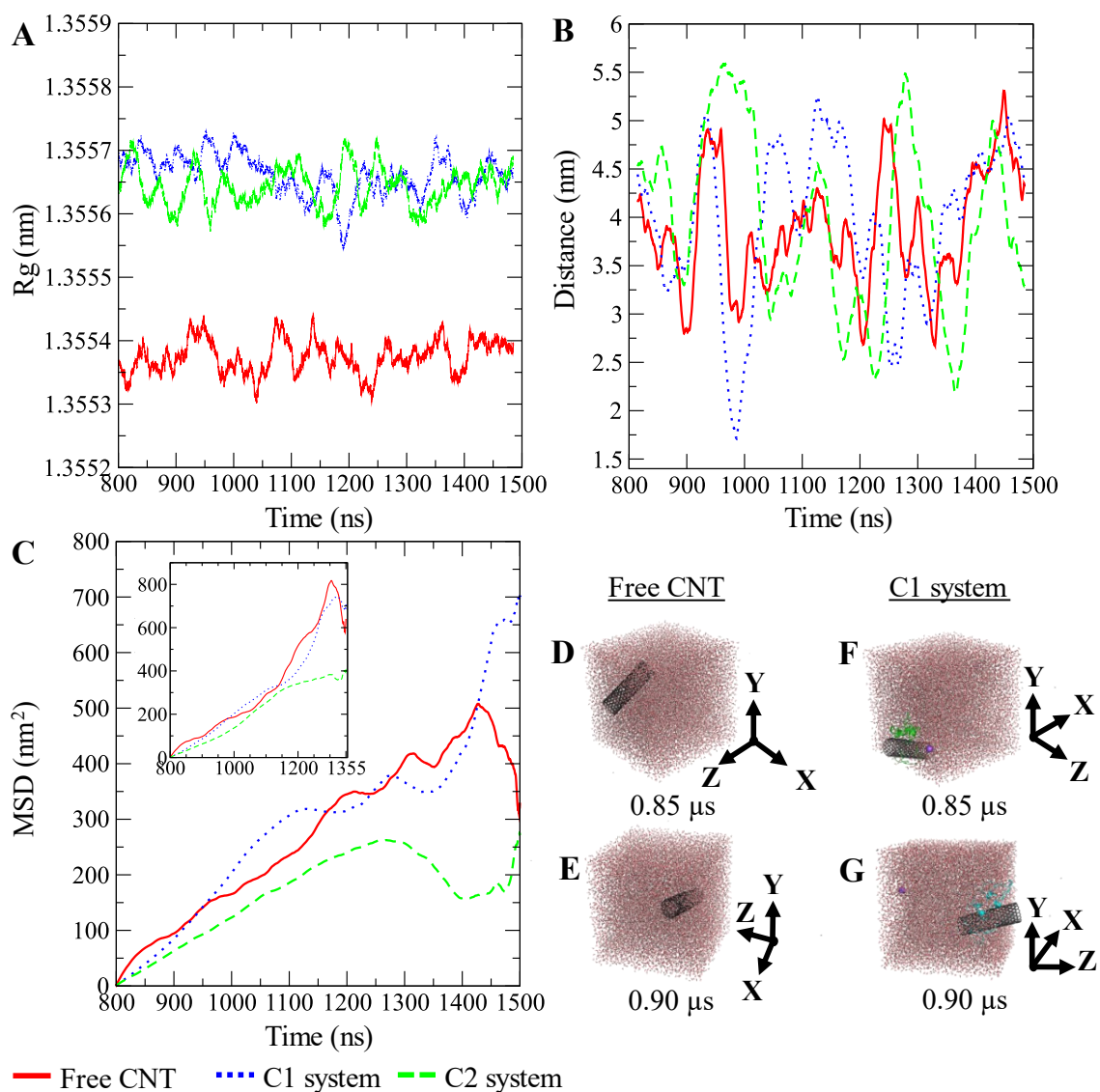
Figure 2.9 The pristine CNT, the C1, and the C2 systems. (A) *R*g, (B) the DCOM between the water box and each CNT, (C) MSD. (D, E) The pristine CNT and (F, G) the C1 system (the P1–P5) simulation boxes. Graphs were generated with averaging every 300 frames.

The D_A of the unbound pristine, the CNT–peptides in the C1, and the C2 systems were 1.21×10^8 nm^2 s^{-1}, 1.38×10^8 nm^2 s^{-1}, and 0.99×10^8 nm^2 s^{-1}. They were obtained by least-squares fitting the best straight line of each MSD graph. The D_A estimated a restricted flux

of the CNT–peptides complex in the C2 system, pertinent to its controlled motions by the more hydrophilic peptides of β-tubulin (the P6–P10) than α-tubulin's (the P1–P5). The polar amino acids created a hydrodynamic shell around the hydrophobic CNT that carried several water molecules involved in the H-bond networks or polar interactions and thus directly affected the complexes' R_g. (**Table 2.5** and **Table A7**)

Table 2.5 Diffusion coefficients of the CNT according to the MSD data linearity trend over the 0.800–1.355 µs of simulation time.

System	Diffusion (nm^2 s^{-1})
Pristine (peptide-free) CNT	$2.40 \pm 2.53 \times 10^{-10}$
C1	$2.18 \pm 1.26 \times 10^{-10}$
C2	$1.48 \pm 0.34 \times 10^{-10}$

The R_g determines the D_A and is influenced by several factors, including the peptides' amino acid composition. The magnitude of the amino acids' hydrophobicity or hydrophilicity regulates binding strength to the tube and the peptides' tendency to stretch out towards the aqueous environment. Accordingly, they shrink or expand the hydrodynamic shell around the CNT and alter the R_g in inverse proportion to D_A as demonstrated by the correlation of the MSD and R_g data. (**Figure 2.9**)

The P6–P10 presented positive LJ energy due to the inter-peptide repulsion forces that improved their distribution on the CNT in the complex C2 better than the P1–P5 in the C1 complex, wherein the peptides clustered on one side of the tube. The inter-peptides relations in the C1 were predominantly governed by the electrostatic forces, while the vdW force had

a more significant contribution to the P1–P5 binding to the CNT in the C2. (**Figure A14–A15**)

2.3.3 Antimitotics Binding

The peptides' binding to drugs was assessed using a molecular docking method. Seventeen MT-binding agents were studied that included PTX[37], docetaxel[38], taccalonolide[39], epothilones (*i.e.*, A, B, D, and ixabepilone)[40, 41], cyclostreptin[42], dictyostatin[43], discodermolide[44], zampanolide[45], and dolastatin.[51] The crystal structures of the drugs bound to α–β tubulin heterodimer exhibit they all are bound to at least one amino acid in the M-loop of β-tubulin. It also shows that the P5 (α-H10), the P6 (β-H1–B2), and particularly the P9 (β-M-loop) to be critical for the CNT functionalization for drug delivery due to their key roles in the binding of several ligands to the tubulin subunits. For instance, epothilone A (4O4I.pdb[46]) encounters the highest number of amino acids in the MT binding site at the β-M-loop (the P9) with Pro274, Leu275, Thr276, Arg278, Gln281, Gln282 and Arg284. Taxol (1JFF.pdb)[37] binds to more than one protein segment, β-H1–B2 (the P6) and β-M-loop (the P9), similar to dolastatin (4X1I.pdb[51]) that is hosted in the MT by α-H10 (the P5) and β-M-loop (the P9) or phomopsin A (3DU7.pdb[52]) by α-H10 (the P5) and β-H1–B2 (the P6). (**Table 2.6** and **Figure 2.10**)

According to the docking results, the two lowest binding energies of the ligand–peptides associated with phomopsin A (neutral and protonated at N1 atom) and laulimalide bound to the P6 and the P7 (in the C2). The neutral phomopsin A presented the highest binding affinity (-26.56 kJ mol^{-1}) among the ligands. (**Table 2.7** and **Figure 2.10–11**)

Table 2.6 Microtubule targeting antimitotics and the crystal structure of their complex with α, β-heterodimer along with their identification code in the RCSB Protein Data Bank. The "α" and "β" refer to the tubulin α and β-subunits.

| Anticancer Drugs	PDB ID	Peptides bound amino acids to the anticancer drugs
Paclitaxel	1JFF[37]	β-tubulin: Asp26, Glu27 (**P6**), Pro274, Leu275, Thr276, Arg278 (**P9**)
Docetaxel	1TUB[38]	β-tubulin: Pro274, Leu275, Thr276, Arg278 (**P9**)
Taccalonolide AJ	5EZY[39]	β-tubulin: Thr276, Arg278 (**P9**) / β-tubulin: Arg278, Gln282 (**P9**)
Epothilone A	4O4I[46]	β-tubulin: Pro274, Leu275, Thr276, Arg278, Gln281, Gln282, Arg284 (**P9**) β-tubulin: Pro274, Leu275, Thr276, Arg278, Gln281 (**P9**)
Epothilone B	7DAE[41]	β-tubulin: Pro274, Leu275, Thr276, Arg278, Gln281, Arg284 (**P9**)
Epothilone D	7DAD[41]	β-tubulin: Pro274, Thr276, Gln281, Arg284 (**P9**)
Ixabepilone	7DAF[41]	β-tubulin: Pro274, Leu275, Thr276, Gln281, Leu286 (**P9**)
Cyclostreptin	6QTN[42]	β-tubulin: Arg278 (**P9**)
Dictyostatin	5MF4[43]	β-tubulin: Pro274, Leu275, Thr276, Arg278, Gln282 (**P9**) β-tubulin: Pro274, Leu275, Thr276, Arg278 (**P9**)
Discodermolide	5LXT[44]	β-tubulin: Pro274, Leu275, Thr276, Arg278, Gln282 (**P9**) β-tubulin: Pro274, Leu275, Thr276, Arg278 (**P9**)
Zampanolide	4I4T[45]	β-tubulin: Pro274, Thr276, Arg278, Gln281, Arg284 (**P9**)
Laulimalide	4O4H[46]	β-tubulin: Asn334, Val335, Asn339 (**P10**)
Peloruside A	4O4J[46]	β-tubulin: Asn339 (**P10**) / β-tubulin: Asn339, Tyr342 (**P10**)
Vinblastine	4EB6[49]	α-tubulin: Asn329, Ile332, Lys336 (**P5**)
Dolastatin	4X1I[51]	α-tubulin: Asn329 (**P5**) β-tubulin: Arg278 (**P9**) / β-tubulin: Gln281, Tyr283 (**P9**)
Phomopsin A	3DU7[52]	α-tubulin: Asn329 (**P5**) β-tubulin: His37 (**P6**)
Eribulin	5JH7[53]	α-tubulin: Asn329 (**P5**)
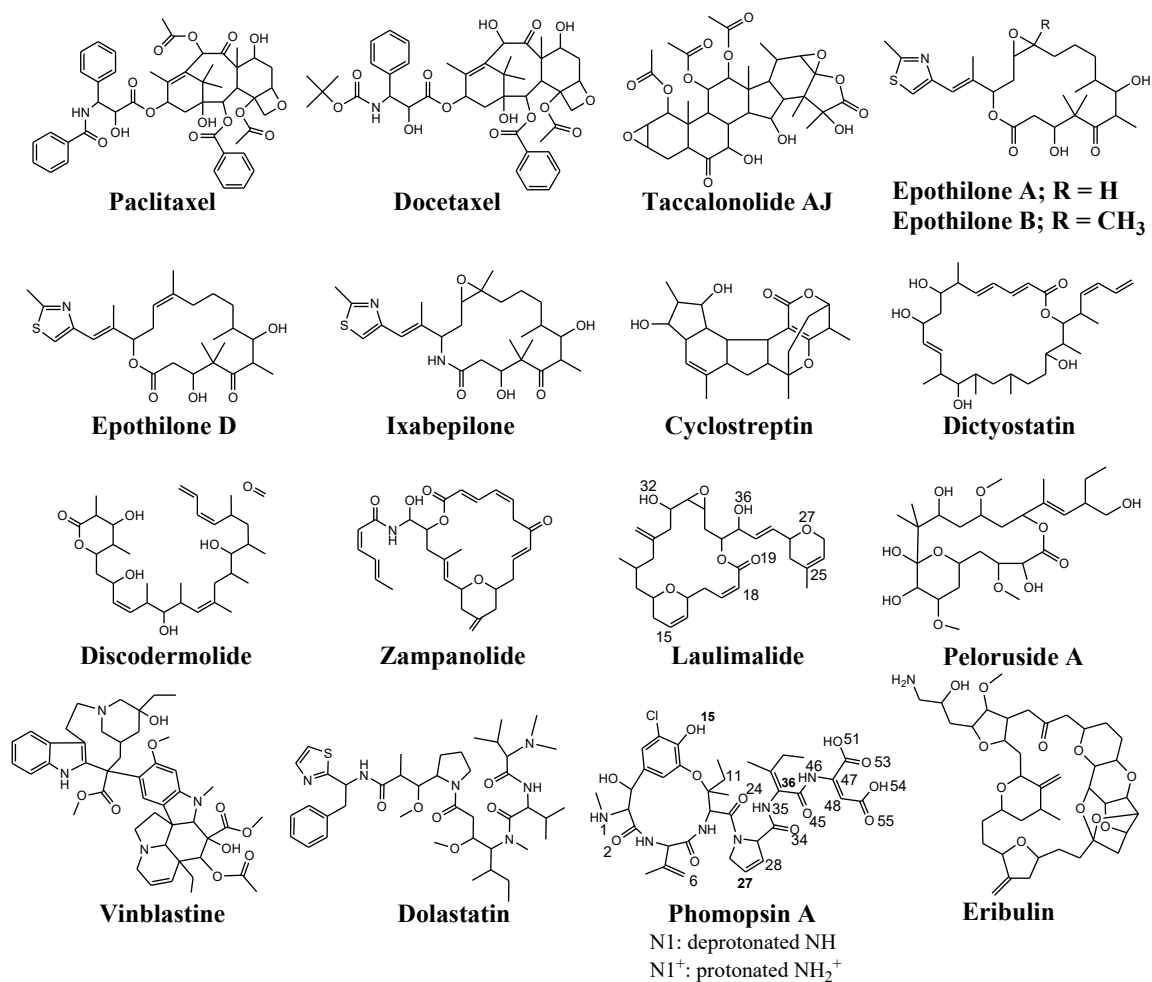
Figure 2.10 The chemical structures of seventeen (17) tubulin anticancer binding drugs in the docking ligand library, drawn and numbered using Chemdraw software.

Table 2.7 The top 13 docking solutions of the anticancer tubulin ligands bound to the C1 and C2 complexes ranked based on the binding energy.

Agent	System	Binding energy (kJ mol^{-1})	Ligand-binding peptides	Involving amino acids
Phomopsin A (neutral)	C2	−26.56	P6 and P7	H-bond: Glu27, His28, Leu42, Asn50, Arg64 (**P6**) vdW: Asp26, His28, Gly29, Arg64 (**P6**), Arg88 (**P7**)
Phomopsin A (protonated)	C2	−17.99	P6 and P7	H-bond: His28, Gln43 (**P6**), and Arg88, Asp90 (**P7**) vdW: Asp26, Glu27, Gln43, Leu42, Asn91 (**P6**) Ionic: Glu290 (**P9**)
Laulimalide	C2	−17.79	P6 and P7	H-bond: Glu27, Gln43, Asn50 (**P6**), Asp90 (**P7**) vdW: Glu27, His28, Gly29, Ile49 (**P6**)
Epothilone A	C2	−17.01	P6 and P7	H-bond: Asp26, Glu27, His28, Gly29, Gln43 (**P6**), Arg88 (**P7**) vdW: His28, Arg48 (**P6**)
Epothilone D	C2	−14.79	P6 and P7	H-bond: Glu27, Gln43 (**P6**), Asn91 (**P7**) vdW: His28 (**P6**), Arg88 (**P7**)
Cyclostreptin	C2	−13.75	P7 and P10	H-bond: Gln85, Ile86 (**P7**), Ser341 (**P10**) vdW: Gln85, Ile86 (**P7**)
Epothilone A	C1	−12.06	P1	H-bond: Ile42, Gly44, Gly45 (**P1**) vdW: Asp47 (**P1**)
Discodermolide	C2	−12.04	P6 and P7	H-bond: Asp26, His28 (**P6**), Arg88, Asn91 (**P7**) vdW: Arg88 (**P7**)
Eribulin	C2	−11.87	P6 and P7	H-bond: Asp26, Asn50 (**P6**), Asn91 (**P7**) vdW: Asn50 (**P6**), Asp90 (**P7**)
Cyclostreptin	C1	−11.46	P1 and P5	H-bond: Tyr24 (**P1**), Lys338 (**P5**) vdW: Thr41 (**P1**)
Zampanolide	C2	−11.21	P7	H-bond: Asp90, Asn91 (**P7**) vdW: His28 (**P6**), Arg88, Asp90 (**P7**)
Docetaxel	C2	−9.52	P6 and P7	H-bond: Asp26, Glu27, Asn50 (**P6**), Arg88, Pro89, Asn91 (**P7**) vdW: Leu42, Gln43 (**P6**), Pro89 (**P7**)
Zampanolide	C1	−7.60	P1	H-bond: Gly44, Gly45 (**P1**) vdW: Pro37, Lys40 (**P1**)
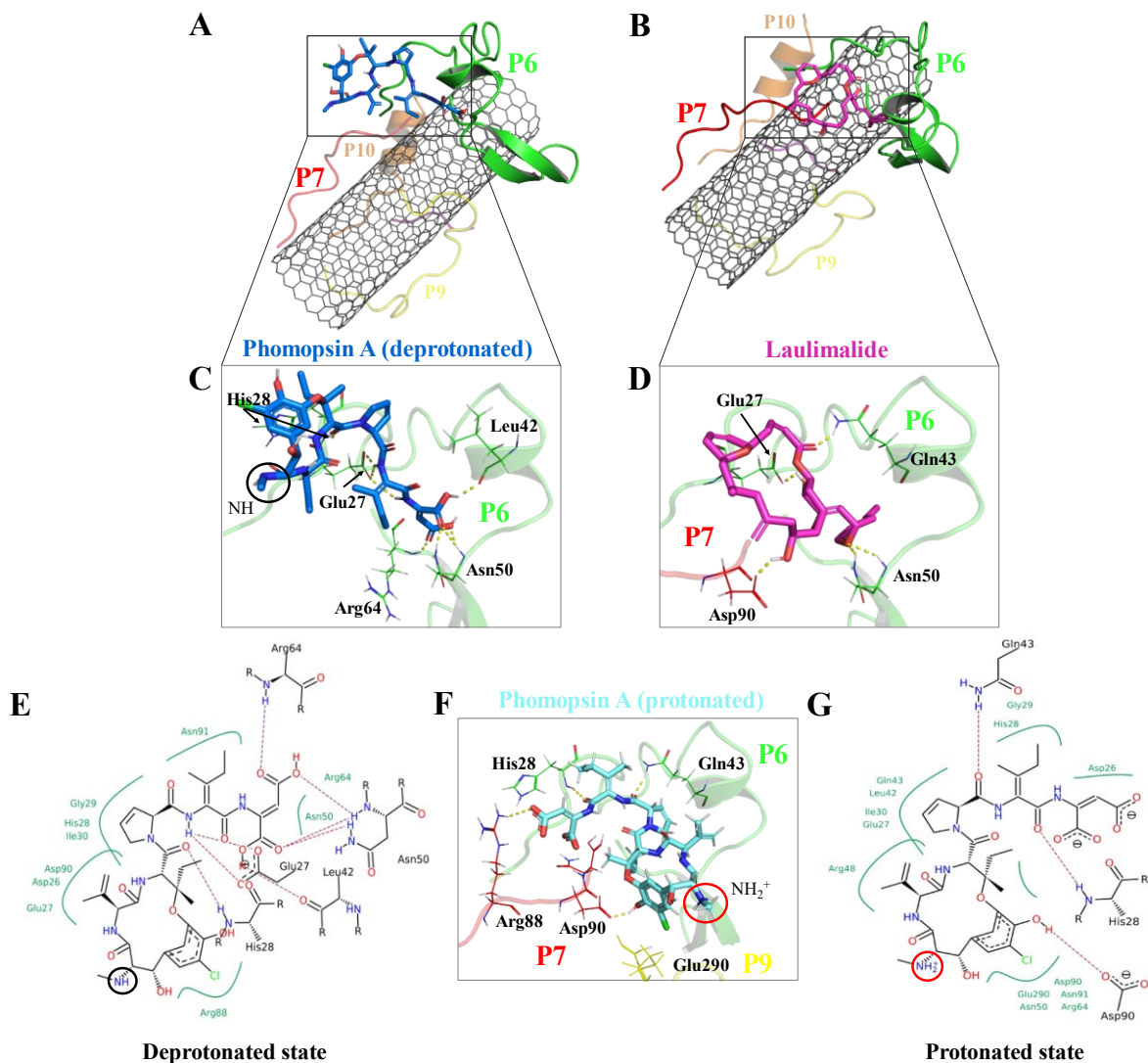
Figure 2.11 The binding profile of (A, C)* neutral phomopsin A (blue), (B, D)* laulimalide (magenta), and protonated phomopsin A (cyan). (E, G) Interactions of the protonated and neutral phomopsin A with the P6 and P7 amino acids. Dashed lines represent H-bonds.

*: The interactions of neutral phomopsin A consisted of H-bonds to the P6: its O24 with His28 amide hydrogen; H35 with the two Glu27 carboxyl oxygen atoms; H46 with Glu27 carboxyl oxygen; H51 with Leu42 carbonyl oxygen; the O53 and O54 atoms formed weak H-bonds with Asn50 amide hydrogen; similar to O55 with Arg64. Phomopsin A formed polar interactions with Arg88 of the P7 through its O2 atom: its C28 atom affected by Gly29 backbone carbons through hydrophobic interactions similar to His28 of the P6 and the C11 atom of the ligand and Arg64 of the P6 and the C48. The protonated phomopsin A made weak H-bonders between the hydrogen of His28 (the P6) and the O45 of the ligand, similar to Gln43 (the P6) with the O34 atoms. Another hydrogen bond occurred between the NH of the

guanidine in Arg88 (the P7) and the ligand's O55; the carbonyl oxygen of Asp90 (the P7) and the H15 atom of the protonated phomopsin

A. The hydrophobically interacting amino acids were Asp26 (the P6) with the C47, Glu27 (the P6) with the C36 and Leu42, and Gln43

(the P6) with the C27, where Leu 42 involved the C6 atom. Laulimalide was accommodated on the CNT by the P6 and the P7 through the

H32 H-binding to the carboxyl oxygen of Asp90 (the P7), similar to the O19 atom with the amide hydrogen of Gln43 (the P6). Other

involving amino acids of the P6 in the H-bond formation included Glu27 and Asn50, while His 26, Glu2, Ile49, and Gly29 bound to the

protonated phomopsin A via vdW forces.

The protonated phomopsin A (at the amide nitrogen, the N1) was also docked, and the FlexX scoring function ranked it as the second-best binding energy among the studied ligands (-17.99 kJ mol^{-1}). The conformation of the protonated phomopsin A was different from its neutral structure. The ionic interaction between the protonated amine moiety (H–N1$^+$) and the negatively charged oxygen atom of Glu290 in the P9 and its H-bond to the same residue caused the ligands' conformational difference in the protonated and deprotonated states, resulting in the loss of minor interactions detected in the neutral ligand and 8.56 kJ mol^{-1} increase of binding energy (-26.56 kJ mol^{-1} vs. -17.99 kJ mol^{-1}) in the protonated form. The third strongest binding was associated with laulimalide, with -17.79 kJ mol^{-1} binding energy. (**Table 2.7** and **Figure 2.10–11**)

Remarkably, the pair of the P6–P7 was the most preferred binding site for several ligands, including the phomopsin A (neutral and protonated), laulimalide, epothilone A, epothilone D, discodermolide, eribulin, and docetaxel. The charged amino acids of the P6 attracted the P7 C-terminal Arg88 and Asp90 through electrostatic forces, which favored their combination for these drug bindings. (**Figure A16**)

2.4   Conclusions

In the presented work, a microtubule-inspired non-covalent functionalization of CNTs is proposed. Ten peptides consisting of the MT's lateral segments were studied for their potential binding to and increasing the solubility of a pristine CNT. Their effects on transforming the tube into an efficient drug carrier were also examined by analyzing the binding affinity of seventeen MT-targeting antimitotics to the functionalized CNT.

The P4 and the P9, equivalent to the M-loop of α- and β-tubulin, were bound to the CNT with the lowest LJ potential energies. The P4's amino acid composition enabled a peptide-conformation that satisfactorily adapted the tube's curve and resulted in a superior surface coating than the other nine peptides. However, a part of the P4 sequence was seen distant from the tube surface for ~30 ns of the simulation time, caused by the H-bond mediating water molecules between Tyr272 and Glu284 of the P4. The intra-peptide H-bond, facilitated by Tyr272, caused steric hindrance for the remainder of the P4's residues preventing its complete interactions to the CNT; thus, replacing Tyr272 with a Phe is expected to increase the peptide's binding affinity. The P9 binding to the CNT, mainly half-sequence length, was regulated by its polar and charged residues. Due to the size and its specific amino acids composition, the P9 can be better accommodated by CNTs with broader surface or greater dimensions than the CNT (16,0) used in this study. In addition, replacing its Glu290 with a hydrophobic residue is suggested to eradicate the undesired polar interactions and the H-bonds with the dynamic solvent molecules. The P2 (α-H2–B3), P5 (α-H10) and P7(β-H2–B3) showed the longest retention time on the CNT, displaying more frequent interactions with the tube than the other peptides. The intra-peptide H-bonds in the P6 (β-H1–B2), such as between Tyr52 and Asn54, negatively affected the P6 binding to the

CNT, costing its binding ability to the tube surface. The Asn mutation with a hydrophobic amino acid such as isoleucine can prevent the unfavorable effects. In the P1 (α-H1–B2), the equivalent segment of the P6 in β-tubulin, His28 played a critical role in strengthening the LJ potential energy due to the parallel position of His imidazole ring to the tube. However, the rotation of the Tyr's phenyl ring under the influence of the H-bonding to Glu27, His28, and water molecules weakened the P1 binding to the CNT. A mutation at Tyr24 with Phe can omit the hydroxyl moiety's H-bonding capability and improve the P1's binding affinity.

The influence of the CNT's presence on the peptides' SS was most pronounced on the P1, P6, P5, and P10. It significantly improved the P1's configuration, stabilizing its folding as a helix and a 3-helix. Similarly, binding to the tube upgraded the configurational state of the P6 to a β-strand, more stable than the P6'. The CNT enables the P5 and P10 to maintain the same SS as in microtubule, whereas their CNT-free forms, the P5' and P10', acted as simple coils throughout the MD trajectory.

The P2 (α-H2–B3) demonstrated a unique structural conformation by wrapping its N-terminal around the CNT in a crook-like shape. However, its Arg84 made frequent H-bonds to Arg79, Gln85, and Tyr83, pulling the P2 segment (Thr80–Thr82) away from the CNT in some MD time frames. Tyr83 and Phe87 caused spatial hindrance for the P2's residues, preventing their complete engagement with the tube's carbocyclic substructures. Simple hydrophobic residues, such as Leu, Val, Ile, instead of Tyr83 and Phe87, can avert the steric hindrance effect, allowing the full-length exposure of the P2 to the CNT. Mutating Arg84 with a hydrophobic amino acid is also suggested to prevent the undesired H-bonds formation. Phe87 in the P7 (β-H2–B3) blocked the peptide's full-sequence involvements with the CNT, weakening its LJ binding energy; thus, a non-aromatic hydrophobic amino

acid instead of the Phe can enhance the P7's binding profile. The P3 (α-H4–T5) and the P8 (β-H4–T5) were the shortest peptides in sequence among the P1–P10, acted mainly as auxiliary agents to stabilize the conformational status of their adjacent peptides.

The peptides' effects on the CNT solubility depended on the number of H-bonds each makes with the solvent molecules. Due to its residue compositions, the P6 demonstrated more hydrogen bonds with water molecules (in the C2) than the P1 (in the C1). In particular, the P2, P8, P9, and P10 showed superior potential over the P3, P4, P5, and the P7, in enhancing the CNT's water solubility. It is noteworthy that peptides such as the P1, P4–P7, and the P9–P10, rich in polar or positively charged residues, could form strong bonds with the CNT and the solvent molecules through dynamic conformational reorientations, and thus augment CNTs solubilization. The hydrodynamic layer created by the peptides from β-tubulin in the C2 system was more widespread than the α-tubulin's in the C1 system. In contrast, the latter formed a broader hydrophobic coating than those from the β-tubulin. Therefore, we propose a functionalization with a combination of the amphiphilic peptides from both α- and β-tubulin to improve CNTs' aqueous solubility, cellular uptake, and efficiency to hold and transport hydrophobic drugs. That could help overcome the significant challenge in drug discovery concerning hydrophobic drugs' insolubility, leading to inefficient bioavailability, absorption, distribution, metabolism, and excretion from the human body. The presence of the hydrophilic peptides is expected to prevent the functionalized CNT from precipitating in the blood artery allowing better fluidity in the bloodstream. Despite the tube's frequent drift from the center of the water box up to 5.6 nm, as seen in the DCOM graph; it is considered minor, taking into account the $\sim 10^4$ nm diameter of the blood artery.

The drugs docking on the peptides demonstrated phomopsin A (neutral and protonated) and laulimalide as the top three best binders among the seventeen antimitotics. The two drugs were bound mainly to the P6 and the P7 of the C2 system. The charged amino acids of the P6 attracted the C-terminal charged groups of the P7 through electrostatic forces, shaping a pair-like format. In addition, the time spent on the CNT by the P6 and P7 were among the tube's top three dwelling peptides. According to the docked ligands' binding profiles, the P4 and the P9 (*i.e.* the M-loop) insignificantly participated in the ligands' binding. In particular, the P9's partial detachment from the CNT, in favor of H-bonds to the P6 and water molecules, indicated its imperfection as a functionalizing group. However, the long peptides in sequence, such as the P1 and the P6 with forty amino acids, or a pair of shorter peptides, such as the P6–P7, the P1–P5, and the P7–P10, can facilitate efficient conditions for a ligand binding. Remarkably, the P6–P7 pair was the most preferred binding site for several ligands, namely, phomopsin A (neutral and protonated), laulimalide, epothilone A, epothilone D, discodermolide, eribulin, and docetaxel.

The designed CNT–peptides complex is deemed a more biocompatible drug carrier and is more likely to increase CNT's cellular uptake or modulate neutrophil activation in the bloodstream than its pristine form, considering the improved binding capacity of the peptide-coated tube to the plasma proteins surface. The proposed functionalization approach is expected to help advance *in vitro* and *in vivo* attempts to design and develop bioapplicable and biocompatible functionalized CNTs.

2.5   Bibliography

1.   Rathinavel, S.; Priyadharshini, K.; Panda, D. A review on carbon nanotube: An overview of synthesis, properties, functionalization, characterization, and the application. *Materials Science and Engineering: B* **2021**, *268*, 115095.

2.   Zare, H.; Ahmadi, S.; Ghasemi, A.; Ghanbari, M.; Rabiee, N.; Bagherzadeh, M.; Karimi, M.; Webster, T. J.; Hamblin, M. R.; Mostafavi, E. Carbon Nanotubes: Smart Drug/Gene Delivery Carriers. *Int J Nanomedicine* **2021**, *16*, 1681–1706.

3.   Pennetta, C.; Floresta, G.; Graziano, A. C. E.; Cardile, V.; Rubino, L.; Galimberti, M.; Rescifina, A.; Barbera, V. Functionalization of Single and Multi-Walled Carbon Nanotubes with Polypropylene Glycol Decorated Pyrrole for the Development of Doxorubicin Nano-Conveyors for Cancer Drug Delivery. *Nanomaterials (Basel)* **2020**, *10* (6), 1073.

4.   Khoshoei, A.; Ghasemy, E.; Poustchi, F.; Shahbazi, M.-A.; Maleki, R. Engineering the pH-Sensitivity of the Graphene and Carbon Nanotube Based Nanomedicines in Smart Cancer Therapy by Grafting Trimetyl Chitosan. *Pharmaceutical Research* **2020**, *37* (8), 160.

5.   Ohta, T.; Hashida, Y.; Yamashita, F.; Hashida, M. Development of Novel Drug and Gene Delivery Carriers Composed of Single-Walled Carbon Nanotubes and Designed Peptides With PEGylation. *Journal of Pharmaceutical Sciences* **2016**, *105* (9), 2815–2824.

6.   Gangrade, A.; Mandal, B. B. Injectable Carbon Nanotube Impregnated Silk Based Multifunctional Hydrogel for Localized Targeted and On-Demand Anticancer Drug Delivery. *ACS Biomaterials Science & Engineering* **2019**, *5* (5), 2365–2381.

7.   Phan, Q. T.; Patil, M. P.; Tu, T. T. K.; Le, C. M. Q.; Kim, G.-D.; Lim, K. T. Polyampholyte-grafted single walled carbon nanotubes prepared via a green process for anticancer drug delivery application. *Polymer* **2020**, *193*, 122340.

8.   Saeednia, L.; Yao, L.; Cluff, K.; Asmatulu, R. Sustained Releasing of Methotrexate from Injectable and Thermosensitive Chitosan-Carbon Nanotube Hybrid Hydrogels Effectively Controls Tumor Cell Growth. *ACS Omega* **2019**, *4* (2), 4040–4048.

9.   Meng, L.; Zhang, X.; Lu, Q.; Fei, Z.; Dyson, P. J. Single walled carbon nanotubes as drug delivery vehicles: Targeting doxorubicin to tumors. *Biomaterials* **2012**, *33* (6), 1689–1698.

10.   Bhirde, A. A.; Patel, S.; Sousa, A. A.; Patel, V.; Molinolo, A. A.; Ji, Y.; Leapman, R. D.; Gutkind, J. S.; Rusling, J. F. Distribution and clearance of PEG-single-walled carbon nanotube cancer drug delivery vehicles in mice. *Nanomedicine (Lond)* **2010**, *5* (10), 1535–46.

11.   Bhirde, A. A.; Patel, V.; Gavard, J.; Zhang, G.; Sousa, A. A.; Masedunskas, A.; Leapman, R. D.; Weigert, R.; Gutkind, J. S.; Rusling, J. F. Targeted killing of cancer cells in vivo and in vitro with EGF-directed carbon nanotube-based drug delivery. *ACS nano* **2009**, *3* (2), 307–316.

12.   Mohseni-Dargah, M.; Akbari-Birgani, S.; Madadi, Z.; Saghatchi, F.; Kaboudin, B. Carbon nanotube-delivered iC9 suicide gene therapy for killing breast cancer cells in vitro. *Nanomedicine* **2019**, *14* (8), 1033–1047.

13.   Liu, Z.; Robinson, J. T.; Tabakman, S. M.; Yang, K.; Dai, H. Carbon materials for drug delivery & cancer therapy. *Materials Today* **2011**, *14* (7), 316-323.

14.   Sanginario, A.; Miccoli, B.; Demarchi, D. Carbon Nanotubes as an Effective Opportunity for Cancer Diagnosis and Treatment. *Biosensors* **2017**, *7* (1), 9.

15.   Chagas, C. M.; Moss, S.; Alisaraie, L. Drug metabolites and their effects on the development of adverse reactions: Revisiting Lipinski's Rule of Five. *International Journal of Pharmaceutics* **2018**, *549* (1), 133–149.

16.   Flynn, M.; Heale, K. A.; Alisaraie, L. Mechanism of Off-Target Interactions and Toxicity of Tamoxifen and Its Metabolites. *Chemical Research in Toxicology* **2017**, *30* (7), 1492–1507.

17.   Chaudhary, H.; Fernandes, R. M. F.; Gowda, V.; Claessens, M. M. A. E.; Furó, I.; Lendel, C. Intrinsically disordered protein as carbon nanotube dispersant: How dynamic interactions lead to excellent colloidal stability. *Journal of Colloid and Interface Science* **2019**, *556*, 172–179.

18.   Díez-Pascual, A. M. Chemical Functionalization of Carbon Nanotubes with Polymers: A Brief Overview. *Macromol* **2021**, *1* (2), 64–83.

19.   Liu, X.; Hurt, R. H.; Kane, A. B. Biodurability of single-walled carbon nanotubes depends on surface functionalization. *Carbon* **2010**, *48* (7), 1961–1969.

20.   González-Lavado, E.; Iturrioz-Rodríguez, N.; Padín-González, E.; González, J.; García-Hevia, L.; Heuts, J.; Pesquera, C.; González, F.; Villegas, J. C.; Valiente, R.; Fanarraga, M. L. Biodegradable multi-walled carbon nanotubes trigger anti-tumoral effects. *Nanoscale* **2018**, *10* (23), 11013–11020.

21.   Kotchey, G. P.; Zhao, Y.; Kagan, V. E.; Star, A. Peroxidase-mediated biodegradation of carbon nanotubes in vitro and in vivo. *Advanced Drug Delivery Reviews* **2013**, *65* (15), 1921–1932.

22.   Todorova, N.; Makarucha, A. J.; Hine, N. D.; Mostofi, A. A.; Yarovsky, I. Dimensionality of carbon nanomaterials determines the binding and dynamics of amyloidogenic peptides: multiscale theoretical simulations. *PLoS Comput Biol* **2013**, *9* (12), e1003360.

23.   Ebrahim-Habibi, M.-B.; Ghobeh, M.; Mahyari, F. A.; Rafii-Tabar, H.; Sasanpour, P. An investigation into non-covalent functionalization of a single-walled carbon nanotube and a graphene sheet with protein G:A combined experimental and molecular dynamics study. *Scientific Reports* **2019**, *9* (1), 1273.

24.   Baweja, L.; Balamurugan, K.; Subramanian, V.; Dhawan, A. Effect of graphene oxide on the conformational transitions of amyloid beta peptide: A molecular dynamics simulation study. *Journal of Molecular Graphics and Modelling* **2015**, *61*, 175–185.

25.   Sun, Y.; Qian, Z.; Wei, G. The inhibitory mechanism of a fullerene derivative against amyloid-β peptide aggregation: an atomistic simulation study. *Physical Chemistry Chemical Physics* **2016**, *18* (18), 12582–12591.

26.   Bhabha, G.; Johnson, G. T.; Schroeder, C. M.; Vale, R. D. How Dynein Moves Along Microtubules. *Trends in Biochemical Sciences* **2016**, *41* (1), 94–105.

27.   Heale, K. A.; Alisaraie, L. C-terminal Tail of β-Tubulin and its Role in the Alterations of Dynein Binding Mode. *Cell Biochem Biophys* **2020**, *78* (3), 331–345.

28.   Shigematsu, H.; Imasaki, T.; Doki, C.; Sumi, T.; Aoki, M.; Uchikubo-Kamo, T.; Sakamoto, A.; Tokuraku, K.; Shirouzu, M.; Nitta, R. Structural insight into microtubule stabilization and kinesin inhibition by Tau family MAPs. *Journal of Cell Biology* **2018**, *217* (12), 4155–4163.

29.   Goodson, H. V.; Jonasson, E. M. Microtubules and Microtubule-Associated Proteins. *Cold Spring Harbor Perspectives in Biology* **2018**, *10* (6), a022608.

30.   Amos, L. A.; Schlieper, D. Microtubules and maps. *Adv Protein Chem* **2005**, *71*, 257–98.

31.   Manka, S. W.; Moores, C. A. The role of tubulin–tubulin lattice contacts in the mechanism of microtubule dynamic instability. *Nature Structural & Molecular Biology* **2018**, *25* (7), 607–615.

32.   Knossow, M.; Campanacci, V.; Khodja, L. A.; Gigant, B. The Mechanism of Tubulin Assembly into Microtubules: Insights from Structural Studies. *iScience* **2020**, *23* (9), 101511.

33.   Sui, H.; Downing, K. H. Structural basis of interprotofilament interaction and lateral deformation of microtubules. *Structure* **2010**, *18* (8), 1022–1031.

34.   Li, Z.; Alisaraie, L. Microtubules dual chemo and thermo-responsive depolymerization. *Proteins* **2015**, *83* (5), 970–81.

35.   Igaev, M.; Grubmüller, H. Microtubule instability driven by longitudinal and lateral strain propagation. *PLOS Computational Biology* **2020**, *16* (9), e1008132.

36.   Jordan, M. A.; Wilson, L. Microtubules and actin filaments: dynamic targets for cancer chemotherapy. *Current Opinion in Cell Biology* **1998**, *10* (1), 123–130.

37.   Löwe, J.; Li, H.; Downing, K. H.; Nogales, E. Refined structure of alpha beta-tubulin at 3.5 A resolution. *J Mol Biol* **2001**, *313* (5), 1045–57.

38.   Nogales, E.; Wolf, S. G.; Downing, K. H. Structure of the alpha beta tubulin dimer by electron crystallography. *Nature* **1998**, *391* (6663), 199–203.

39.   Wang, Y.; Yu, Y.; Li, G. B.; Li, S. A.; Wu, C.; Gigant, B.; Qin, W.; Chen, H.; Wu, Y.; Chen, Q.; Yang, J. Mechanism of microtubule stabilization by taccalonolide AJ. *Nat Commun* **2017**, *8*, 15787.

40.   Nettles, J. H.; Li, H.; Cornett, B.; Krahn, J. M.; Snyder, J. P.; Downing, K. H. The binding mode of epothilone A on alpha,beta-tubulin by electron crystallography. *Science* **2004**, *305* (5685), 866–869.

41.   Xiao, Q.; Xue, T.; Shuai, W.; Wu, C.; Zhang, Z.; Zhang, T.; Zeng, S.; Sun, B.; Wang, Y. High-resolution X-ray structure of three microtubule-stabilizing agents in complex with tubulin provide a rationale for drug design. *Biochem Biophys Res Commun* **2021**, *534*, 330–336.

42.   Balaguer, F. A.; Mühlethaler, T.; Estévez-Gallego, J.; Calvo, E.; Giménez-Abián, J. F.; Risinger, A. L.; Sorensen, E. J.; Vanderwal, C. D.; Altmann, K. H.; Mooberry, S. L.; Steinmetz, M. O.; Oliva, M.; Prota, A. E.; Díaz, J. F. Crystal Structure of the Cyclostreptin-Tubulin Adduct: Implications for Tubulin Activation by Taxane-Site Ligands. *Int J Mol Sci* **2019**, *20* (6), 1392.

43.   Trigili, C.; Barasoain, I.; Sánchez-Murcia, P. A.; Bargsten, K.; Redondo-Horcajo, M.; Nogales, A.; Gardner, N. M.; Meyer, A.; Naylor, G. J.; Gómez-Rubio, E.; Gago, F.; Steinmetz, M. O.; Paterson, I.; Prota, A. E.; Díaz, J. F. Structural Determinants of the Dictyostatin Chemotype for Tubulin Binding Affinity and Antitumor Activity Against Taxane- and Epothilone-Resistant Cancer Cells. *ACS Omega* **2016**, *1* (6), 1192–1204.

44.   Prota, A. E.; Bargsten, K.; Redondo-Horcajo, M.; Smith, A. B., 3rd; Yang, C. H.; McDaid, H. M.; Paterson, I.; Horwitz, S. B.; Fernando Díaz, J.; Steinmetz, M. O.

Structural Basis of Microtubule Stabilization by Discodermolide. *Chembiochem* **2017**, *18* (10), 905–909.

45. Prota, A. E.; Bargsten, K.; Zurwerra, D.; Field, J. J.; Díaz, J. F.; Altmann, K. H.; Steinmetz, M. O. Molecular mechanism of action of microtubule-stabilizing anticancer agents. *Science* **2013**, *339* (6119), 587–590.

46. Prota, A. E.; Bargsten, K.; Northcote, P. T.; Marsh, M.; Altmann, K. H.; Miller, J. H.; Díaz, J. F.; Steinmetz, M. O. Structural basis of microtubule stabilization by laulimalide and peloruside A. *Angew Chem Int Ed Engl* **2014**, *53* (6), 1621–5.

47. Gajewski, M. M.; Alisaraie, L.; Tuszynski, J. A. Peloruside, laulimalide, and noscapine interactions with beta-tubulin. *Pharm Res* **2012**, *29* (11), 2985–2993.

48. Waight, A. B.; Bargsten, K.; Doronina, S.; Steinmetz, M. O.; Sussman, D.; Prota, A. E. Structural Basis of Microtubule Destabilization by Potent Auristatin Anti-Mitotics. *PLoS One* **2016**, *11* (8), e0160890.

49. Ranaivoson, F. M.; Gigant, B.; Berritt, S.; Joullié, M.; Knossow, M. Structural plasticity of tubulin assembly probed by vinca-domain ligands. *Acta Crystallogr D Biol Crystallogr* **2012**, *68* (8), 927–934.

50. Chagas, C. M.; Alisaraie, L. Metabolites of Vinca Alkaloid Vinblastine: Tubulin Binding and Activation of Nausea-Associated Receptors. *ACS Omega* **2019**, *4* (6), 9784–9799.

51. Maderna, A.; Doroski, M.; Subramanyam, C.; Porte, A.; Leverett, C. A.; Vetelino, B. C.; Chen, Z.; Risley, H.; Parris, K.; Pandit, J.; Varghese, A. H.; Shanker, S.; Song, C.; Sukuru, S. C.; Farley, K. A.; Wagenaar, M. M.; Shapiro, M. J.; Musto, S.;

Lam, M. H.; Loganzo, F.; O'Donnell, C. J. Discovery of cytotoxic dolastatin 10 analogues with N-terminal modifications. *J Med Chem* **2014**, *57* (24), 10527–10543.

52.   Cormier, A.; Marchand, M.; Ravelli, R. B.; Knossow, M.; Gigant, B. Structural insight into the inhibition of tubulin by vinca domain peptide ligands. *EMBO Rep* **2008**, *9* (11), 1101–1106.

53.   Doodhi, H.; Prota, A. E.; Rodríguez-García, R.; Xiao, H.; Custar, D. W.; Bargsten, K.; Katrukha, E. A.; Hilbert, M.; Hua, S.; Jiang, K.; Grigoriev, I.; Yang, C. H.; Cox, D.; Horwitz, S. B.; Kapitein, L. C.; Akhmanova, A.; Steinmetz, M. O. Termination of Protofilament Elongation by Eribulin Induces Lattice Defects that Promote Microtubule Catastrophes. *Curr Biol* **2016**, *26* (13), 1713–1721.

54.   Rodriguez-Fernandez, L.; Valiente, R.; Gonzalez, J.; Villegas, J. C.; Fanarraga, M. L. Multiwalled Carbon Nanotubes Display Microtubule Biomimetic Properties in Vivo, Enhancing Microtubule Assembly and Stabilization. *ACS Nano* **2012**, *6* (8), 6614–6625.

55.   Pampaloni, F.; Florin, E.-L. Microtubule architecture: inspiration for novel carbon nanotube-based biomimetic materials. *Trends in Biotechnology* **2008**, *26* (6), 302–310.

56.   García-Hevia, L.; Fernández, F.; Grávalos, C.; García, A.; Villegas, J. C.; Fanarraga, M. L. Nanotube interactions with microtubules: implications for cancer medicine. *Nanomedicine* **2014**, *9* (10), 1581–1588.

57.   Li, Z.; de Barros, A. L. B.; Soares, D. C. F.; Moss, S. N.; Alisaraie, L. Functionalized single-walled carbon nanotubes: cellular uptake, biodistribution and applications in drug delivery. *International Journal of Pharmaceutics* **2017**, *524* (1), 41-54.

58.   Berman, H. M.; Westbrook, J.; Feng, Z.; Gilliland, G.; Bhat, T. N.; Weissig, H.; Shindyalov, I. N.; Bourne, P. E. The Protein Data Bank. *Nucleic Acids Research* **2000**, *28* (1), 235–242.

59.   Lalign program, Swiss Institute of Bioinformatics. *https://embnet.vital-it.ch/software/LALIGN_form.html*.

60.   Huang, X.; Miller, W. A time-efficient, linear-space local similarity algorithm. *Advances in Applied Mathematics* **1991**, *12* (3), 337–357.

61.   Grafmüller, A.; Noya, E. G.; Voth, G. A. Nucleotide-Dependent Lateral and Longitudinal Interactions in Microtubules. *Journal of Molecular Biology* **2013**, *425* (12), 2232–2246.

62.   Nogales, E.; Whittaker, M.; Milligan, R. A.; Downing, K. H. High-Resolution Model of the Microtubule. *Cell* **1999**, *96* (1), 79–88.

63.   Borys, F.; Joachimiak, E.; Krawczyk, H.; Fabczak, H. Intrinsic and Extrinsic Factors Affecting Microtubule Dynamics in Normal and Cancer Cells. *Molecules* **2020**, *25* (16), 3705.

64.   JCrystalSoft Nanotube Modeler. *http://www.jcrystal.com/products/wincnt/index.htm*

65.   Li, Z.; Tozer, T.; Alisaraie, L. Molecular Dynamics Studies for Optimization of Noncovalent Loading of Vinblastine on Single-Walled Carbon Nanotube. *The Journal of Physical Chemistry C* **2016**, *120* (7), 4061–4070.

66.   Van Der Spoel, D.; Lindahl, E.; Hess, B.; Groenhof, G.; Mark, A. E.; Berendsen, H. J. GROMACS: fast, flexible, and free. *J Comput Chem* **2005**, *26* (16), 1701–1718.

67. Hess, B.; Kutzner, C.; van der Spoel, D.; Lindahl, E. GROMACS 4: Algorithms for Highly Efficient, Load-Balanced, and Scalable Molecular Simulation. *Journal of Chemical Theory and Computation* **2008**, *4* (3), 435–447.

68. Kaminski, G. A.; Friesner, R. A.; Tirado-Rives, J.; Jorgensen, W. L. Evaluation and Reparametrization of the OPLS-AA Force Field for Proteins via Comparison with Accurate Quantum Chemical Calculations on Peptides. *The Journal of Physical Chemistry B* **2001**, *105* (28), 6474–6487.

69. Darden, T.; York, D.; Pedersen, L. Particle mesh Ewald: An N·log(N) method for Ewald sums in large systems. *The Journal of Chemical Physics* **1993**, *98* (12), 10089–10092.

70. Leach, A. R., *Molecular modelling : principles and applications*. Prentice Hall: Harlow, England; New York, 2001.

71. Hess, B.; Bekker, H.; Berendsen, H. J. C.; Fraaije, J. G. E. M. LINCS: A linear constraint solver for molecular simulations. *Journal of Computational Chemistry* **1997**, *18* (12), 1463–1472.

72. Maiorov, V. N.; Crippen, G. M. Size-independent comparison of protein three-dimensional structures. *Proteins* **1995**, *22* (3), 273-83.

73. Smith, L. J.; Daura, X.; van Gunsteren, W. F. Assessing equilibration and convergence in biomolecular simulations. *Proteins* **2002**, *48* (3), 487–496.

74. Rarey, M.; Kramer, B.; Lengauer, T. Multiple automatic base selection: protein-ligand docking based on incremental construction without manual intervention. *J Comput Aided Mol Des* **1997**, *11* (4), 369–384.

75.   Rarey, M.; Kramer, B.; Lengauer, T.; Klebe, G. A fast flexible docking method using an incremental construction algorithm. *J Mol Biol* **1996**, *261* (3), 470–489.

76.   Rarey, M.; Kramer, B.; Lengauer, T. Docking of hydrophobic ligands with interaction-based matching algorithms. *Bioinformatics* **1999**, *15* (3), 243–250.

77.   Böhm, H. J. Prediction of binding constants of protein ligands: a fast method for the prioritization of hits obtained from de novo design or 3D database search programs. *J Comput Aided Mol Des* **1998**, *12* (4), 309–23.

78.   Shen, J.-W.; Wu, T.; Wang, Q.; Kang, Y. Induced stepwise conformational change of human serum albumin on carbon nanotube surfaces. *Biomaterials* **2008**, *29* (28), 3847–3855.

79.   Eisenhaber, F.; Lijnzaad, P.; Argos, P.; Sander, C.; Scharf, M. The double cubic lattice method: Efficient approaches to numerical integration of surface area and volume and to dot surface contouring of molecular assemblies. *Journal of Computational Chemistry* **1995**, *16* (3), 273-284.

80.   Zhang, L.; Xiao, X.; Yuan, Y.; Guo, Y.; Li, M.; Pu, X. Probing Immobilization Mechanism of alpha-chymotrypsin onto Carbon Nanotube in Organic Media by Molecular Dynamics Simulation. *Scientific Reports* **2015**, *5* (1), 9297.

81.   Balamurugan, K.; Gopalakrishnan, R.; Raman, S. S.; Subramanian, V. Exploring the Changes in the Structure of α-Helical Peptides Adsorbed onto a Single Walled Carbon Nanotube Using Classical Molecular Dynamics Simulation. *The Journal of Physical Chemistry B* **2010**, *114* (44), 14048–14058.

82.   Brenner, D. W.; Shenderova, O. A.; Harrison, J. A.; Stuart, S. J.; Ni, B.; Sinnott, S. B. A second-generation reactive empirical bond order (REBO) potential energy

expression for hydrocarbons. *Journal of Physics: Condensed Matter* **2002**, *14* (4), 783–802.

83.   Panczyk, T.; Wolski, P.; Lajtar, L. Coadsorption of Doxorubicin and Selected Dyes on Carbon Nanotubes. Theoretical Investigation of Potential Application as a pH-Controlled Drug Delivery System. *Langmuir* **2016**, *32* (19), 4719–4728.

84.   Stuart, S. J.; Tutein, A. B.; Harrison, J. A. A reactive potential for hydrocarbons with intermolecular interactions. *The Journal of Chemical Physics* **2000**, *112* (14), 6472–6486.

85.   Wolski, P.; Nieszporek, K.; Panczyk, T. Carbon Nanotubes and Short Cytosine-Rich Telomeric DNA Oligomeres as Platforms for Controlled Release of Doxorubicin—A Molecular Dynamics Study. *International Journal of Molecular Sciences* **2020**, *21* (10), 3619.

86.   M.J. Abraham, D. v. d. S., E. Lindahl, B. Hess, and the GROMACS; team, d. GROMACS User Manual version 2016. **2018**.

87.   Allen, M. P.; Tildesley, D. J. Computer Simulations of Liquids Oxford Science Publications. **1987**.

Summary

ƒ-CNTs have emerged as an alternative and efficient tool for medicine applications, especially functionating as transporting and translocating therapeutic molecules (either for effective, localized drug and gene release, or then for other purposes, such as radio, vaccine, or stem cell delivery), aside from serving as reinforcement for composite implants; healing material, and scaffold; overall, all aspiring to benefit from their multifarious top-level properties. Taking advantage of CNTs' propitious attributes, a novel non-covalent CNT functionalization has been presented in this thesis comprising specific tubulin-based peptides (i.e. lateral-interaction segments of MT) for bioavailability and biocompatibility augmentation in an anticancer drug delivery system. The *in-silico* results provided verifiable data for tackling CNT aggregation with these segments, which indicated amelioration of the CNT's diffusivity and aqueous solubility and provided insights into the relevant CNT– peptide and drug–peptide properties. This study also proposed structural strategies to design better biologically adjustable and purposeful MT-bioinspired segments to optimize their binding performance on CNTs. Most importantly, the outstanding peptides β-tubulin H1–B2 and H2–B3 segments, called herein as the P6 and P7, were suggested as the best-combined candidates for CNT coating in terms of nanocarrier-bounding strength, positional and structural stability, tube retention time ability, dispersion enhancement, and tubulin-antimitotic binding-affinity capability, particularly considering to use this complex with

phomopsin A and laulimalide agents. The P6–P7 combination has unique characteristics worth further wet laboratory experiments.

Future prospects should have their attention on the following aspects. First, explore the CNT-double systems covered with the tubulin-based fragments of this study (i.e., the P1 to P10), evaluating them in several nanotube dimensions, to investigate in atomistic-level details their potential peptides' solubilization to prevent the CNT aggregation. Second, examine the differences between non-covalent and covalent interactions between the tube and the fragments, computationally and experimentally. Third, develop a testable system in laboratory and probe the selected peptide(s) performance, as well as *in vitro* and *in vivo* assessment. Finally, provide further insights toward designing a biomimetic peptide–CNT system and suggest better strategies for drug delivery designs, especially to tackle cancer.

List of Appendices
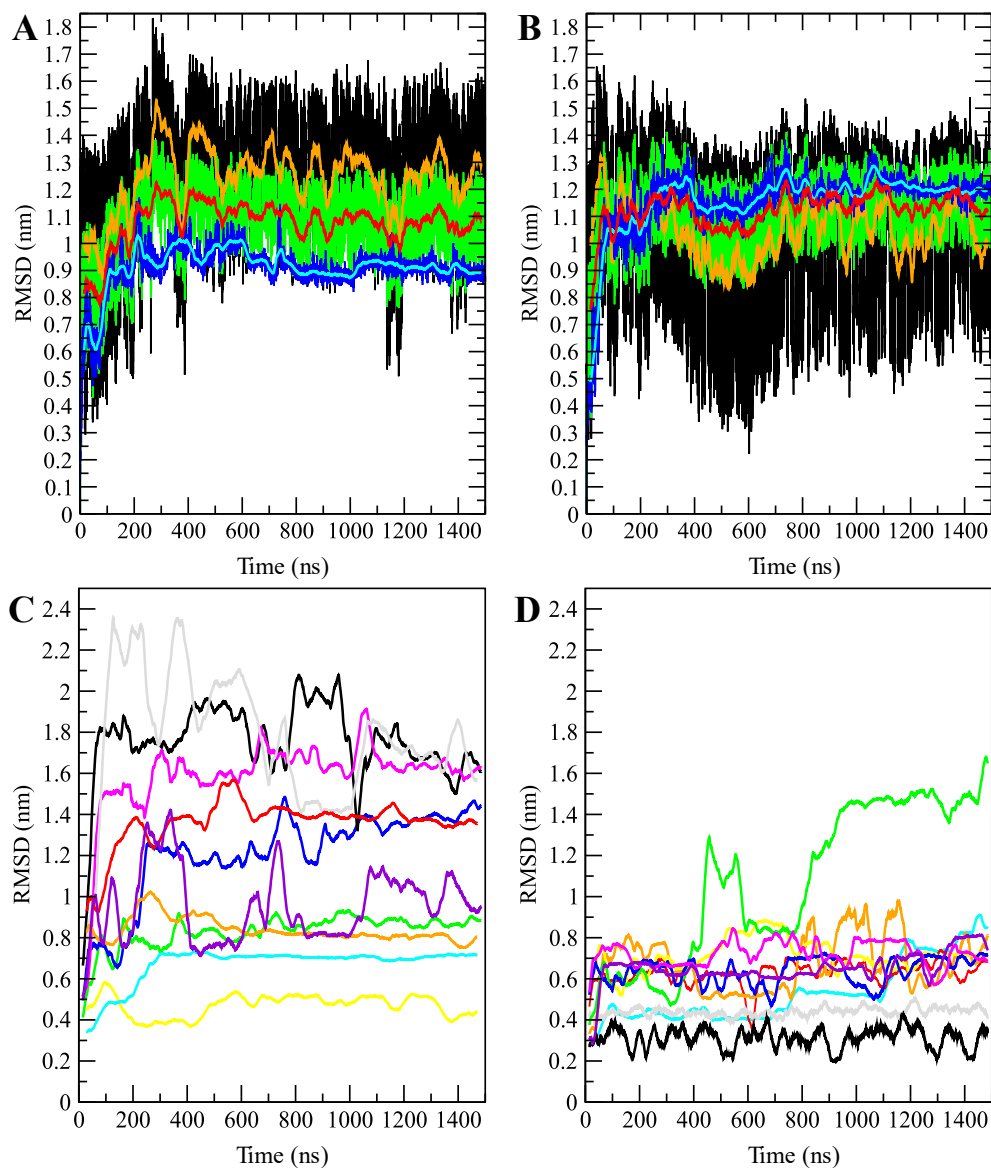
Figure A1 RMSD plots of the CNT (black, orange average), peptides (blue, cyan average), and peptides–CNT complex (green, red average) of the (A) C1 system and (B) C2 system. (C) Each peptide on the CNT: P1 (cyan), P2 (red), P3 (gray), P4 (orange), P5 (yellow), P6 (green), P7 (blue), P8 (black), P9 (magenta), and P10 (violet). (D) The free peptides with same coloring as in (C). Average lines were generated by averaging every 300 frames.
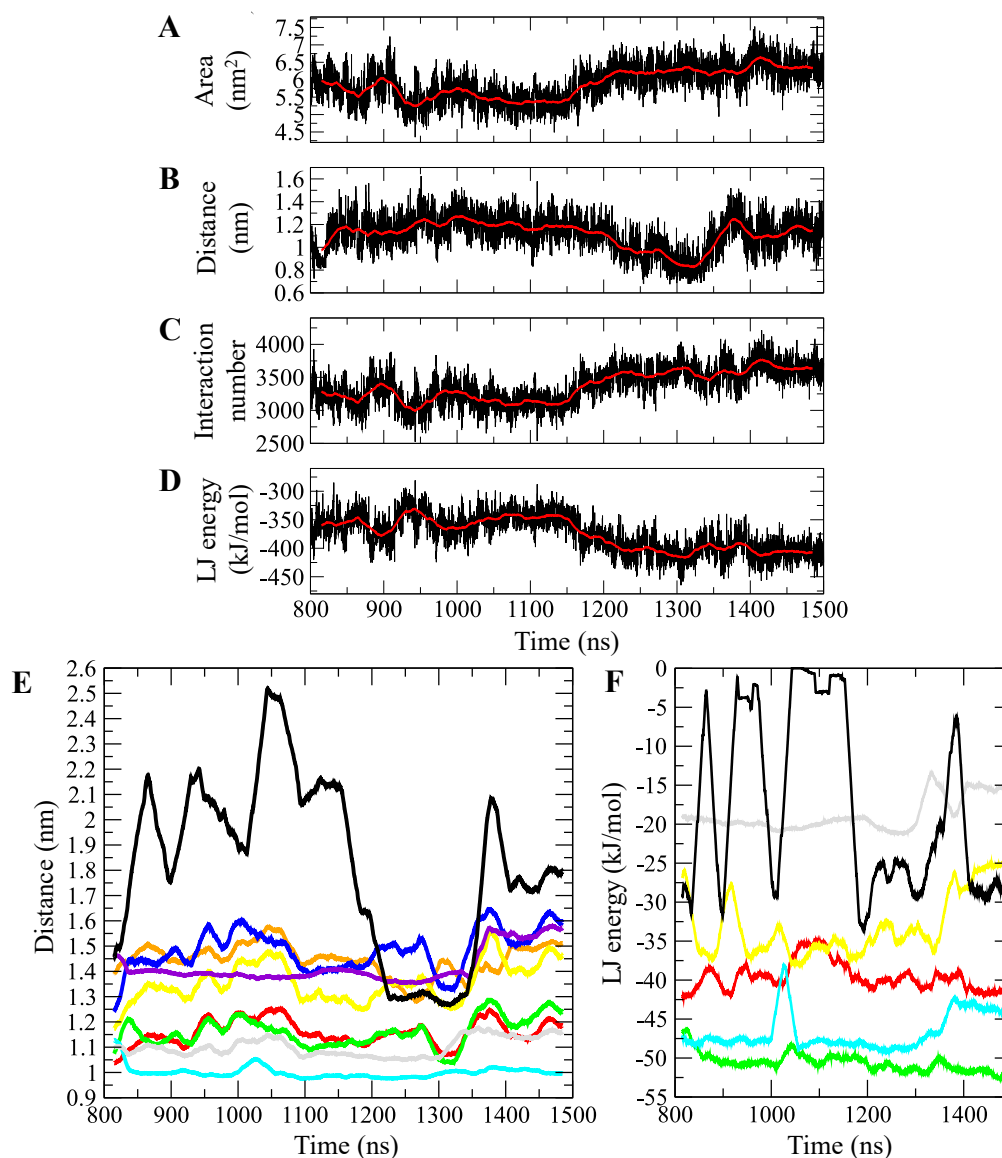
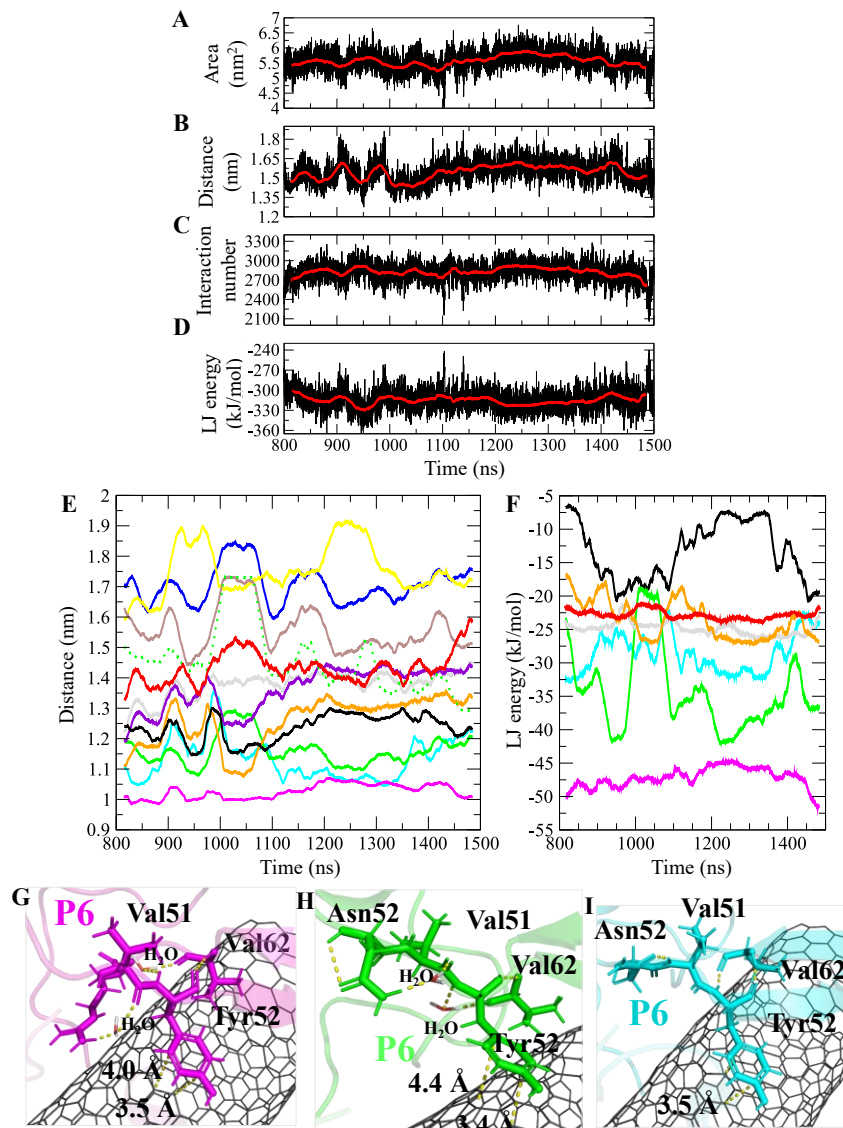**Figure A2** The time evolution of properties between the CNT and the P9: (A) SAS area, (B) DCOM, (C) interaction frequency (< 6 Å), and (D) LJ energy. (E) The DCOM average between the CNT and the P9 residues: Tyr283 (red), Arg278 (green), Gly279(blue), Gln282(yellow), Arg284 (cyan), Ala285 (gray), Leu286 (violet), Thr287 (orange), and Glu290 (black). (F) The LJ energy average of the CNT with: Arg278 (green), Arg284 (cyan), Tyr283 (red), Ala285 (gray), Gln282(yellow), and Glu290 (black). Graphs were generated with averaging every 300 frames of the 1.5 μs MD trajectory.

Figure A3 The properties between the CNT and the P6: (A) SAS area, (B) DCOM, (C) interaction number (< 6 Å), and (D) LJ energy. (E) The DCOM between the CNT and: Ile24 (cyan), Pro63 (violet), Arg64 (magenta), Tyr53 (blue), Asn54 (red), Tyr52 (green), Ser25 (black), Tyr61 (yellow), Val51 (brown), Val62 (gray), Ala65 (orange), and Asn50 (dotted green). (F) The LJ energy of the CNT with: Arg64 (magenta), Tyr52 (green), Ile24 (cyan), Val62 (gray), Asn54 (red), and Ser25 (black). Graphs were generated with averaging every 300 frames. (G) Mediating-water molecules with tilt Tyr52 ring at 3.5–4.4 Å and (H) 4.4 Å to the CNT. (I) Intra H-bond network (any water-bridging molecules) bringing a parallel Tyr52 ring at 3.5 Å to the CNT.
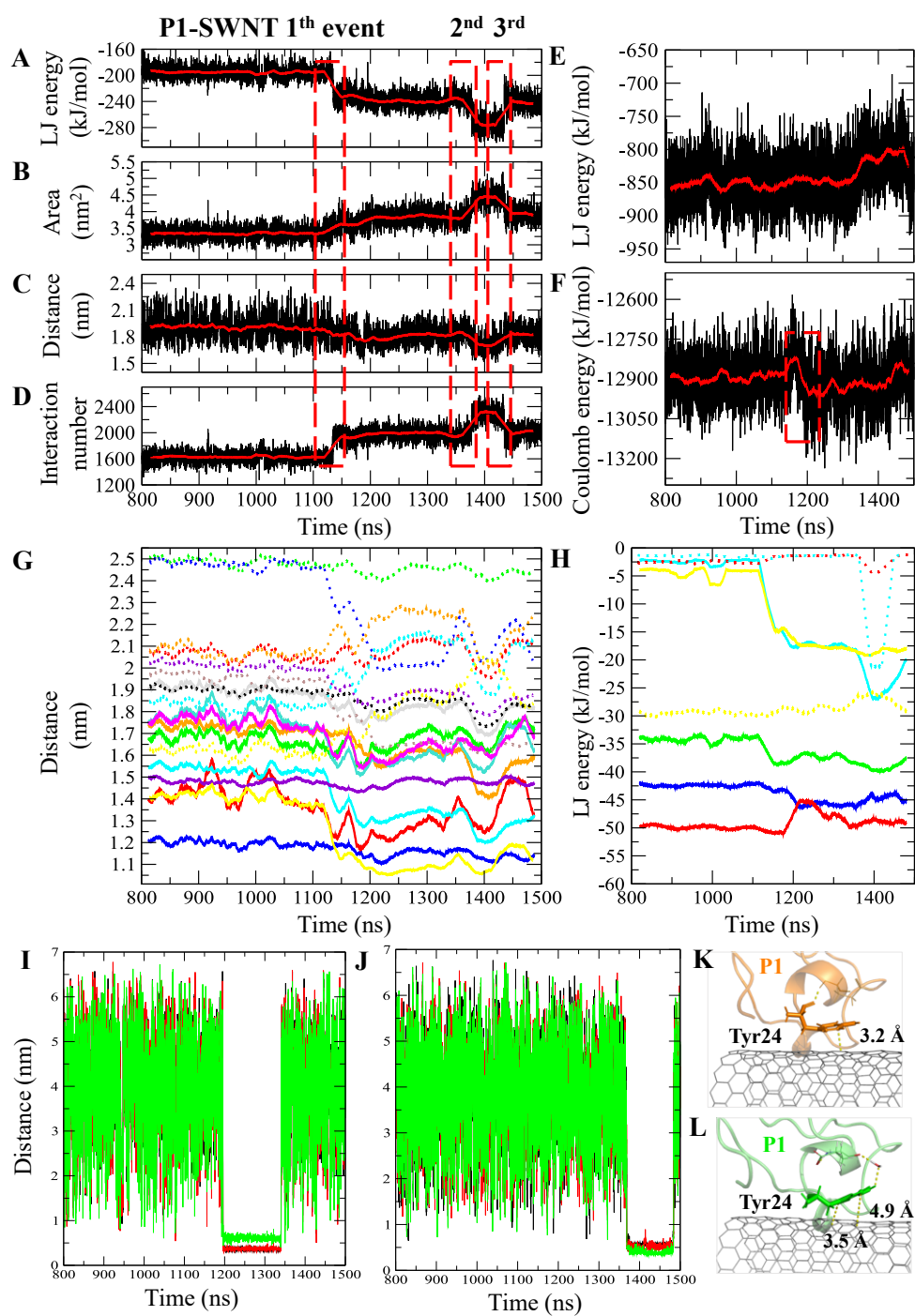
Figure A4 The properties between the CNT and P1: (A) LJ energy, (B) SAS area, (C) DCOM, and (D) interaction number (<6 Å). The P1 intramolecular (E) LJ and (F) coulomb energy. (G) The DCOM average between the CNT and: the P1 (gray), Phe52 (green), Asp46

(turquoise), Asn50 (magenta), Cys25 (orange), Glu27 (violet), Phe49 (red), His28 (cyan), Tyr24 (blue), and Gly44 (yellow), Pro63 (dotted yellow), Leu26 (dotted black), Ile30 (dotted violet), Ile42 (dotted brown), Val62 (dotted cyan), Phe53 (dotted red), Pro32 (dotted green), Pro37 (dotted blue), and His61 (dotted orange). (H) The LJ average energy between the CNT and: Tyr24 (blue), Phe49 (red), His28 (cyan), Phe52 (green), Gly44 (yellow), Pro63 (dotted yellow), and Val62 (dotted cyan). DCOM of the bridging-water molecule (I) ID 8709 that hydrogen bond Gly44 (black), Gly45 (red), and Lys40 (green) (1.195–1.340 μs), and (J) ID 14220 that bridges His28 (black), Gly43 (red), and Asn50 (green) (1.369–1.483 μs). Graphs were generated with averaging every 300 frames. (K) Tyr24 (P1) from parallel to (L) tilt at ~30° to the CNT length axis due to a water molecule bridging its hydroxyl to Glu28.
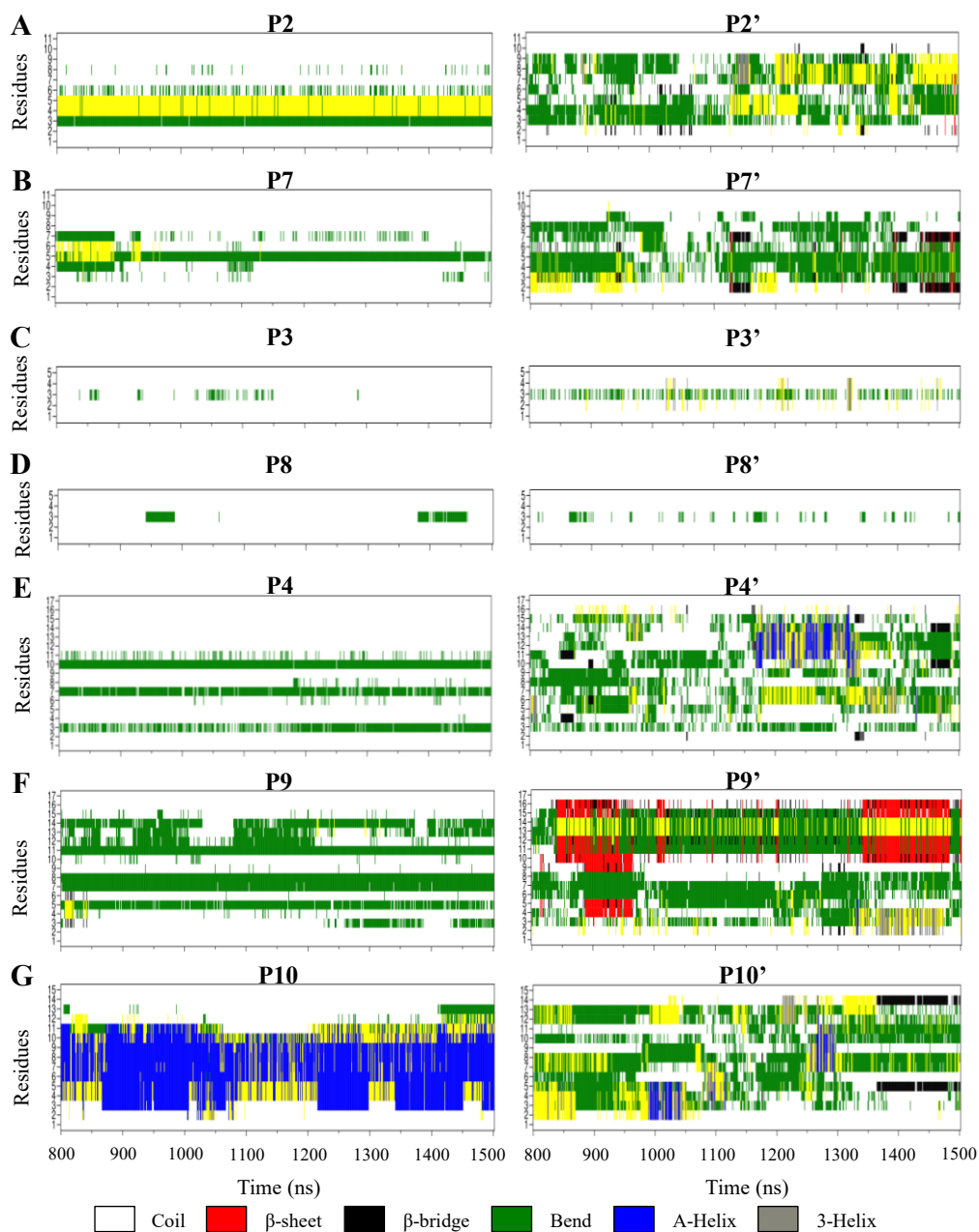
Figure A5 SS analysis based on the DSSP algorithm of the (A) P2 and P2' (residue numbering of 1–11 correspond to Arg79–Pro89[1]), (B) P7 and P7' (1–11 for Gly81–Asn91[1]), (C) P3 and P3' (1–5 for Leu157–Tyr161[1]), (D) P8 and P8' (1–5 for Glu159–Asp163[1]), (E) P4 and P4' (1–17 for

---

[1] Löwe, J.; Li, H.; Downing, K. H.; Nogales, E. *J Mol Biol* 2001, 313 (5), 1045–57.

Tyr272–Val288[1]), (F) P9 and P9' (1–17 for Pro274–Glu290[1]), and (G) P10 and P10' (1–15 for
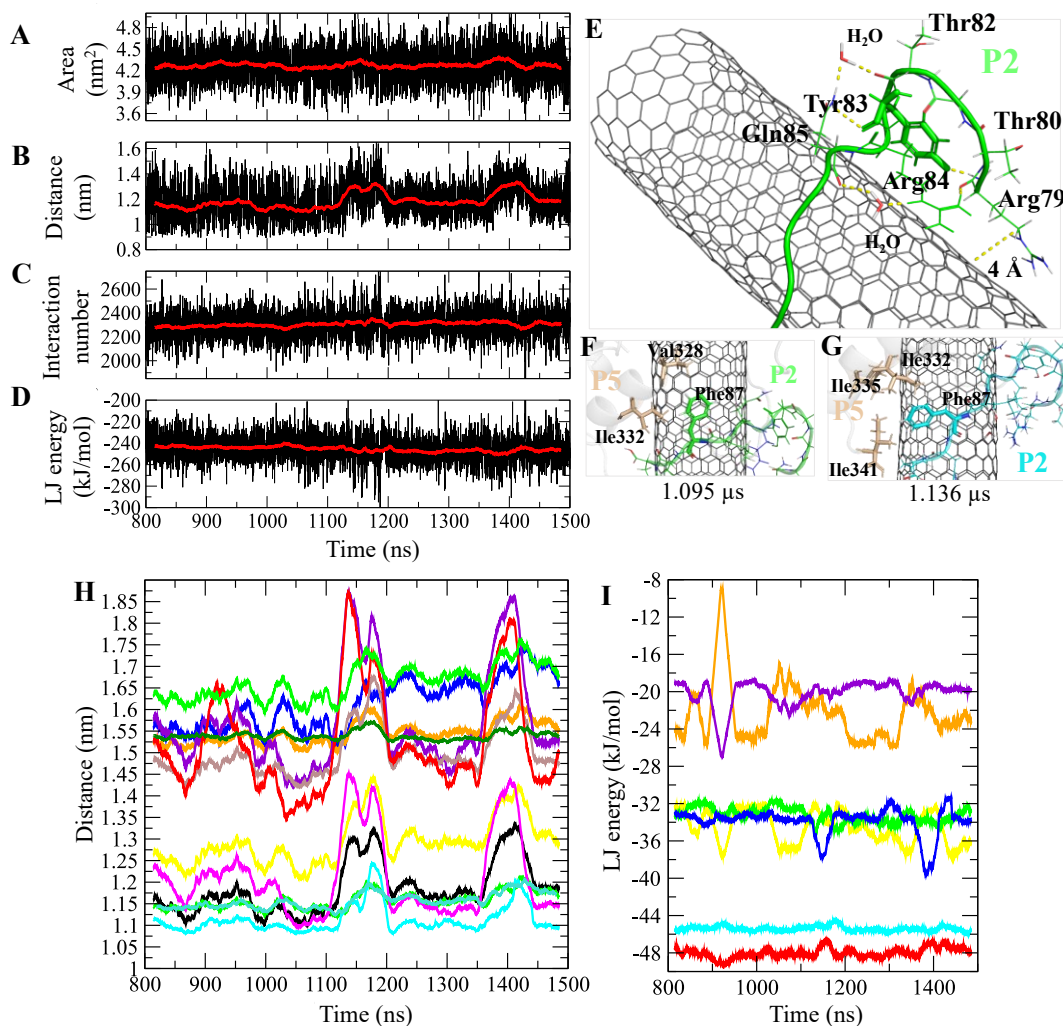
Asp329–Phe343[1]).

Figure A6 The properties between the CNT and the P2: (A) SAS area, (B) DCOM, (C)

interaction frequency (< 6 Å), and (D) LJ energy. (F) Tyr83 (stick) of the P2 caused steric

hindrance and induced local bend conformation. (G–H) Phe57 non-parallel orientations on the

CNT. (H) The DCOM average between the CNT and: the P2 (black), Arg79 (blue), Thr80

(green), Gly81 (orange), Thr82 (dark green), Tyr83 (turquoise), Arg84 (yellow), Gln85 (cyan),

Leu86 (brown), Phe87 (magenta), His88 (violet), Pro89 (red). (I) The LJ energy average between

the CNT and: Arg79 (red), Tyr83 (green), Arg84 (cyan), Gln85 (blue), and Phe87 (yellow), His88 (orange), and Pro89 (violet). Graphs were generated with averaging every 300 frames.
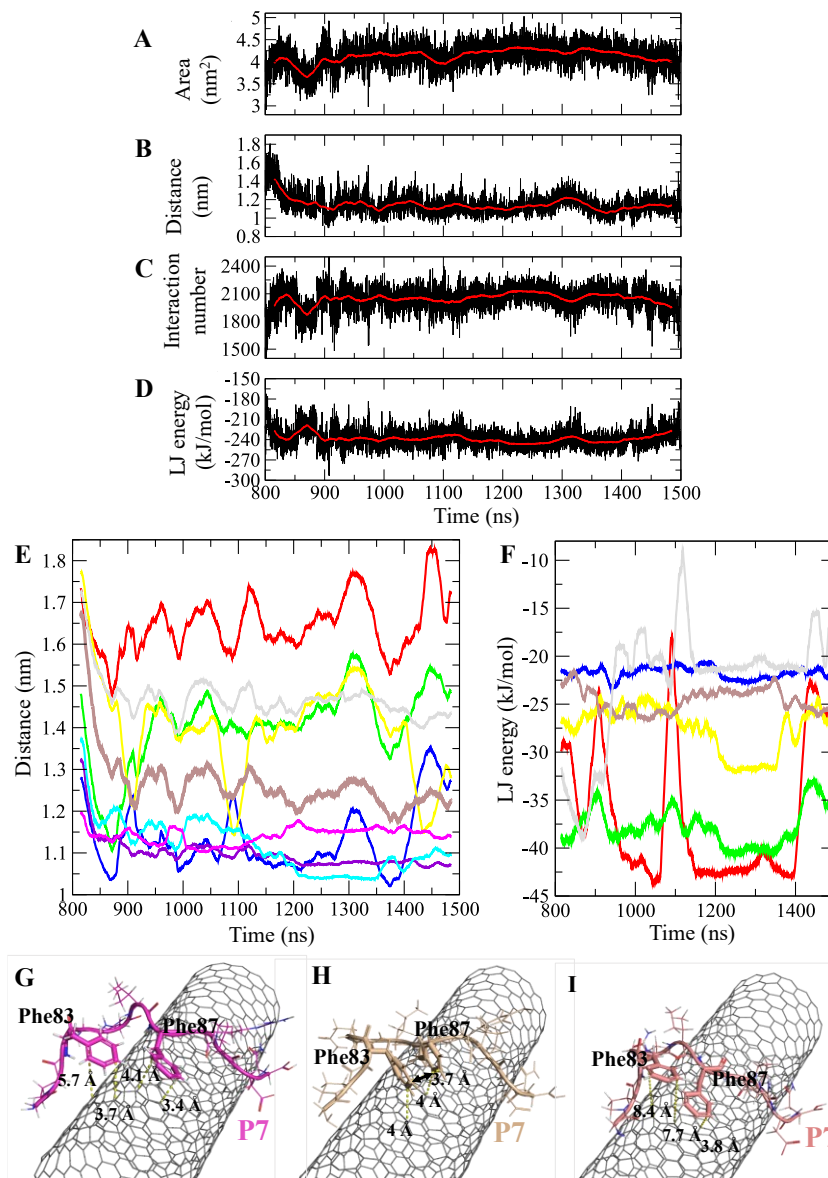

Figure A7 The properties between the CNT and the P7 (β-H2–B3): (A) SAS area, (B) DCOM, (C) interaction frequency (< 6 Å), and (D) LJ energy. (E) The DCOM average between the CNT and: Phe83 (red), Gly84 (green), Gln85 (blue), Ile86 (yellow), Phe87 (brown), Arg88 (gray), Pro89 (violet), Asp90 (cyan), Asn91 (magenta). (F) The LJ energy average of the CNT with: Gln85 (red), Phe87 (green), Asp90 (yellow), Asn91 (brown), Phe83 (gray), and Pro89 (blue).

Graphs were generated with averaging every 300 frames. (G–I) Phe83 and Phe87 (stick) of the

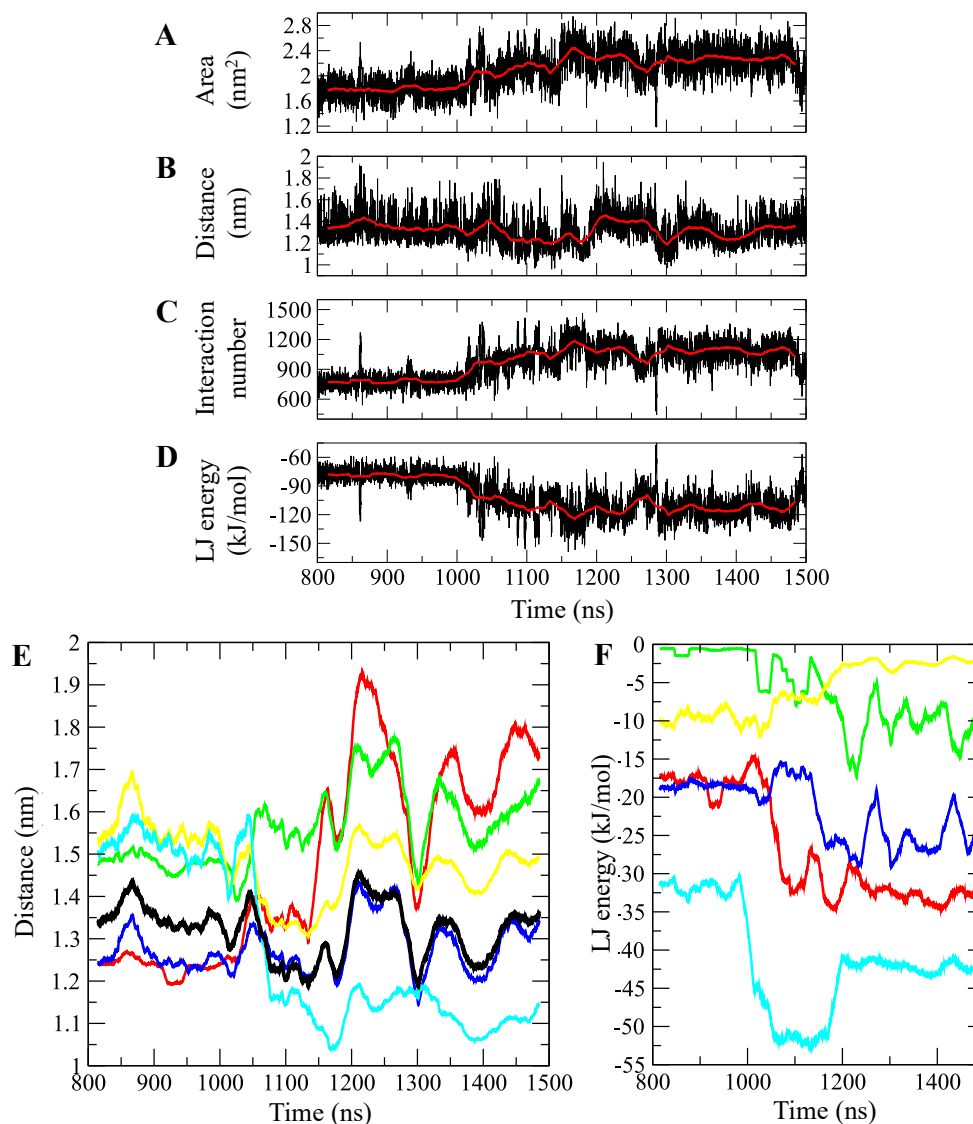P7 changes of orientation and distances to the CNT.

Figure A8 The time evolution of properties between the CNT and the P3 (α-H4–T5): (A)

SAS area, (B) DCOM, (C) interaction frequency (< 6 Å), and (D) LJ energy. (E) DCOM

average between the CNT and: Leu157 (red), Ser158 (green), Val159 (blue), Asp160

(yellow), and Tyr161 (cyan). (F) LJ energy average of the CNT with: Leu157 (red), Ser158

(green), Val159 (blue), Asp160 (yellow), and Tyr161 (cyan). Graphs were generated with averaging every 300 frames of the 1.5 μs MD trajectory.
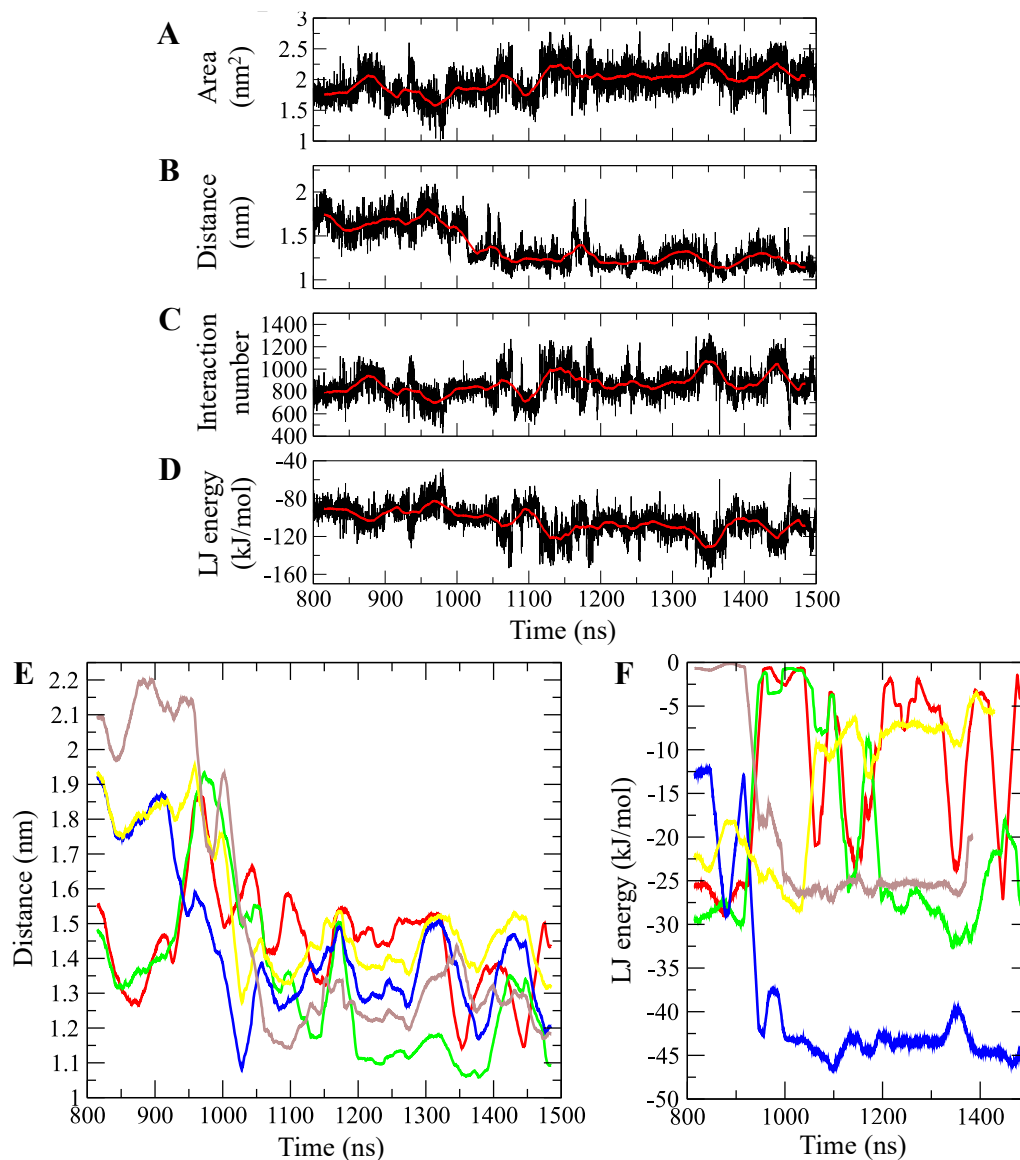
Figure A9 The time evolution of properties between the CNT and P8 (β-H4–T5): (A) SAS area, (B) DCOM, (C) interaction frequency (< 6 Å), and (D) LJ energy. (E) The DCOM average between the CNT and: Glu159 (red), Glu160 (green), Tyr161 (blue), Pro162 (yellow), and Asp163 (brown). (F) The LJ energy average of the CNT with: Glu159 (red), Glu160 (green), Tyr161 (blue), Pro162 (yellow), and Asp163 (brown). Graphs were generated with averaging every 300 frames of the 1.5 μs MD trajectory.
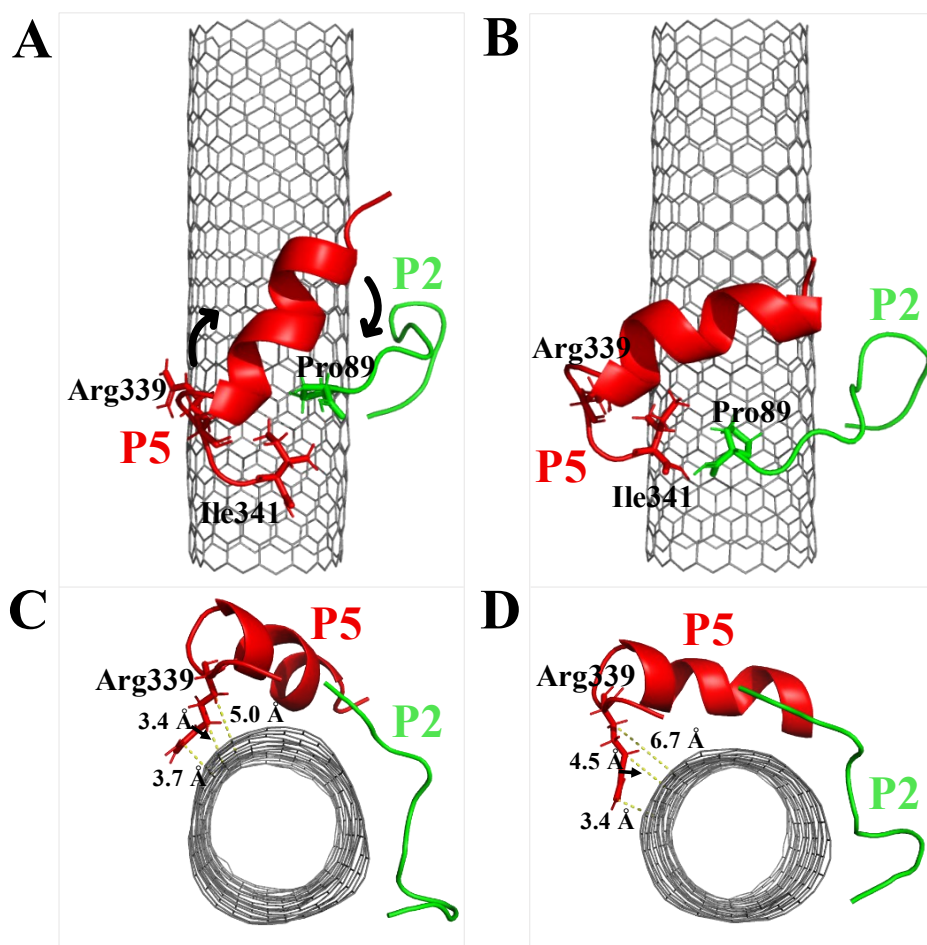
Figure A10 Representative snapshots of the P5 (red) moving from (A) diagonally positioned to (B) almost perpendicular to the CNT length axis while P2 (green) Pro89 approached P5 Ile341. Distance increase from the CNT of Arg339 (P5) from (C) ladder-shaped to (D) almost perpendicular to the CNT.
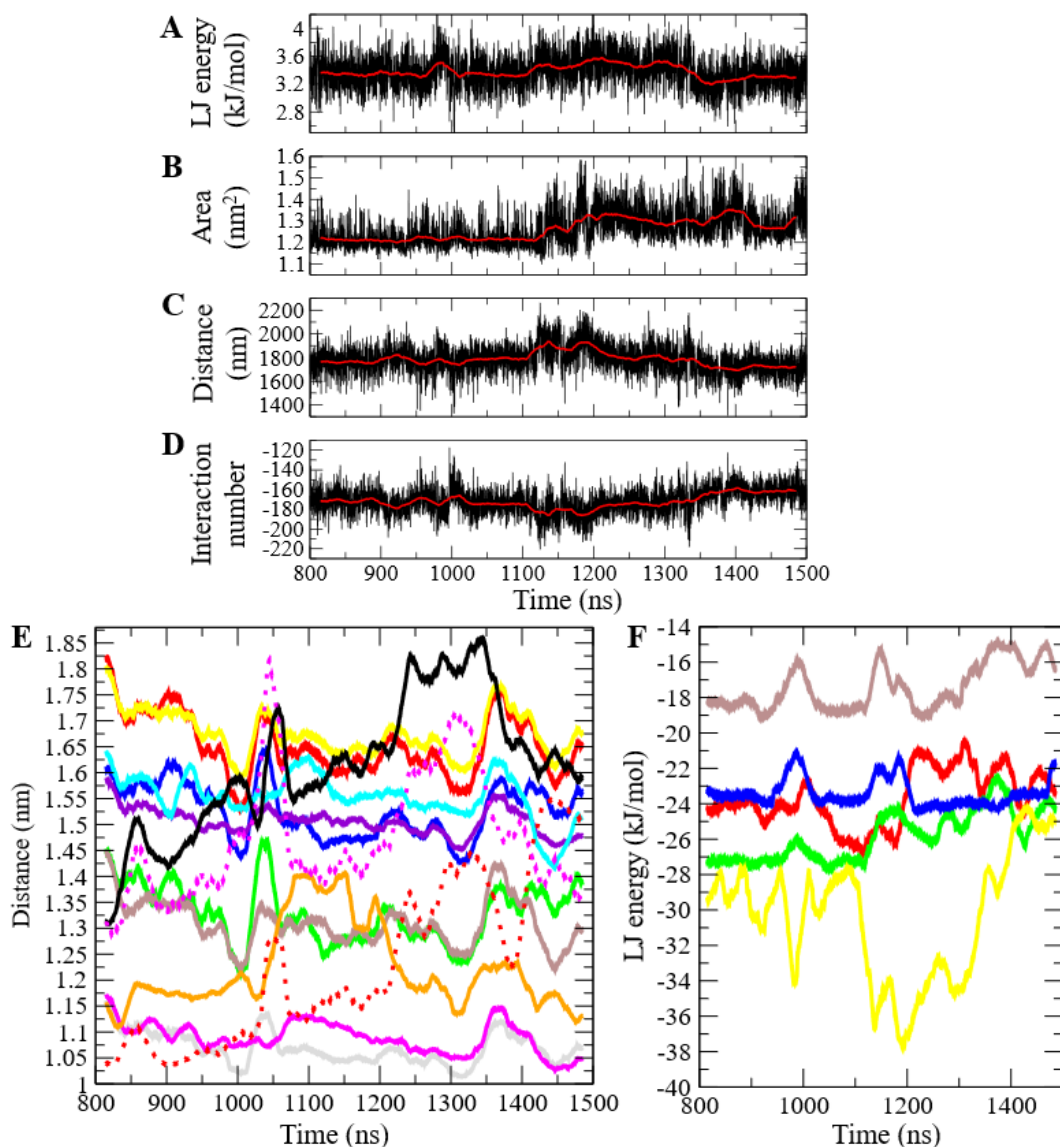
Figure A11 The time evolution of properties between the CNT and P5 (α-H10): (A) SAS area, (B) DCOM, (C) interaction frequency (< 6 Å), and (D) LJ energy. (E) The DCOM average between the CNT and: Ile332 (cyan), Ile335 (violet), Val328 (magenta), Arg339 (blue), Ala330 (red), Ala331 (green), Thr334 (black), Asn329 (yellow), and Asp327 (brown). (F) The LJ energy average regarding the CNT with: Val328 (red), Ala331 (brown), Ile332 (green), Ile335 (blue), and Arg339 (yellow). Graphs were generated with averaging every 300 frames of the 1.5 μs MD trajectory.

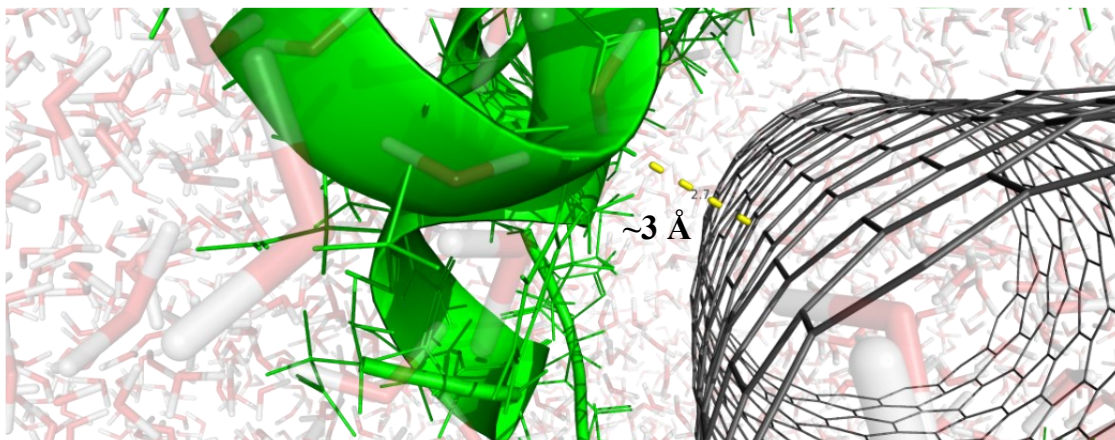**Figure A12** Dehydration gap of 3 Å between the exterior CNT shell and the peptides.
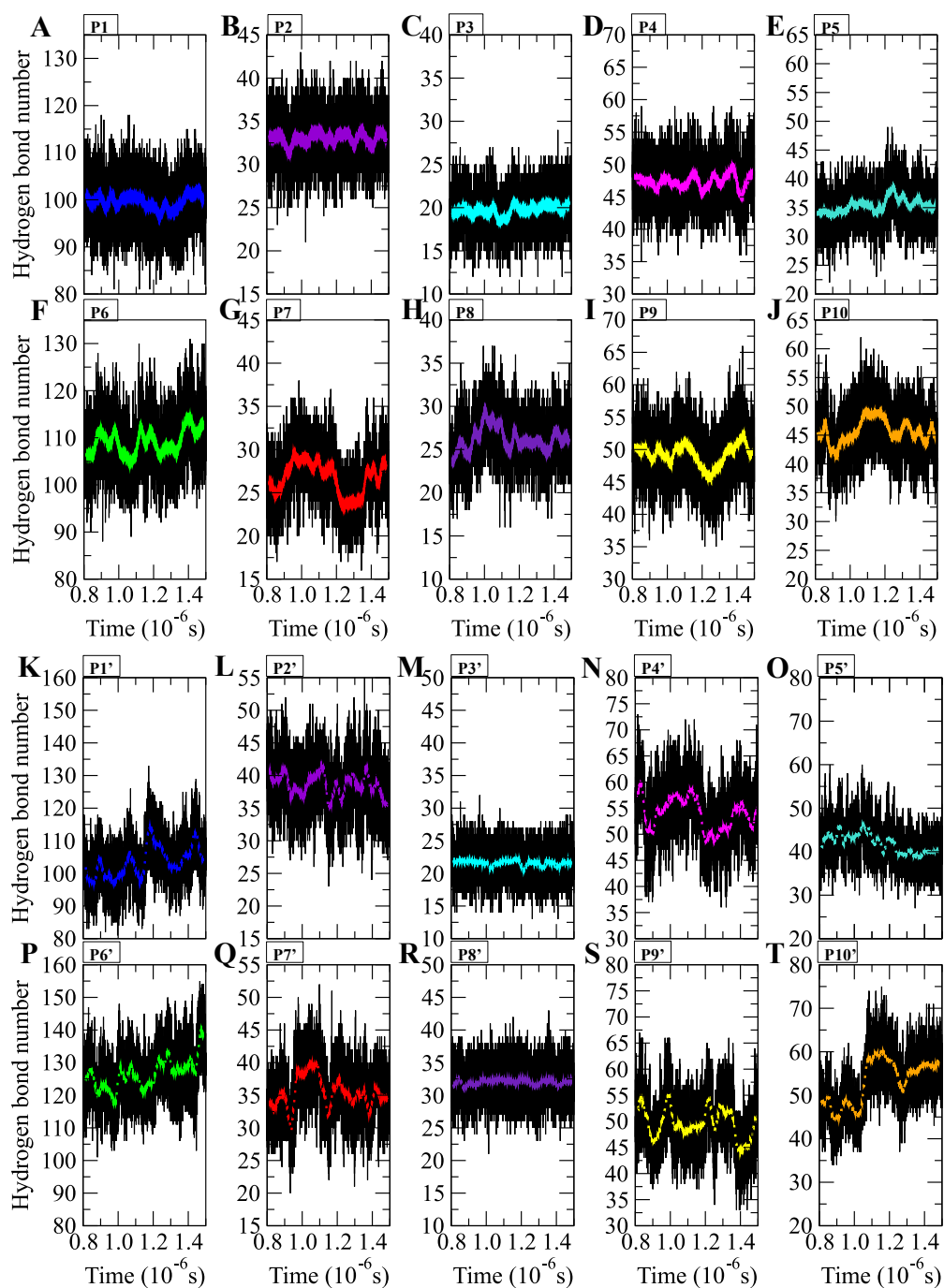
Figure A13 The time evolution of the intermolecular (with water) hydrogen-bond number between the CNT-complexed peptides (A) P1, (B) P2, (C) P3, (D) P4, (E) P5, (F) P6, (G) P7, (H) P8, (I) P9, and (J) P10 and their unbounded peptides (control systems) (K) P1', (L) P2', (M) P3', (N) P4', (O) P5', (P) P6', (Q) P7', (R) P8', (S) P9', and (T) P10'.
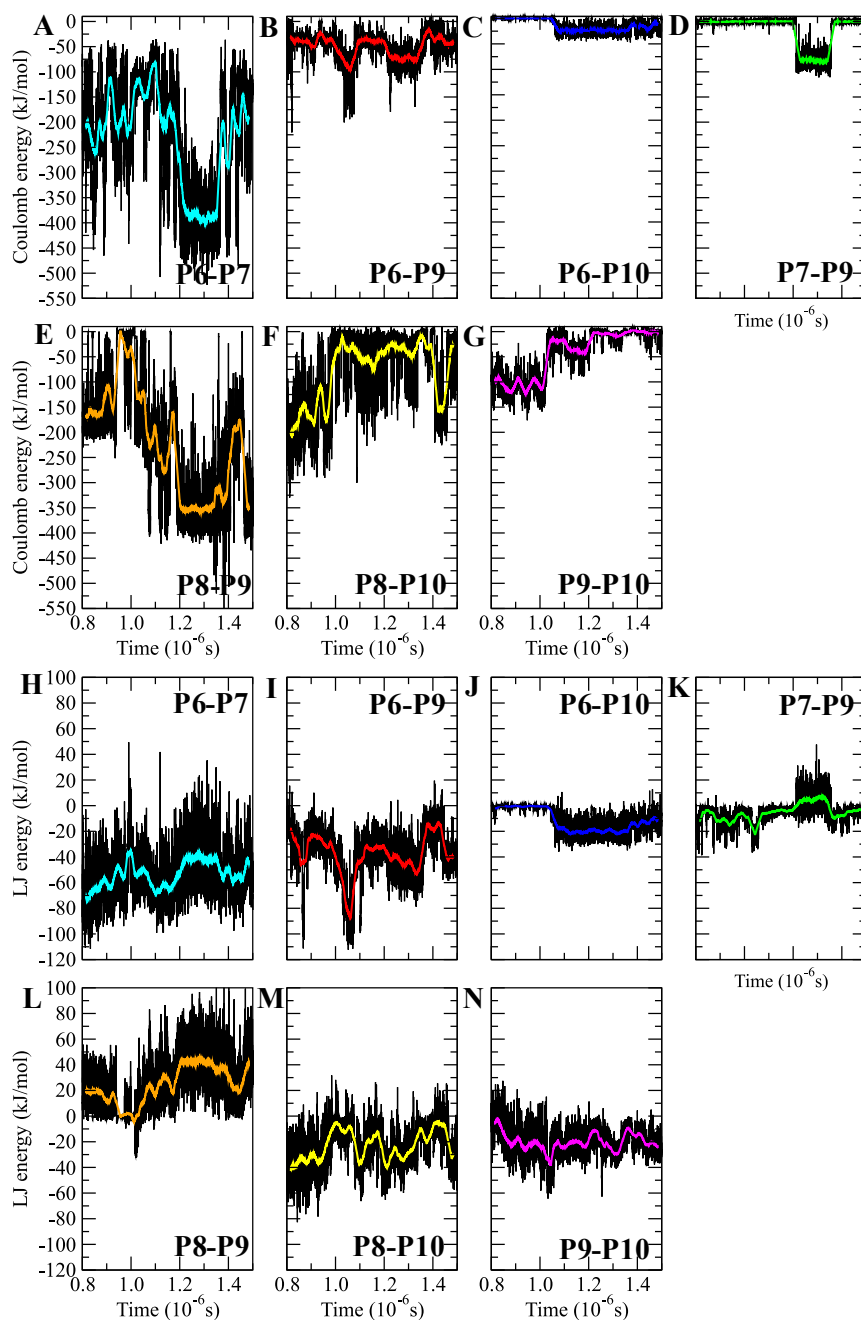
Figure A14 The coulomb force average between the (A) P6 and P7, (B) P6 and P9, (C) P6 and P10, (D) P7 and P9, (E) P8 and P9, (F) P8 and P10, (G) P9 and P10, and the LJ energy average between the (H) P6 and P7, (I) P6 and P9, (J) P6 and P10, (K) P7 and P9, (L) P8 and P9, (M) P8 and P10, (N) P9 and P10, in the C2 complex. Averaging generation every 300 frames.
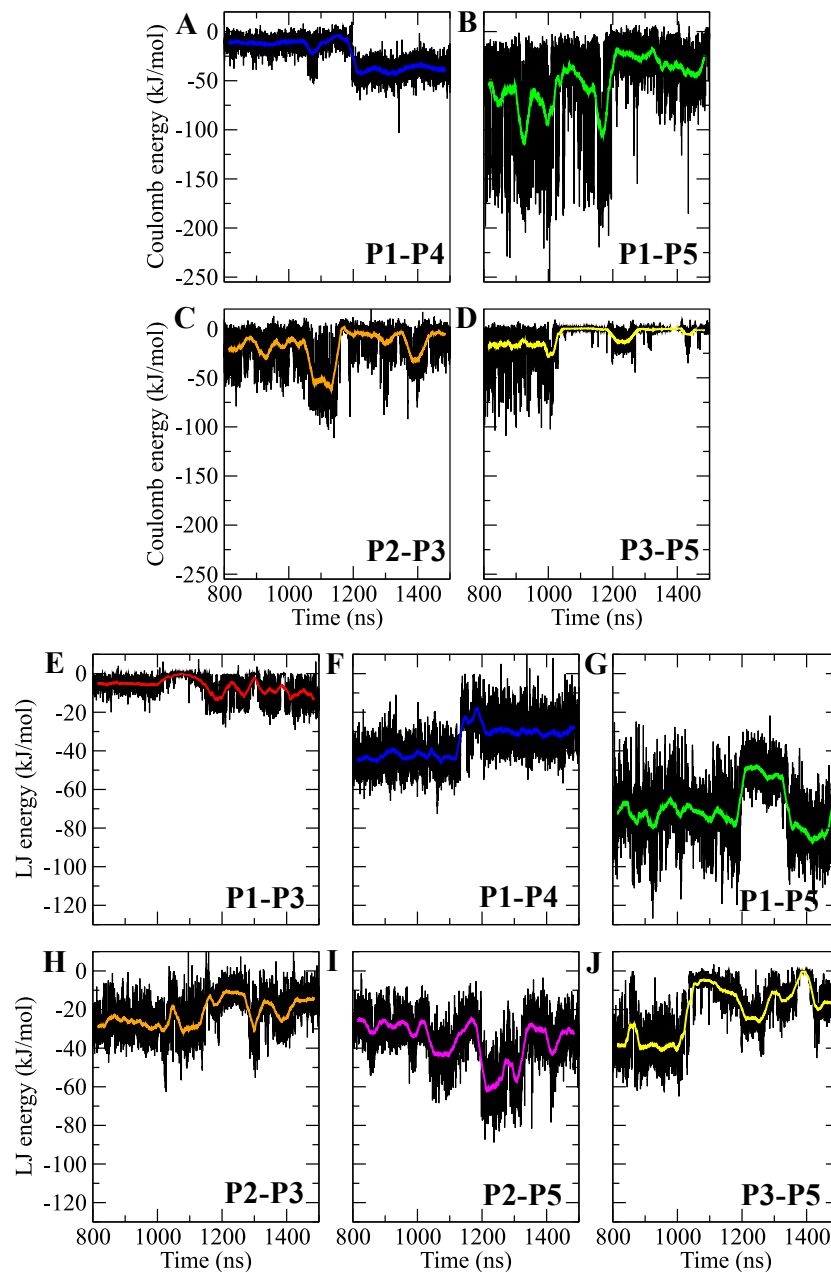
Figure A15 The average of coulomb forces between the (A) P1 and P4, (B) P1 and P5, (C) P2 and P3, (D) P3 and P5, and the average of LJ energy between the (E) P1 and P3, (F) P1 and P4, (G) P1 and P5, (H) P2 and P3, (I) P2 and P5, and (J) P3 and P5, in the C1complex. Graphs were generated with averaging every 300 frames of the 1.5 μs MD trajectory.
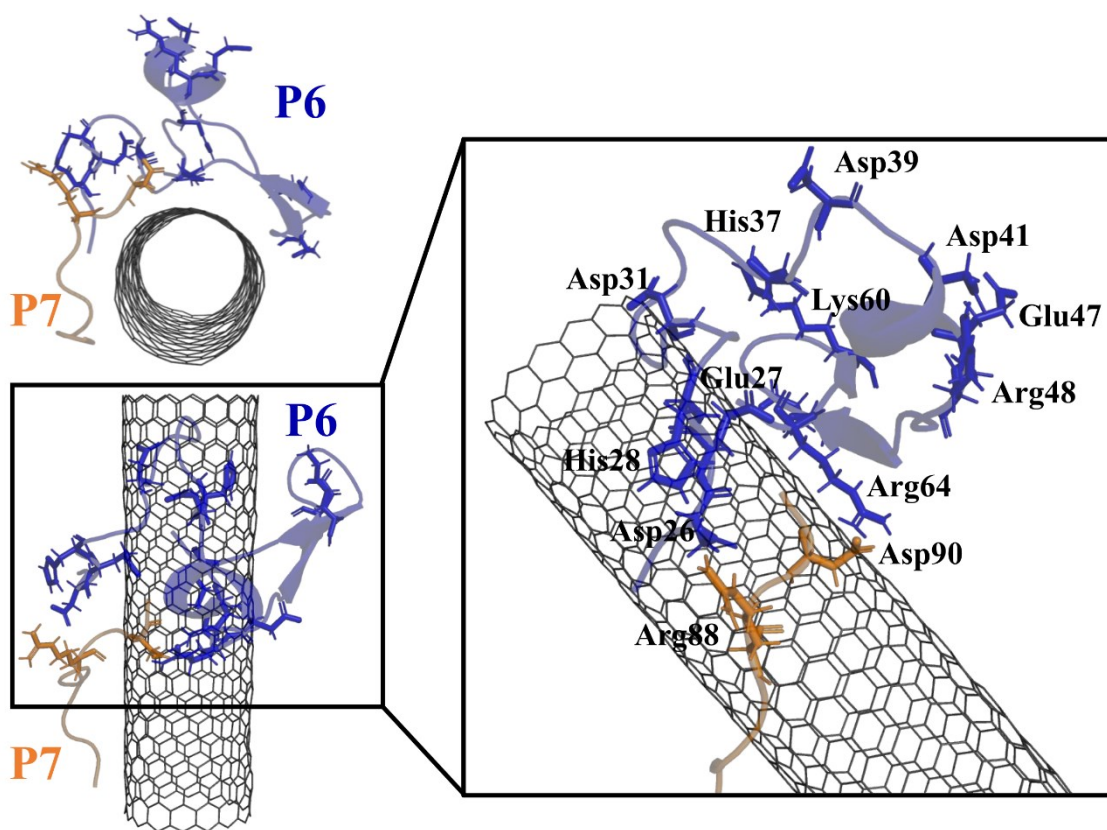
Figure A16 The P6 and P7 conformations on the CNT wherein the half structure of the P6 contains most of its electrostatic residues, while C-terminal of the P7 (Arg88 and Asp90) holds charged residues as well. The remaining P8, P9, and P10 in the C2 system were not shown to obtain better visualization.

Table A1 The tubulin-lateral peptides as control unbounded segments (the P1'–P10') with their assigned SS on the tubulin heterodimer crystal structure (1JFF.pdb[1]) and location in the MT protofilaments. The amino acids are shown as single-letter codes. The letters "T", "B", and "H" refer to the loops, β-strand, and α-helix, respectively.

| Peptide	Segment in MT	Functional association in MT (inter-subunits)	Residue range (1JFF.pdb[1])	Sequence and amino acid (AA) number
P1'	α-H1–B2	Lateral	Tyr24–Pro63	Y_{24}CLEHGIQPDGQMPSDKTIGGGDDS FNTFFSETGAGKHVP$_{63}$ (40 AA)
P2'	α-H2–B3	Lateral	Arg79–Pro89	R_{79}TGTYRQLFHP$_{89}$ (11 AA)
P3'	α-H4–T5	Lateral	Leu157–Tyr161	L_{157}SVDY$_{161}$ (5 AA)
P4'	α-M-loop	Lateral	Tyr272–Val288	Y_{272}APVISAEKAYHEQLSV$_{288}$ (17 AA)
P5'	α-H10	Lateral and Longitudinal	Asp327–Ile341	D_{327}VNAAIATIKTKRSI$_{341}$ (15 AA)
P6'	β-H1–B2	Lateral	Ile24–Ala65	I_{24}SDEHGIDPTGSYHGDSDLQLERINV YYNEAAGNKYVPRA$_{65}$ (40 AA)
P7'	β-H2–B3	Lateral	Gly81–Asn91	G_{81}PFGQIFRPDN$_{91}$ (11 AA)
P8'	β-H4–T5	Lateral	Glu159–Asp163	E_{159}EYPD$_{163}$ (5 AA)
P9'	β-M-loop	Lateral	Pro274–Glu290	P_{274}LTSRGSQQYRALTVPE$_{290}$ (17 AA)
P10'	β-H10	Lateral and Longitudinal	Asp329–Phe343	D_{329}EQMLNVQNKNSSYF$_{343}$ (15 AA)

---

[1] Löwe, J.; Li, H.; Downing, K. H.; Nogales, E., Refined structure of alpha beta-tubulin at 3.5 A resolution. J Mol Biol 2001, 313 (5), 1045–57.

Table A2 The number of CNT atoms, water molecules, and water box dimension of the pristine CNT (*i.e.* peptide-free), the tubulin peptides on the CNT systems (the C1 complex contains the P1–P5, and the C2 complex contains the P6–P10), and the unbounded peptides

Systems	Number of CNT carbon atoms	Number of water molecules	Water box dimensions (nm^3)
Free CNT	640	16726	8 x 8 x 8
C1 (the P1–P5 on the CNT)	640	16262	8 x 8 x 8
C2 (the P6–P10 on the CNT)	640	16269	8 x 8 x 8
P1'	-	4248	5.1 x 5.1 x 5.1
P2'	-	2135	4.2 x 4.2 x 4.2
P3'	-	1278	3.3 x 3.3 x 3.3
P4'	-	3363	4.8 x 4.8 x 4.8
P5'	-	2840	4.7 x 4.7 x 4.7
P6'	-	3797	5.0 x 5.0 x 5.0
P7'	-	2571	4.3 x 4.3 x 4.3
P8'	-	1443	3.6 x 3.6 x 3.6
P9'	-	3762	4.7 x 4.7 x 4.7
P10'	-	2919	4.5 x 4.5 x 4.5

without the CNT (the P1'–P10').

Table A3 The energy minimization input parameters (*i.e.*, emtol and emstep) and output data (*i.e.*, potential energy, maximum force and normal of force) of the pristine CNT, the CNT-complexes C1 (the P1–P5) and C2 (the P6–P10), and each free peptide without the CNT (the P1'–P10').

	EM parameters		EM output		
	Emtol (kJ mol^{-1} nm^{-1})	Emstep (nm)	Potential Energy (kJ mol^{-1})	Maximum force (kJ mol^{-1} nm^{-1})	Norm of force (kJ mol^{-1} nm^{-1})
Free CNT	100	0.01	$-8.254e+05$	99.97	13.52
C1	100	0.01	$-8.266E+05$	99.73	10.10
C2	65	0.005	$-8.424E+05$	64.37	5.37
P1'	1000	0.01	$-2.095E+05$	862.02	33.99
P2'	1000	0.01	$-1.002E+05$	901.58	51.65
P3'	1000	0.01	$-5.899E+04$	974.27	52.10
P4'	1000	0.01	$-1.615E+05$	953.49	33.02
P5'	1000	0.01	$-1.337E+05$	955.92	43.41
P6'	1000	0.01	$-1.894E+05$	900.33	30.13
P7'	1000	0.01	$-1.203E+05$	967.89	42.34
P8'	1000	0.01	$-6.796E+04$	801.96	53.04
P9'	1000	0.01	$-1.805E+05$	954.91	34.68
P10'	1000	0.01	$-1.386E+05$	869.27	41.16

Table A4 The sequence similarities between pair of equivalent peptides from respective α- and β-tubulin subunits (*i.e.*, the P1–P6; the P2–P7; the P3–P8; the P4–P9; and the P5–P10). In alignment, the colon (:) indicates conservation between groups of strongly similar properties, and the period (.) means conservation between groups of weakly similar properties.

Peptides on the CNT	Identity and Similarity (%)	Alignment*
P1 vs. P6	32.4% and 75.7% (37 AA overlap of 4–40:4–37)	EHGIQPDGQMPSDKTIGGGDDSFNTFFSETGAGKHVP :::::.: :.. .:. . . .:.....:. ..:.:: EHGIDPTGSYHGDSDLQL--ERINVYYNEATGNKYVP
P2 vs. P7	44.4% and 77.8% (9 AA overlap of 3–11:1–9)	GTYRQLFHP : . :.:.: GPFGQIFRP
P4 vs. P9	26.7% and 60.0% (15 AA overlap of 3–17:1–15)	PVISAEKAYHEQLSV :. : . .. :.: PLTSRGSQQYRALTV
P5 vs. P10	16.7% and 66.7% (12 AA overlap of 3–14:1–12)	NAAIATIKTKRS . . ....: : DEQMLNVQNKNS

Table A5 The average RMSF of the unbounded peptide systems without the CNT (the P1'–P10') and the peptides on the CNT of the C1 (containing the P1–P5) and the C2 (containing the P6–P10) complexes during 0.8–1.5 µs of MD trajectories.

Free peptides	Free peptides RMSF (Å)	Peptides on the CNT	C1 RMSF (Å)	C2 RMSF (Å)
P1'	3.94 ± 1.13	P1	2.25 ± 0.52	-
P2'	4.85 ± 0.50	P2	2.10 ± 0.31	-
P3'	2.83 ± 0.62	P3	5.87 ± 0.89	-
P4'	5.12 ± 0.92	P4	2.16 ± 0.44	-
P5'	4.39 ± 0.80	P5	1.96 ± 0.28	-
P6'	5.04 ± 1.02	P6	-	2.61 ± 0.53
P7'	4.70 ± 1.00	P7	-	3.10 ± 0.64
P8'	2.08 ± 0.35	P8	-	5.94 ± 1.08
P9'	4.72 ± 1.23	P9	-	3.48 ± 1.06
P10'	5.16 ± 0.58	P10	-	3.35 ± 0.46

Table A6 The average hydrogen-bond number of each tubulin peptides with water of the C1 (the P1–P5) and the C2 (the P6–P10) on the CNT complexes during 0.8–1.5 μs simulation time.

Peptides	Inter hydrogen bond number with water molecules
P1	100 ± 4
P2	33 ± 2
P3	20 ± 2
P4	47 ± 3
P5	35 ± 3
P6	109 ± 5
P7	27 ± 3
P8	26 ± 2
P9	49 ± 3
P10	46 ± 3
P1'	104 ± 6
P2'	39 ± 3
P3'	22 ± 2
P4'	54 ± 4
P5'	42 ± 4
P6'	127 ± 6
P7'	35 ± 3
P8'	32 ± 2
P9'	50 ± 4
P10'	53 ± 5

Table A7 The average DCOM, SAS area, interaction frequency number (at a distance ≤ 6.0 Å), and LJ energy between each tubulin peptide and the CNT during 0.8–1.5 µs time interval. The approximation values of the hydrophobic (HYD) and hydrophilic (HILIC) SAS area, and the total average SAS area, of each peptide.

Peptides	DCOM (nm)	SAS area (nm²)	№ of Interactions	LJ energy (kJ mol⁻¹)	HYD, HILIC, and total SAS area (nm²)
P1	1.85 ± 0.14	3.64 ± 0.32	1,840 ± 206	−219.69 ± 28.50	~17, ~15, 31.91 ± 0.79
P2	1.18 ± 0.13	4.27 ± 0.18	2,304 ± 83	−245.41 ± 8.92	~10, ~8, 17.55 ± 0.34
P3	1.32 ± 0.11	2.08 ± 0.25	975 ± 147	−101.51 ± 16.58	~5, ~4, 8.89 ± 0.29
P4	0.96 ± 0.04	6.05 ± 0.28	3,635 ± 139	−425.43 ± 16.21	~13, ~9, 21.97 ± 0.57
P5	1.26 ± 0.06	3.38 ± 0.19	1,783 ± 88	−172.03 ± 10.03	~9, ~8, 17.16 ± 0.44
P6	1.54 ± 0.09	5.56 ± 0.27	2,823 ± 113	−314.47 ± 12.18	~19, ~17.5, 36.46 ± 1.23
P7	1.15 ± 0.11	4.13 ± 0.22	2,046 ± 96	−238.11 ± 10.47	~9, ~8, 16.72 ± 0.44
P8	1.37 ± 0.23	1.97 ± 0.21	865 ± 101	−104.40 ± 12.33	~4, ~5, 9.02 ± 0.29
P9	1.11 ± 0.16	5.90 ± 0.43	3,373 ± 228	−375.84 ± 27.29	~13, ~11, 24.20 ± 0.61
P10	1.25 ± 0.08	4. 40 ± 0.37	2,076 ± 180	−239.22 ± 20.56	~10, ~10, 19.89 ± 0.66